

ADA 044304

12
B.S.

Change No. 4

for

THE TRAPPED RADIATION HANDBOOK
(DNA 2524H)

4 January 1977

Instructions

The recipient is requested to remove the pages listed below and add the attached pages per DNA letter of approval dated 13 June 1977, and record this action on page iii.

Remove

Title Page (2 December 1974)
ii (2 December 1974)
ix through xii (2 December 1974)
xvii through xxxviii (1 November 1973)
4-1 through 4-88 (Original)
D-1 through D-8 (2 December 1974)

Add

Title Page (4 January 1977)
ii (4 January 1977)
ix through xii (4 January 1977)
xvii through xl (4 January 1977)
4-1 through 4-100 (4 January 1977)
D-1 through D-10 (4 January 1977)

Note: If the recipient did not receive a copy of DNA 2524H (The Trapped Radiation Handbook) plus Changes 1 through 3, they can be obtained by addressing a request to the below named individual. However, a limited supply is available for this purpose.

M. J. Dudash
General Electric Company - TEMPO
DASIAC
816 State Street
Santa Barbara, California 93102

DDC
RECEIVED
SEP 16 1977
C

AD No. _____
DDC FILE COPY

6 THE TRAPPED RADIATION HANDBOOK
Change 11

18 DNA 2524H
Change 4

Compilers and Editors-in Chief:

10 John B. Cladis,
Gerald T. Davidson
Lester L. Newkirk

11 Revised
4 January 1977

12 128 p.

ADDITIONAL FOR	
CLASSIFICATION	<input checked="" type="checkbox"/>
CONTROL	<input type="checkbox"/>
EXEMPTION	<input type="checkbox"/>
U.S. GOVERNMENT	
BY	
DISTRIBUTION/AVAILABILITY CODES	
DIS. CONTROL	
A	

Project Officer: Dr. Charles A. Blank

Prepared for:

Defense Nuclear Agency
Washington, D.C. 20305

15 by Lockheed Palo Alto Research Laboratory
~~Under Contract DNA 001-73-C-0065~~
NWER Subtask HC047-08

Published by:

DASIAC
General Electric Company—TEMPO
Santa Barbara, California 93102
Under Contract DNA 001-75-C-0023
NWED Subtask DC008-01

Approved for public release; distribution unlimited

210 118

4B

4 January 1977

LIST OF EFFECTIVE PAGES

<u>PAGE</u>	<u>LAST CHANGE</u>	<u>PAGE</u>	<u>LAST CHANGE</u>
Title Page	4 January 1977	6-1 through 6-60	Original
ii	4 January 1977	7-1 through 7-30	Original
iii through iv	2 December 1974	8-1 through 8-2	1 November 1973
v through viii	1 November 1973	8-3 through 8-4	Original
ix through xii	4 January 1977	8-5 through 8-6	1 November 1973
xiii through xvi	2 December 1974	8-7 through 8-8	Original
xvii through xl	4 January 1977	8-9 through 8-10	2 December 1974
1-1 through 1-22	Original	8-11 through 8-12	Original
2-1 through 2-6	Original	8-13 through 8-35	1 November 1973
2-7 through 2-8	2 January 1973	8-35A through 8-35D	1 November 1973
2-9 through 2-10	Original	8-36	1 November 1973
2-11 through 2-12	2 January 1973	8-37 through 8-80	Original
2-13 through 2-32	Original	8-81 through 8-82	2 January 1973
2-33 through 2-34	2 January 1973	8-83 through 8-84	Original
2-35 through 2-66	Original	8-85 through 8-86	1 November 1973
3-1 through 3-6	Original	8-87 through 8-88	Original
3-7 through 3-8	2 January 1973	8-89 through 8-90	1 November 1973
3-9 through 3-18	Original	9-1 through 9-36	Original
3-19 through 3-24	2 December 1974	10-1 through 10-9	Original
3-25 through 3-36	Original	11-1 through 11-34	Original
3-37 through 3-46	2 December 1974	11-35 through 11-36	2 January 1973
3-47 through 3-68	Original	11-37 through 11-60	Original
3-69 through 3-100	2 December 1974	12-1 through 12-6	Original
4-1 through 4-100	4 January 1977	13-1 through 13-20	Original
5-1 through 5-2	2 December 1974	14-1 through 14-2	Original
5-3 through 5-8	Original	14-3 through 14-4	2 January 1973
5-9 through 5-126	2 December 1974	15-1 through 15-18	2 December 1974
		D-1 through D-10	4 January 1977

4 January 1977

CONTENTS

LIST OF EFFECTIVE PAGES	ii
RECORD OF REVISIONS	iii
ACKNOWLEDGMENTS	iv
PREFACE	v
ILLUSTRATIONS	xv
TABLES	xxxiii
AUTHORS	xxxvii

SECTION 1

THE MAGNETOSPHERE	1-1
Introduction	1-1
Conditions in Interplanetary Space	1-1
Interaction of Solar Wind with Geomagnetic Field	1-2
The Radiation Belts	1-7
Magnetospheric Electric Fields	1-12
Magnetospheric Convection	1-19
REFERENCES	1-19

SECTION 2

THE GEOMAGNETIC FIELD	2-1
Introduction	2-1
Magnetic Field Elements	2-2
The Dipolar Field of the Earth	2-4
The Spherical Harmonic Expansion of the Field	2-17

4 January 1977

Distant Magnetic Field	2-22
Geomagnetic Transient Variations	2-29
Geomagnetic Pulsations	2-33
APPENDIX 2A-GEOMAGNETIC INDICES	2-37
APPENDIX 2B-MAPS OF THE GEOMAGNETIC LATITUDE AND LONGITUDE	2-41
APPENDIX 2C-CONTOURS B, L FOR VARYING ALTITUDES	2-49
APPENDIX 2D-CONSTANT-B VERSUS ALTITUDE, LONGI- TITUDE AND MAGNETIC SHELL NUMBER	2-55
REFERENCES	2-61

SECTION 3

THE MOTION OF CHARGED PARTICLES IN THE EARTH'S MAGNETIC FIELD	3-1
Introduction	3-1
The Motion of an Electrically Charged Particle in a Magnetic Dipole Field	3-3
The Guiding Center Approximation	3-15
The Adiabatic Approximation	3-26
Liouville's Theorem	3-35
Hydromagnetic Model for a Plasma	3-38
APPENDIX 3A-ELECTRIC AND MAGNETIC UNITS	3-47
APPENDIX 3B-SUPPLEMENTARY TABLES AND GRAPHS	3-51
APPENDIX 3C-CONVERSION OF OMNIDIRECTIONAL FLUX TO DIRECTIONAL FLUX	3-89
REFERENCES	3-93

SECTION 4

TRAPPED RADIATION POPULATION	4-1
Introduction	4-1
Trapped Proton Environment	4-2

4 January 1977

Trapped Electron Environment	4-6
Magnetospherically Trapped Ions with $Z \geq 2$	4-20
Summary	4-23
REFERENCES	4-24

SECTION 5

SOURCES AND LOSSES OF TRAPPED PARTICLES	5-1
Introduction	5-1
Losses in the Atmosphere	5-2
Injection of Trapped Particles Through Nuclear Decays	5-28
Nonconservation of the Third Adiabatic Invariant	5-35
Nonconservation of the First and Second Adiabatic Invariants	5-58
Convection in the Outer Magnetosphere as a Source of Trapped Particles	5-107
REFERENCES	5-109

SECTION 6

HISTORY OF ARTIFICIAL RADIATION BELTS	6-1
Introduction	6-1
Teak and Orange	6-3
Argus Experiments	6-13
Starfish	6-31
USSR Detonations in 1962	6-47
REFERENCES	6-55

SECTION 7

PARTICLE INJECTION BY NUCLEAR DETONATIONS	7-1
Introduction	7-1
Sources of Electrons	7-1

4 January 1977

Trapping Efficiency	7-9
Trapping Phenomenology	7-12
REFERENCES	7-30

SECTION 8

EFFECTS OF TRAPPED RADIATION ON SPACECRAFT SYSTEMS	8-1
Summary and Introduction	8-1
Trapped Radiation Effects on Semiconductor Devices	8-5
Trapped Radiation Effects on Thermal Control and Solar Reflector Surfaces	8-36
Trapped Radiation Effects on Selected Optical Materials and Devices	8-42
Orbital and Shielding Effects on Damage Parameters	8-44
REFERENCES	8-83

SECTION 9

SYNCHROTRON RADIATION FROM ELECTRONS TRAPPED IN THE EARTH'S MAGNETIC FIELD	9-1
Introduction	9-1
Summary of Synchrotron Theory	9-1
Synchrotron Radiation from Starfish Electrons	9-19
Synchrotron Radiation from a Model Electron Flux Distribution	9-21
Summary	9-29
REFERENCES	9-33
SELECTED ADDITIONAL REFERENCES	9-35

SECTION 10

VULNERABILITY OF OPERATIONAL SYSTEMS TO TRAPPED RADIATION	10-1
Introduction	10-1
Satellite Systems in Natural Environment	10-1
Spacecraft Systems in Weapons Test Environment	10-4

4 January 1977

FIGURE	TITLE	PAGE
2D-2	Altitudes of constant-B for $L = 1.20$.	2-57
2D-3	Altitudes of constant-B for $L = 1.60$.	2-58
2D-4	Altitudes of constant-B for $L = 2.20$.	2-59
2D-5	Altitudes of constant-B for $L = 3.50$.	2-60
3-1	The gyro-motion of charged particles in a uniform magnetic field.	3-6
3-2	Forbidden regions in a dipolar magnetic field.	3-10
3-3	Sample charged particle orbiting in the equatorial plane of a magnetic dipole field.	3-11
3-4	Limits of stable trapping in a dipole field as derived from the Störmer orbit theory.	3-12
3-5	Curves of constant Ξ (the Störmer potential) superimposed on dipole field lines.	3-13
3-6	Sample charged particle orbits in a dipolar magnetic field, projected onto a meridian plane.	3-14
3-7	Motion of a charged particle in crossed electric and magnetic fields.	3-16
3-8	Motion of a charged particle in a nonhomogenous magnetic field or in a magnetic field with a superimposed charge-independent transverse force field.	3-17
3-9	Components of the force acting on a positively charged particle in a converging magnetic field.	3-21
3-10	Equatorial cross section of a uniformly varying, axially symmetric field.	3-25
3-11	An adiabatic invariant surface in the geomagnetic field.	3-32
3-12	Splitting of invariant surfaces in the geomagnetic field.	3-34
3B-1a	Nomograph for computing magnetic fields and pitch angles.	3-54
3B-1b	Step-by-step use of the nomograph.	3-55
3B-2	Pitch angle as a function of field intensity.	3-57
3B-3	Mirror latitudes in a dipole field.	3-59
3B-4	The atmospheric cutoff pitch angle.	3-61

4 January 1977

FIGURE	TITLE	PAGE
3B-5	Mirror point altitude as a function of equatorial pitch angle.	3-63
3B-6	Relativistic corrections to velocity and momentum.	3-64
3B-7	Relativistic corrections to velocity and momentum.	3-65
3B-8	Magnetic moment of a charged particle as a function of kinetic energy.	3-67
3B-9	The gyro-period of a charged particle in the geomagnetic field.	3-69
3B-10	The bounce and drift periods of trapped electrons as a function of kinetic energy.	3-71
3B-11	The bounce and drift periods of trapped protons as a function of kinetic energy.	3-72
3B-12	The bounce period and second adiabatic invariant as functions of equatorial pitch angle.	3-73
3B-13	Azimuthal drift period as a function of the equatorial pitch angle in the earth's field.	3-75
3B-14	Energy-dependent factor employed in azimuthal drift computations.	3-77
3B-15	Constant adiabatic invariant curves in a dipole field.	3-79
3B-16	Constant adiabatic invariant curves in B, L coordinates.	3-81
3B-17	Adiabatic invariants of particles entering the atmosphere.	3-83
3B-18	Equatorial pitch angle as a function of L for constant adiabatic invariants.	3-85
3B-19a	Mirror point field as a function of L for constant adiabatic invariants.	3-87
3B-19B	Mirror point field as a function of L for constant adiabatic invariants.	3-88
4-1	Trapping regions for a model magnetosphere.	4-31
4-2	B - L omnidirectional flux map for protons with $E \geq 0.1$ MeV at times of solar minimum and solar maximum—models AP8MIN and AP8MAX.	4-32

4 January 1977

FIGURE	TITLE	PAGE
4-3	B-L omnidirectional flux map for protons with $E \geq 1.0$ MeV at times of solar minimum and solar maximum—models AP8MIN and AP8MAX.	4-33
4-4	B-L omnidirectional flux map for protons with $E \geq 10.0$ MeV at times of solar minimum and solar maximum—models AP8MIN and AP8MAX.	4-34
4-5	B-L omnidirectional flux map for protons with $E \geq 50.0$ MeV at times of solar minimum and solar maximum—models AP8MIN and AP8MAX.	4-35
4-6	B-L omnidirectional flux map for protons with $E \geq 100.0$ MeV at times of solar minimum and solar maximum—models AP8MIN and AP8MAX.	4-36
4-7	B-L omnidirectional flux map for protons with $E \geq 400.0$ MeV at times of solar minimum and solar maximum—models AP8MIN and AP8MAX.	4-37
4-8	Radial distributions of AP8MIN omnidirectional fluxes of protons in the equatorial plane with energies above threshold values between 0.1 and 400.0 MeV.	4-38
4-9	Integral spectra of AP8MIN omnidirectional fluxes of protons for various values of B at $L = 1.2$.	4-39
4-10	Integral spectra of AP8MIN omnidirectional fluxes of protons for various values of B at $L = 1.5$.	4-40
4-11	Integral spectra of AP8MIN omnidirectional fluxes of protons for various values of B at $L = 2.0$.	4-41
4-12	Integral spectra of AP8MIN omnidirectional fluxes of protons for various values of B at $L = 2.5$.	4-42
4-13	Integral spectra of AP8MIN omnidirectional fluxes of protons for various values of B at $L = 3.0$.	4-43
4-14	Integral spectra of AP8MIN omnidirectional fluxes of protons for various values of B at $L = 4.0$.	4-44
4-15	Integral spectra of AP8MIN omnidirectional fluxes of protons for various values of B at $L = 5.0$.	4-45
4-16	Integral spectra of AP8MIN omnidirectional fluxes of protons for various values of B at $L = 6.6$.	4-46

4 January 1977

FIGURE	TITLE	PAGE
4-17	Computed ratio of $J(t)/J$ (1963.0) at 60 MeV and minimum mirror point altitudes of 250, 350, and 450 km, $L = 1.40$, between January 1963 and May 1969.	4-47
4-18	Time behavior of high-energy protons.	4-48
4-19	Time behavior of medium-energy protons.	4-49
4-20	Time behavior of low-energy protons.	4-50
4-21	Time behavior of low-energy protons.	4-51
4-22	Time behavior of low-energy protons at $L = 4.0$.	4-52
4-23	Low-altitude proton observations at $L = 4.85$ with energies between 0.25 and 1.65 MeV, as obtained by the Azur satellite.	4-53
4-24	Differential spectra of directional proton fluxes over the energy range of $200 \text{ eV} \leq E \leq 1 \text{ MeV}$ mirroring at the magnetic equator as compiled from observations with OGO 3, Explorer 12, and Mariner 4.	4-54
4-25	Distribution function, multiplied by two times the proton mass for equatorially mirroring protons as a function of time throughout the period of the December 17, 1971 storm.	4-55
4-26	Contours of AE 2 integral electron-electron flux in the Earth's radiation belts.	4-56
4-27	Time behavior of $>280\text{-KeV}$ electrons in the inner zone.	4-57
4-28	Time behavior of $>1\text{-MeV}$ electrons in the outer zone.	4-58
4-29	The diurnal variation of the mean of logarithm of ATS 1 observation.	4-59
4-30	Equatorial radial profiles of OGO 1 and OGO 3 data, showing the solar-cycle effect.	4-60
4-31	Position of the slot minimum (L_{min}) and the outer belt maximum (L_{max}) in various periods of the solar cycle.	4-61
4-32	Comparison of AE 4 model spectra with the source data at $L = 3.0, 3.6, 4.0, \text{ and } 4.5$.	4-62
4-33	Comparison of AE 4 model spectra with the source data at $L = 5.0, 5.5, 6.0, \text{ and } 6.6$.	4-63

4 January 1977

FIGURE	TITLE	PAGE
4-34	Comparison of model power law parameter for B/B_0 dependence with the calculated parameter from various source data sets.	4-64
4-35	Local time variation of the AE 4 model.	4-65
4-36	Magnitude of the maximum local time variation at $L = 6.6$ for the data set of different epochs: Explorer 12-1962, Explorer 14-1963, IMP 1-1964, ERS 13-1965, and ATS 1-1967.	4-66
4-37	Logarithmic presentation of AE 4 local time model for epoch 1964, threshold energy 0.5 MeV.	4-67
4-38	Logarithmic presentation of AE 4 local time model for epoch 1967, threshold energy 0.5 MeV.	4-68
4-39	AE 4 radial profile of equatorial omnidirectional flux for various energy thresholds, epoch 1964.	4-69
4-40	AE 4 radial profile of equatorial omnidirectional flux for various energy thresholds, epoch 1967.	4-70
4-41	Model standard deviation of the AE 4 fluxes as a function of energy plotted for constant L .	4-71
4-42	Model standard deviation of the AE 4 fluxes as a function of L plotted for constant energy.	4-72
4-43	Comparison of AE 4 model B dependence with Azur data at $L = 3.0, 4.0,$ and 5.5 .	4-73
4-44	Comparison of AE 4 model electron spectrum with various data at $L = 6.6$.	4-74
4-45	Comparison of AE 4 model spectrum with Azur data at $L = 4.0$ and $B = 0.14$ gauss.	4-75
4-46	Comparison of AE 4 radial profile with OV1-19 data at $B = 0.05$ gauss.	4-76
4-47	Model radial profiles for 250-KeV electrons in the inner zone.	4-77
4-48	Model radial profiles for 500-KeV electrons in the inner zone.	4-78
4-49	Model radial profiles for 1-MeV electrons in the inner zone.	4-79

4 January 1977

FIGURE	TITLE	PAGE
4-50	Relative importance of the Starfish and quiet-day flux components as a function of time for energy between 292 and 690 KeV at L = 1.5 and 1.9.	4-80
4-51	Ratio, R_T , of the integral flux ($E > 500$ KeV) in October 1967 to the corresponding flux in various phases of the solar cycle.	4-81
4-52	Nomograph map for AE 5 (1975) model fluxes of electrons with $E > 500$ KeV.	4-82
4-53	Nomograph map for AE 6 model fluxes of electrons with $E > 500$ KeV.	4-83
4-54	Comparison of inner zone model spectra with various data at L = 1.4.	4-84
4-55	Comparison of inner zone model spectra with various data at L = 1.6.	4-85
4-56	Composite equatorial radial profiles of the overall environment models for electrons with $E > 500$ KeV.	4-86
4-57	Orbit-integrated fluxes (1-day fluences) of >500 -KeV electrons as a function of orbital altitude for inclinations of 30 and 90 degrees.	4-87
4-58	Particle substorm events observed by ATS 1 spectrometer.	4-88
4-59	Comparison of the theoretical Coulomb-scattering loss with the measured decay time of electrons from 300 KeV to 5 MeV.	4-89
4-60	Hourly average of local noon electron count rates as observed by ATS 6 and ATS 1 in the autumn of 1974 and spring of 1975.	4-90
4-61	Comparison of the Injun 5 electron spectrum with the model spectrum computed by assuming a 400-volt potential difference along a magnetic field line and an ambient Maxwellian electron distribution of temperature of 800 eV and density of 5 cm^{-3} .	4-91
4-62	Composite map of low-energy electrons.	4-92
4-63	Differential energy spectra of alpha particles at selected L values between 1.525 and 2.125 plotted on the same intensity scale for $B/B_0 = 1.3$.	4-93

4 January 1977

FIGURE	TITLE	PAGE
4-64	Alpha particle spectra (differential flux versus total energy) for $B = 0.10$ gauss and $L = 2.5, 2.7,$ and 2.9 .	4-94
4-65	B-L plots of five alpha particle channels.	4-95
4-66	B-L contours of alpha particles with energies between 1.18 and 8.0 MeV from 11 through 28 February 1970.	4-96
4-67	The radial profile of J_{α} ($0.91 < E_{\alpha} < 2.00$ MeV) inferred from the response of the $\Delta\alpha 2$ channel.	4-97
4-68	Average J_{α}/J_p versus L for five ranges of energy per nucleon (E/A).	4-98
4-69	Daily averages of intensity for protons in the energy range of $0.31 \leq E_p \leq 0.45$ and alpha particles in the range of $0.30 \leq E_{\alpha} \leq 2.0$ MeV/nucleon, at $L = 3.05 \pm 0.05$ and $B = 0.19 \pm 0.01$ for the entire period for available Injun 5 data.	4-99
5-1	Ranges of electrons and protons in the air.	5-6
5-2	Electron number densities in the atmosphere.	5-8
5-3	The path of a light-charged particle (an electron) in a fully ionized gas.	5-17
5-4	Functions used in computing Fokker-Planck coefficients for the slowing and deflection of a charged particle in an ionized gas.	5-19
5-5	Diffusion of a group of electrons in energy, pitch angle space.	5-27
5-6	The intersection of a pitch angle cone with the earth's surface.	5-30
5-7	Equatorial pitch angle dependence of the average injection coefficient $\bar{\eta}$ for an isotropic neutron flux emerging from the atmosphere.	5-31
5-8	Energy dependence of average albedo neutron injection coefficient.	5-32

4 January 1977

FIGURE	TITLE	PAGE
5-9	Neutron decay rate contours near the earth.	5-36
5-10	Total magnetic field energy in the volume contained between the earth's surface and a shell of field lines at $L = R_0/R_E$.	5-38
5-11	The stability function, $d(j_0/p^2)/dL$, integrated over J , the second adiabatic invariant, for the Starfish trapped electron belts.	5-43
5-12	Latitude-dependent part of the radial diffusion coefficient.	5-50
5-13	Decay time constants of the Starfish trapped electron belts.	5-53
5-14	Radial diffusion coefficients for electrons with 90-degree equatorial pitch angles.	5-55
5-15	Decay time parameters for trapped electrons on intermediate L-shells.	5-56
5-16	Inward motion of trapped electrons during a period of 9 days.	5-57
5-17	Relative phases of wave field vectors in a circularly polarized wave.	5-65
5-18a	Velocity space trajectories of a proton interacting with circularly polarized waves.	5-68
5-18b	Velocity space trajectories of a proton interacting with circularly polarized waves.	5-69
5-19a	The ratio of plasma frequency-squared to electron gyro-frequency-squared, on the morning and dayside of the magnetosphere.	5-73
5-19b	The ratio of plasma frequency-squared to electron gyro-frequency-squared, on the evening and nightside of the magnetosphere.	5-74
5-20	The relativistic resonance conditions for electrons interacting with circularly polarized waves in an electron-proton plasma.	5-77
5-21	The relativistic resonance conditions for protons interacting with circularly polarized waves in an electron-proton plasma.	5-78

4 January 1977

FIGURE	TITLE	PAGE
5-22	The minimum phase velocity and minimum resonant electron momentum for ion-cyclotron waves as a function of β $\frac{2Q(T)_{avg}}{3m_e c^2} = \frac{2QT}{m_e c^2}$.	5-80
5-23a	The functions of G_1 and G_2/G_1 used in evaluating the wave amplification rates of Equation 5-140b; $\nu = 0$.	5-88
5-23b	The functions of G_1 and G_2/G_1 used in evaluating the wave amplification rates of Equation 5-140b; $\nu = 2$.	5-89
5-23c	The functions of G_1 and G_2/G_1 used in evaluating the wave amplification rates of Equation 5-140b; $\nu = 4$.	5-90
5-23d	The functions of G_1 and G_2/G_1 used in evaluating the wave amplification rates of Equation 5-140b; $\nu = 6$.	5-91
5-24	Limits on trapping of high-energy electrons.	5-96
5-25a	Sample diffusion coefficients for electrons at $L = 2$.	5-98
5-25b	Sample diffusion coefficients for electrons at $L = 3$.	5-99
5-25c	Sample diffusion coefficients for electrons at $L = 4$.	5-100
5-25d	Sample diffusion coefficients for electrons at $L = 5$.	5-101
5-26a	The amplification rates of whistler-waves as a function of frequency for a $(\sin \alpha_p)$ pitch-angle distribution.	5-104
5-26b	The amplification rates of whistler-waves as a function of frequency for a $(\sin \alpha_p)^2$ pitch-angle distribution.	5-105
5-27	Convection in the equatorial plane of the magnetosphere.	5-108
6-1	Time sequence of measurements of (1) true counts versus L , (2) count rate ratios versus L , and (3) true counts versus $\log B$ for the Teak enhancement 0.3 hours after the detonation.	6-5
6-2	Time sequence of measurements of (1) true counts versus L , (2) count rate ratios versus L , and (3) true counts versus $\log B$ for the Teak enhancement 24 hours after the detonation.	6-6
6-3	Time sequence of measurements of (1) true counts versus L , (2) count rate ratios versus L , and (3) true counts versus $\log B$ for the Teak enhancement 43 hours after the detonation.	6-7

4 January 1977

FIGURE	TITLE	PAGE
6-4	Buildup and decay of Teak enhancement.	6-11
6-5	Argus 1 trapping 1.80 hours after T_E ; data were acquired at Huntsville.	6-16
6-6	Argus 1 trapping 25.48 hours after T_E ; data were acquired at Huntsville.	6-17
6-7	Sample of observed unidirectional count rate versus θ (angle between counter axis and plane perpendicular to B)—Argus 1, 1.80 hours after T_E .	6-18
6-8	Unidirectional flux density versus θ [angle between $j(\theta)$ and plane perpendicular to B]—distributions for Argus 1, $T_E + 25.48$ hours.	6-19
6-9	Decay of unidirectional peak flux density $j(\theta)_{\max}$ perpendicular to B for Argus 1.	6-21
6-10	Summary of omnidirectional data for Argus 1.	6-22
6-11	Summary of omnidirectional data for Argus 2.	6-23
6-12	Summary of omnidirectional data for Argus 3.	6-24
6-13	Counting rates of detectors on rocket flight 2024 versus flight time.	6-28
6-14	Time rate of decay of electron flux for Event 2.	6-30
6-15	Flux contours 10 hours after Starfish, as determined from Injun I data.	6-32
6-16	Flux contours 2 days after Starfish, as determined from Telstar data by Newkirk and Walt.	6-35
6-17	Comparison of omnidirectional fluxes in the geomagnetic equatorial plane as a function of L, several months after Starfish.	6-37
6-18	Experimental spectra of radiation belt electrons following Starfish.	6-38
6-19	Counting rate data from Injun I and Injun III following Starfish.	6-41
6-20	Omnidirectional counting rate data from Telstar following Starfish.	6-42
6-21	Comparison of experimental and theoretical values for the time decay of the Starfish radiation belt.	6-44

4 January 1977

FIGURE	TITLE	PAGE
6-22	Field lines in the meridian plane passing through Johnston Island.	6-45
6-23	Omnidirectional flux ($\text{cm}^{-2} \text{sec}^{-1}$) contours (Telstar data) immediately following the Russian test of 22 October 1962.	6-48
6-24	Omnidirectional flux ($\text{cm}^{-2} \text{sec}^{-1}$) contours (Telstar data) immediately following the Russian test of 28 October 1962.	6-50
7-1	Contours of omnidirectional flux that would result from complete saturation of the closed trapping region (out to $L \sim 6$).	7-10
7-2	The trapping fraction as a function of injection altitude.	7-11
7-3	Omnidirectional flux of untrapped electrons in the beta tube as a function of location on the associated field lines.	7-16
7-4	The integrand of Equation 7-20a.	7-19
7-5	The drift dilution of a group of electrons injected instantaneously in a longitudinal segment of finite width.	7-21
7-6	The drift dilution of a group of electrons injected instantaneously in a longitudinal segment of finite width.	7-23
7-7	The drift dilution of a group of electrons injected instantaneously in a longitudinal segment of finite width.	7-25
7-8	The function that is proportional to the contribution of electrons injected at a point B to the total omnidirectional flux.	7-29
8-1	Normalized damage coefficients for p-type silicon.	8-12
8-2	Typical solar cell assembly.	8-14
8-3	Diffusion length damage coefficient K_L at five cell temperatures (Reference 64).	8-16
8-4	Normalized 10 ohm - centimeter n/p cell degradation at 27°C for normal incidence 1-MeV electrons.	8-18
8-5	Normalized 2 ohm - centimeter n/p cell degradation at 27°C for normal incidence 1-MeV electrons.	8-19
8-6	Planar transistor construction (schematic).	8-22

4 January 1977

FIGURE	TITLE	PAGE
8-7	Nomograph for obtaining variation in grounded emitter current gain of silicon NPN transistors with equivalent 1-MeV electron fluence.	8-25
8-8	Degradation of Fairchild-type 2N1711 transistors versus test collector current at gamma ray dose of 5×10^4 rads.	8-27
8-9	Degradation of Fairchild-type 2N1711 transistors versus dose of Cobalt-60 gamma rays, showing effect of irradiation bias and deviation from linearity.	8-27
8-10	Normalized leakage and saturation parameters versus electron irradiation for bipolar type 2N930 and junction FET type FE200 transistors.	8-29
8-11	MIS transistor.	8-30
8-12	Generalized form of shift in MIS transistor characteristics as a function of irradiation (Reference 65).	8-32
8-13	Radiation resistance of field-effect transistors (FE200 type) and bipolar transistors (2N930 type) under 1-MeV electron irradiation.	8-33
8-14	Dielectrically isolated junction field effect transistor.	8-35
8-14A	Complementary MOS (CMOS) inverter.	8-35A
8-14B	Change in CMOS inverter transfer characteristic for input high condition. (Gate bias on p-channel is 0 volts, +10 volts on n-channel. $V_{DD} = +10$ volts.) (Reference 68).	8-35B
8-14C	Change in CMOS inverter transfer characteristic for input low condition. (Gate bias on p-channel is +10 volts, 0 volt on n-channel. $V_{DD} = +10$ volts.) (Reference 68).	8-35B
8-14D	Threshold-voltage shift as a function of radiation-dose at 2 different bombardment biases for MIS transistors possessing various gate-insulator materials (Reference 33).	8-35D
8-15	Change in solar absorptance due to protons.	8-40
8-16	Absolute change in solar absorptance as a function of 2-KeV proton fluence.	8-41
8-17	Daily dose (natural electrons) in circular orbit satellites as a function of satellite altitude for specified orbital inclination and shielding thickness (inclination = 0 degree).	8-48

4 January 1977

FIGURE	TITLE	PAGE
8-18	Daily dose (natural electrons) in circular orbit satellites as a function of satellite altitude for specified orbital inclination and shielding thickness (inclination = 30 degrees).	8-49
8-19	Daily dose (natural electrons) in circular orbit satellites as a function of satellite altitude for specified orbital inclination and shielding thickness (inclination = 60 degrees).	8-50
8-20	Daily dose (natural electrons) in circular orbit satellites as a function of satellite altitude for specified orbital inclination and shielding thickness (inclination = 90 degrees).	8-51
8-21	Daily dose (natural protons) in circular orbit satellites as a function of satellite altitude for specified orbital inclination and shielding thickness (inclination = 0 degree).	8-53
8-22	Daily dose (natural protons) in circular orbit satellites as a function of satellite altitude for specified orbital inclination and shielding thickness (inclination = 30 degrees).	8-54
8-23	Daily dose (natural protons) in circular orbit satellites as a function of satellite altitude for specified orbital inclination and shielding thickness (inclination = 60 degrees).	8-55
8-24	Daily dose (natural protons) in circular orbit satellites as a function of satellite altitude for specified orbital inclination and shielding thickness (inclination = 90 degrees).	8-56
8-25	Daily omnidirectional flux of fission electrons on circular orbit satellites as a function of satellite altitude for specified orbital inclinations (1-megaton fission yield injection at 200 kilometers, $L = 5.0$).	8-59
8-26	Daily omnidirectional flux of fission electrons on circular orbit satellites as a function of satellite altitude for specified orbital inclinations (1-megaton fission yield injection at 200 kilometers, $L = 4.0$).	8-60
8-27	Daily omnidirectional flux of fission electrons on circular orbit satellites as a function of satellite altitude for specified orbital inclinations (1-megaton fission yield injection at 200 kilometers, $L = 3.0$).	8-61
8-28	Daily omnidirectional flux of fission electrons on circular orbit satellites as a function of satellite altitude for specified orbital inclinations (1-megaton fission yield injection at 200 kilometers, $L = 2.0$).	8-62

4 January 1977

FIGURE	TITLE	PAGE
8-29	Daily omnidirectional flux of fission electrons on circular orbit satellites as a function of satellite altitude for specified orbital inclinations (1-megaton fission yield injection at 200 kilometers, $L = 1.15$).	8-63
8-30	Daily omnidirectional flux of fission electrons on circular orbit satellites as a function of satellite altitude for specified orbital inclinations (saturation condition, $\beta = 1.0$).	8-64
8-31	Electron and bremsstrahlung depth dose for fission electrons as a function of thickness of aluminum.	8-65
8-32	Electron dose nomograph.	8-66
8-33	Bremsstrahlung number and energy spectra resulting from a fission electron spectrum normally incident on a thick aluminum target.	8-69
8-34	Daily fluence of equivalent 1-MeV electrons (for natural trapped electron environment) in circular orbit satellites as a function of satellite altitude for specified orbital inclinations and shielding thicknesses (inclination = 0 degree).	8-72
8-35	Daily fluence of equivalent 1-MeV electrons (for natural trapped electron environment) in circular orbit satellites as a function of satellite altitude for specified orbital inclinations and shielding thicknesses (inclination = 30 degrees).	8-73
8-36	Daily fluence of equivalent 1-MeV electrons (for natural trapped electron environment) in circular orbit satellites as a function of satellite altitude for specified orbital inclinations and shielding thicknesses (inclination = 60 degrees).	8-74
8-37	Daily fluence of equivalent 1-MeV electrons (for natural trapped electron environment) in circular orbit satellites as a function of satellite altitude for specified orbital inclinations and shielding thicknesses (inclination = 90 degrees).	8-75
8-38	Daily fluence of equivalent 1-MeV electrons (for natural trapped proton environment) in circular orbit satellites as a function of satellite altitude for specified orbital inclinations and shielding thicknesses (inclination = 0 degree).	8-77

4 January 1977

FIGURE	TITLE	PAGE
8-39	Daily fluence of equivalent 1-MeV electrons (for natural trapped proton environment) in circular orbit satellites as a function of satellite altitude for specified orbital inclinations and shielding thicknesses (inclination = 30 degrees).	8-78
8-40	Daily fluence of equivalent 1-MeV electrons (for natural trapped proton environment) in circular orbit satellites as a function of satellite altitude for specified orbital inclinations and shielding thicknesses (inclination = 60 degrees).	8-79
8-41	Daily fluence of equivalent 1-MeV electrons (for natural trapped proton environment) in circular orbit satellites as a function of satellite altitude for specified orbital inclinations and shielding thicknesses (inclination = 90 degrees).	8-80
8-42	Equivalent 1-MeV electron fluence as a function of aluminum shield thickness produced by unit fluence of fission beta electrons incident on shield.	8-81
9-1	Coordinate system for an electron in circular motion.	9-3
9-2	Examples of radiation patterns (total power) at various electron energies.	9-4
9-3	Total power radiated by a high-energy electron ($\gamma^2 \gg 1$) at the n^{th} harmonic of the gyro-frequency.	9-6
9-4	Normalized spectrum of a high-energy electron ($\gamma^2 \gg 1$) when $\nu \gg \nu_c$, $\alpha = 90$ degrees, and $\Psi = 0$.	9-9
9-5	Power (per hertz per ster) radiated in the orbital plane ($\Psi = 0$) by electrons in circular motion ($\alpha = 90$ degrees) with energies of 128 KeV to 40 MeV.	9-11
9-6	Examples of the variation of W_ψ (ψ) with electron energy and the frequency of observation.	9-13
9-7	Examples of the variation of the beamwidth (with respect to ψ) of the radiation from a high-energy electron.	9-15
9-8	Effect of changes in the pitch angle α on the spectrum of a 10-MeV electron.	9-17
9-9	Density of electrons versus height over the magnetic equator in earth radii.	9-20

4 January 1977

FIGURE	TITLE	PAGE
9-10	Emission coefficient $q(x, \nu)$ versus height (in earth radii) over the magnetic equator for frequencies of 30, 50, and 100 MHz.	9-22
9-11	Comparison of synchrotron noise from Starfish electrons with cosmic noise and lightning storm noise.	9-23
9-12	Observational geometry for an observer on the geomagnetic equator (A) and at 45-degree geomagnetic latitude (B).	9-24
9-13	30-MHz emission coefficient $q(x, \nu)$ as a function of the intersection of the ray path with a sequence of L-shells.	9-27
9-14	Brightness temperature T_B versus frequency for three zenith distances (Δ).	9-28
9-15	30-MHz emission coefficient $q(x, \nu)$ as a function of the intersection of the ray path with a sequence of L-shells.	9-30
9-16	Brightness temperature T_B versus frequency for four zenith distances (Δ).	9-31
11-1	Mass distribution for fission of U^{235} , U^{238} , and Pu^{239} .	11-7
11-2	Average beta energy for U^{235} as a function of time.	11-10
11-3	Fission spectra at different times after instantaneous fission and the equilibrium fission spectrum.	11-11
11-4	Rate of beta decay following fission for U^{235} , U^{238} and Pu^{239} .	11-12
11-5	Distribution of major constituents of neutral atmosphere at local times $t = 21$ or 8 hours (diurnal average) for average solar activity ($S' = 125$ RU).	11-18
11-6	Distributions of major constituents of neutral atmosphere at extremes of diurnal variation for average solar activity ($S' = 125$ RU).	11-19
11-7	Distributions of major constituents of neutral atmosphere at extremes of solar activity.	11-20

4 January 1977

FIGURE	TITLE	PAGE
11-8	Distributions of free electrons in atmosphere at extremes of diurnal and solar cycle variations.	11-31
11-9	Typical measurements of proton distributions at geomagnetic latitudes of 0°N, 35°N, and 40°N from 2,000 to 30,000 kilometers.	11-33
11-10	Initial orbital inclinations of U.S. and Russian satellites.	11-51

4 January 1977

TABLES

TABLE	TITLE	PAGE
2-1	Spherical harmonic coefficients (gammas) of the geomagnetic field for epoch 1960.	2-20
2-2	Tabular values of invariant latitude Λ (degrees) versus L.	2-25
2A-1	Ranges of R (in gammas) that define K on a quasi-logarithmic scale.	2-37
2A-2	Equivalent amplitude a_p versus K_p .	2-38
3A-1	Fundamental electrical and magnetic equations.	3-48
3A-2	Electric and magnetic unit conversion factors.	3-49
3B-1	Important charged particle parameters in a dipole field.	3-52
4-1	Omnidirectional flux confidence codes for AE 5 (1975 projected).	4-15
4-2	Omnidirectional flux confidence codes for AE 6.	4-15
5-1	Excitation ionization potentials.	5-9
5-2	Energy loss lifetimes of trapped particles with pitch angles near 90 degrees.	5-22
6-1	High-altitude nuclear detonations.	6-2
6-2	Summary of Teak data at times after the event time T_E .	6-8
6-3	Summary of Orange data at times after the event time T_E .	6-9
6-4	Characteristics of three Explorer 4 detectors.	6-14
6-5	Summary of unidirectional data for Argus 1 and Argus 2.	6-15
6-6	Sounding rocket launches.	6-27
6-7	Argus injection efficiencies.	6-30

4 January 1977

TABLE	TITLE	PAGE
6-8	Principal Starfish measurements.	6-33
6-9	Electron inventories for Starfish.	6-40
6-10	Electron inventories for the USSR tests.	6-53
8-1	Comparison of theoretical displacement parameters with measured carrier removal in silicon.	8-9
8-2	Cover slide transmission losses due to radiation.	8-45
10-1	Dose limits of radiation exposure.	10-2
11-1	Summarization of radiation belt detectors.	11-5
11-2	Main regions of the earth's atmosphere.	11-13
11-3	Lower atmosphere average neutral properties versus altitude (spring or fall; latitude 45 degrees).	11-14
11-4	Upper atmosphere neutral properties versus altitude near sunspot minimum (spring or fall; latitude 45 degrees; $t = 21$ hours; diurnal average).	11-21
11-5	Upper atmosphere neutral properties versus altitude near sunspot minimum (spring or fall; latitude 45 degrees; $t = 5$ hours; diurnal minimum).	11-22
11-6	Upper atmosphere neutral properties versus altitude near sunspot minimum (spring or fall; latitude 45 degrees; $t = 14$ hours; diurnal maximum).	11-23
11-7	Upper atmosphere neutral properties versus altitude for average sunspot conditions (spring or fall; latitude 45 degrees; $t = 21$ hours; diurnal average).	11-24
11-8	Upper atmosphere neutral properties versus altitude for average sunspot conditions (spring or fall; latitude 45 degrees; $t = 5$ hours; diurnal minimum).	11-25
11-9	Upper atmosphere neutral properties versus altitude for average sunspot conditions (spring or fall; latitude 45 degrees; $t = 14$ hours; diurnal maximum).	11-26
11-10	Upper atmosphere neutral properties versus altitude near sunspot maximum (spring or fall; latitude 45 degrees; $t = 21$ hours; diurnal average).	11-27
11-11	Upper atmosphere neutral properties versus altitude near sunspot maximum (spring or fall; latitude 45 degrees; $t = 5$ hours; diurnal minimum).	11-28

4 January 1977

TABLE	TITLE	PAGE
11-12	Upper atmosphere neutral properties versus altitude near sunspot maximum (spring or fall; latitude 45 degrees; $t = 14$ hours; diurnal maximum).	11-29
11-13	Proton concentration versus altitude and geomagnetic latitude.	11-34
11-14	Number of U.S. spacecraft launched per year on various missions.	11-51
11-15	Number of foreign spacecraft launched per year by various countries.	11-52

4 January 1977

AUTHORS

- Section 1. John B. Cladis, Lockheed Palo Alto Research Laboratory.
- Section 2. Lester L. Newkirk, Lockheed Palo Alto Research Laboratory.
- Section 3. Gerald T. Davidson, Lockheed Palo Alto Research Laboratory.
- Section 4. K. W. Chan, D. M. Sawyer, and J. I. Vette, NASA—Goddard Space Flight Center.
- Section 5. Gerald T. Davidson, Lockheed Palo Alto Research Laboratory.
- Section 6. Martin Walt, Lockheed Palo Alto Research Laboratory.
- Section 7. Gerald T. Davidson, Lockheed Palo Alto Research Laboratory and Roy W. Hendrick, Jr., General Electric—TEMPO.
- Section 8. David L. Crowther, William H. Harless, Jr., and J. W. Schallau, Lockheed Palo Alto Research Laboratory.
- Section 9. A. M. Peterson and J. F. Vesecky, Stanford Research Institute.
- Section 10. John B. Cladis and Billy M. McCormac, Lockheed Palo Alto Research Laboratory.
- Section 11. "Supplementary Topics:"
- Section 11. 1. George H. Nakano, Lockheed Palo Alto Research Laboratory.
- Section 11. 2. Charles H. Humphrey, Lockheed Palo Alto Research Laboratory.
- Section 11. 3. Albert D. Anderson, Lockheed Palo Alto Research Laboratory.

xxxix

4 January 1977

Section 11.4. Fred H. Sage, III, General Electric-TEMPO.

Section 11.5. Lester L. Newkirk, Lockheed Palo Alto Research
Laboratory.

Section 12. John B. Cladis, Lockheed Palo Alto Research Laboratory.

4 January 1977

SECTION 4

TRAPPED RADIATION POPULATION

K.W. Chan, D.M. Sawyer, and J.I. Vette,
NASA—Goddard Space Flight Center

4.1 INTRODUCTION

This section contains a description of the charged particles within the magnetosphere. The emphasis, however, is on those fluxes found within the stably trapped region since their energetic nature usually makes them of primary concern to spacecraft designers. A complete description of a particle population requires a knowledge of the particle flux and energy spectrum as a function of time, spatial position, and orientation of the measuring device. In those regions of the magnetosphere where the particle motion obeys adiabatic invariants, the orientation and position variables are connected through the invariants. Since the particle fluxes depend heavily upon all the variables, and there is no theory to completely unify the diverse behavior of these variables, a concise quantitative treatment is very difficult. The adiabatic theory (e.g., Reference 1) and the diffusion theory (e.g., Reference 2) have provided the major framework for explaining many of the observed phenomena. (Also see Sections 3 and 5.)

A large number of satellite measurements have been made since the first radiation belt observations in 1958. These have provided enough data to form a good phenomenological picture of many magnetospheric processes. Several books and proceedings of symposia, as well as review articles, are available to those interested in becoming acquainted with the observations and theories (References 2 through 10). Since these contain references to most of the original work, no attempt is made in this section to provide an extensive bibliography. Many general ideas are stated without specific reference.

Unlike the interplanetary medium, the magnetic field within the magnetosphere is usually strong enough to dominate the particle motion. This situation is obtained when the magnetic energy density ($B^2/8\pi$) exceeds the particle kinetic energy density ($nmv^2/2$). However, in the magnetosheath region and in parts of the geomagnetic tail, the balance of control can fluctuate between particles and fields.

4 January 1977

Moving inward toward the Earth, the field becomes well ordered and stable enough to serve as a coordinate system for particle motion. It is in this region that the natural radiation belt particles reside and in which the three adiabatic invariants of gyration, bounce, and drift are well defined.

Within the belts are electrons, protons, and heavier ions with energies from a few eV in the thermal plasma region to a few MeV for electrons and to several hundred MeV for protons. Extensive observations have been made of both the electron and proton populations. Their different morphological structure and behavior make it convenient to discuss them in separate subsections. Similarly, a separate subsection is reserved for the observations of $Z \geq 2$ ions. The final subsection is a brief summary.

4.2 TRAPPED PROTON ENVIRONMENT

4.2.1 Protons with $E \geq 100$ KeV

The stable trapping region is defined as that volume of the magnetosphere where the drift paths of the particles form closed shells around the Earth. At L values beyond 5, these shells become noticeably distorted by the asymmetry of the Earth's field, which in turn is caused by the solar wind pressure. In this region, the local time becomes important as an additional parameter necessary for a complete description of the trapped fluxes. Figure 4-1 shows the trapping regions in the noon to midnight meridian for a model magnetosphere with this asymmetry.

Out to the distance of the synchronous orbit near $L = 6.6$, the proton environment can be described, for most purposes, without the local time variable. However, Stevens et al. (Reference 11) have observed a factor-of-four variation in the quiet time fluxes of 0.6- to 3.3-MeV protons between noon and midnight at $L = 6.6$.

Sawyer and Vette (Reference 12) have recently (1976) completed a comprehensive model of the trapped proton environment out to $L = 6.6$ for energies above 100 KeV. This environment can be viewed as a summary of the many different measurements by numerous investigators. It is composed of two parts, designated AP8MIN and AP8MAX, which correspond to solar minimum and solar maximum conditions, respectively. This division results from the cyclic nature of the trapped flux at low altitudes, which varies in correspondence with the 11-year solar cycle. This variation is discussed later

4 January 1977

in more detail. Figures 4-2 through 4-7 present B-L flux maps of the AP8MIN and AP8MAX models for six different energies between 0.1 and 400 MeV. These fluxes are omnidirectional and integral in energy. AP8MAX differs from AP8MIN for altitudes less than about 1,000 kilometers, and for L values less than 2.9. The limit at $L = 2.9$ is the result of insufficient data at higher L values on which to base any solar-cycle variation. The absolute accuracy of the solar-cycle effect in the AP8 models is somewhat uncertain since the steep spatial gradients in the fluxes are difficult to determine accurately and consistently.

The equatorial distribution of the protons as obtained from the AP8MIN model is shown in Figure 4-8. It is apparent from the figure that there is only one proton radiation belt, which is in sharp contrast to the two-belt structure observed for electrons described in the next subsection. The flux above 5-MeV peaks within $L = 1.8$ and the flux above 0.1 MeV peaks at about $L = 3.2$.

The nature of the AP8MIN omnidirectional integral spectra is shown in Figures 4-9 through 4-16. Each figure corresponds to one L value and contains the spectra for several B/B_0 values, where B_0 is the equatorial B field value. An inflection point around 30 MeV in the equatorial spectrum at $L = 1.5$ is apparent in Figure 4-10. This is suggestive of different source or loss mechanisms predominating above and below 30 MeV. It is fairly well established that the source of the higher energy protons is the neutron flux produced in the atmosphere by incident cosmic rays, and the lower energy protons are primarily due to radial diffusion transport from more distant regions of the magnetosphere. It is interesting to note that the higher energy protons typically have lifetimes of hundreds of years (Reference 13). Reasonable agreement exists between the observations of the equatorial proton flux with energies above 10 MeV for L values from 1.18 to 1.7, and the solution of an inhomogeneous radial diffusion equation with the proper source and loss terms (References 13 through 16). The same situation does not yet hold for the remainder of the stable trapping region.

The word stable is not meant to imply the absence of time variations, as we have already noted with the solar-cycle variations. These time variations are ultimately related to particles and electromagnetic waves emitted by the sun as well as to solar magnetic field variations which interact with the Earth's magnetic field and atmosphere. As one looks to higher L values and, correspondingly, lower energies, time variations generally become more pronounced.

4 January 1977

The mechanism of the proton solar-cycle variation is reasonably well understood. A cyclic solar emission drives an atmospheric density variation which causes a corresponding variation in the fluxes of protons mirroring in the atmosphere at altitudes below about 1,000 kilometers (References 17 through 19). Observations of proton fluxes in a narrow range of minimum mirror point altitudes (designated h_{MIN}) over a period of several years have shown variations which are consistent with predictions. Figure 4-17 shows the time dependence of the omnidirectional, 60-MeV (differential) flux at the three h_{MIN} altitudes of 250, 350, and 450 kilometers (Reference 19). Also shown are the corresponding theoretical predictions. The good agreement between observations and theory lends considerable confidence to our understanding of the basic mechanisms involved.

The extensive coverage of the satellite 1963-38C has provided particularly useful data regarding long-term time variations for L values up to 3 (Reference 19). Figures 4-18 through 4-21 show 10-day averages over 5 years of the 1963-38C proton counting rates in the energy ranges of 25 to 100 MeV, 8.2 to 25 MeV, 2.2 to 8.2 MeV, and 1.2 to 2.2 MeV. Fluxes at energies above 25 MeV are very stable for L values less than 2 while some response to major geomagnetic storms, such as September 1963 and May 1967, can be seen at $L = 2.2$. The lower energies show an observable response to even minor storms, with decay times on the order of months to years. There is also some evidence in these figures for long-term decreases in the fluxes with decay times on the order of 3 to 7 years.

An example of the time behavior of protons at $L = 4$ (Reference 20) is shown in Figure 4-22. These curves are for protons mirroring at the equator with energies above eight threshold values. The curves labeled A through H correspond to the threshold energies of 98, 134, 180, 345, 513, 775, 1,140, and 1,700 KeV, respectively. The curves are displaced to avoid overlap, and the values must be multiplied by 10 raised to the power $-1.25, -1.00, -0.75, -0.50, -0.25, 0.25, 0.25,$ and 0.25 for curves A through H, respectively. The result is the integral intensity in protons/cm²-sec-ster. Also plotted are the hourly Dst values which are magnetic field changes related to changes in the total energy of particles trapped in the radiation belt (see subsection 4.2.2). Some of the variations seen in these protons represent adiabatic changes consistent with the magnetic field changes.

Order of magnitude fluctuations in the fluxes are observable in Azur satellite data at $L = 4.85$ and $B = 0.17$ gauss. These proton

4 January 1977

fluxes for energy intervals between 0.25 to 0.5, 0.5 to 1.0, and 1.0 to 1.65 MeV are shown in Figure 4-23 (Reference 21). Above $L = 5$, order-of-magnitude fluctuations have been observed on time scales as short as 10 minutes (Reference 22). At the synchronous orbit and beyond, the particle population exhibits extremely dynamic behavior (Reference 19). Occasionally, the Earth's magnetospheric boundary is compressed by the solar wind to less than $6.6 R_E$ on the noon side, resulting in the disappearance of the higher energy (~ 1 MeV) trapped particles. Solar protons also have easy access to the synchronous region, especially during disturbed times (Reference 23). A more extensive discussion of time variations for the protons modeled by AP8 is contained in Reference 12.

4.2.2 Protons with $E < 100$ KeV

We now turn attention to the observations of protons with energies less than 100 KeV in the stable trapping region. Increases in the fluxes of these protons have been thought to be largely responsible for the decreases of the magnetic field intensities measured at the Earth's equator during main-phase geomagnetic storms (References 24 and 25). However, recent observations of ions heavier than protons and storm particle decay times have cast some doubt on the identification of those particles as protons. This possibility is discussed more fully in subsection 4.4.3.

The magnetic activity index Dst is a measure of geomagnetic-storm field decreases and is, therefore, closely related to the particle increases which constitute the bulk of the storm time ring current. It is generally believed that the source of these particles is the convection of plasma sheet protons to low L values (References 26 and 27). Since a comprehensive model of the distribution and time dependence of these fluxes is not currently available, figures from the published works of various investigators are presented.

Figure 4-24 shows unidirectional differential energy spectra at the magnetic equator for L values of 4.5, 5.0, and 6.0 (Reference 28). The flux values peak near 10 KeV, with intensities of approximately 10^3 protons/cm²-sec-ster-eV. These data are a composite of results from the spacecraft OGO 3, Explorer 12, and Mariner 4. The spectrum below 100 KeV is seen to merge smoothly with observations above 100 KeV, and an empirical expression which fits the data is also shown. The fluxes with energies below 50 KeV were acquired aboard OGO 3 during June and July 1966, with measurements during two moderate main-phase geomagnetic storms excluded (Reference 28).

4 January 1977

The effects of storms of these low-energy protons can be seen in Figure 4-25 (Reference 29). These results were acquired during 1800 to 2400 local times aboard the Explorer 45 (S³) satellite in December 1971. The quantity plotted is two times the proton mass times the phase space distribution function, which in the nonrelativistic limit is equal to j/E , where j is the equatorial (differential) flux at 90 degrees pitch angle, in units of protons/cm²-sec-ster-KeV, and E is the energy in KeV. This quantity is plotted as a function of time at constant energy and at constant first invariant μ ($\mu = E_{\perp}^2/B$) for radial distances between 2.5 and 5. The storm on 17 December is evident in the lower energy fluxes and in the Dst index, which is also shown. Notice that the higher energy particles at constant μ show no intensity decreases in association with the storm main phase, which is indicative of adiabatic behavior (Reference 29). Prestorm particle intensities shown at energies ≤ 26 KeV are upper limits to the true intensities at radial distances less than 3.5 as a result of a detector background problem. Extensive pitch-angle distributions for these same data are contained in Reference 30.

4.3 TRAPPED ELECTRON ENVIRONMENT

4.3.1 Morphology of Energetic Electrons ($E \geq 40$ KeV) in the Trapping Region of the Geomagnetic Field

The electron population in the terrestrial environment is found to encompass two zones (the inner and outer radiation zones, or the Van Allen belts) of enhanced intensity in the distorted dipole magnetic field of the Earth. An overview of the radiation environment is illustrated by the isoflux contour map of Figure 4-26, which was constructed by compiling measurements of electrons with energies greater than 0.5 MeV (Reference 31). The regions having omnidirectional flux intensities greater than 10^6 electrons/cm²-sec are shaded to show the two-belt configuration of the energetic electrons trapped in the vicinity of the Earth.

There is abundant literature available on the electrons within the Van Allen radiation zones. It has been well established that the inner- and outer-zone electrons have remarkable differences in temporal and spatial fluctuations. Figure 4-27 is an example of the long-term observation of the $E \geq 0.28$ -MeV electrons in the inner zone over the period of more than 5 years, as recorded by satellite 1963-38C. The data are 10-day averages of the counting rate. The main feature in the time-history profile is a steady monotonic decrease with time for L shells between $L = 1.2$ to $L = 1.8$, showing

4 January 1977

the decay of the artificial electrons injected by the Starfish detonation in July 1962 (also see Sections 5 and 6). For the outer edge of the inner zone, $L = 2.2$, the flux enhancements associated with the magnetic storms are clearly the dominant effect in the time history. The greater the magnetic disturbances, as indicated by the magnitude of the Dst index in the bottom panel, the lower the L shells in the inner zone that will be affected.

In contrast to this phenomenon in the inner zone, storm-related enhancements are observed throughout the outer zone. Figure 4-28 shows this temporal behavior of the outer zone electrons as observed by both the low-altitude 1963-38C data and the high-altitude Explorer 26 measurements. For $L \geq 4$, there is clear evidence of flux enhancements in each of the Dst storms, followed by a rapid decay to the prestorm level.

The dynamic storm responses of the outer-zone electrons are further complicated by other external effects such as diurnal drift-shell splitting, the changing sectors of the interplanetary magnetic field, and the injections and accelerations related to the magnetospheric substorms. The day-night differences in electron fluxes can best be illustrated (Figure 4-29) by the observation of the geosynchronous orbiter ATS 1 at $L = 6.6$ (Reference 32). The average flux of electrons with $E \geq 1.05$ MeV at local noon, for example, is a factor of 2.8 higher than that at local midnight. Electrons with energy lower than 1 MeV show slightly smaller diurnal variations.

The effect of substorms and the correlation of the outer-zone electrons with the sector structure of the interplanetary magnetic field are discussed in subsection 4.3.3, which also includes a discussion of the diffusion process.

In view of the marked differences in the characteristics of the inner- and outer-zone electrons, the model environment of the trapped-electron radiation in the two zones is presented separately. Generally, these models are constructed by using time-averaged fluxes measured by several satellites over a time period that covers the epochs near both the minimum and maximum of the solar activity cycle.

The well known solar-cycle effect on the trapped electrons has been observed by many experimenters (Reference 35). Figure 4-30 is an example of the direct observation of OGO 1 and OGO 3 with

4 January 1977

similar spectrometers over two epochs. While the data show comparatively enhanced flux levels in 1967 as the solar maximum approaches, the slot between the inner and outer zones tends to shift to lower L values as it is being filled. This effect can be summarized by the data compiled in Figure 4-31, which shows the shifting positions of both the slot and the peak of the outer zone over the solar cycle, starting at the maximum in 1958. In view of this pronounced influence of solar cycle on the electron environment, the modeling of trapped electrons described in the following subsection is further subdivided into solar maximum and solar minimum epochs for each radiation zone.

4.3.2 Electron Environment Models

In the original edition of Section 4, the AE 2 model was given as a summary of the energetic electron radiation environment which has served as a standard reference for many years. As improved instrumentation and new data become available, it is necessary to update the environment models. In the last few years, the continued effort of data compilation at NASA National Space Science Data Center (NSSDC) has produced electron models AE 4, AE 5, and AE 6. It is the purpose of this section to present the latest versions of these models for the inner- and outer-radiation zones. Because of the previously noted differences in the behaviors between the inner- and outer-zone electrons, the modeling of the electron environment has been accordingly separated. Furthermore, the prominent solar-cycle effects are accounted for by grouping the data with respect to the time epochs of solar maximum and solar minimum. The following electron environment models, currently available at NSSDC for making estimates of future fluxes, are described in the following sections:

	<u>Inner Zone</u>	<u>Outer Zone</u>
Solar Minimum	AE 5 (Epoch 1975) (Projected)	AE 4 (Epoch 1964)
Solar Maximum	AE 6 (Epoch 1980) (Projected)	AE 4 (Epoch 1967)

OUTER-ZONE MODELS. Because of the numerous temporal variations associated with the outer-zone electrons, a useful environment model of the outer zone can be presented with time-averaged fluxes. Singley and Vette (Reference 36) constructed time-averaged flux models, AE 4 Solar Max and AE 4 Solar Min, over the energy range

4 January 1977

of 40 KeV to 4.0 MeV and L values from 3.0 to 11.0. They used data from experiments on board the OGO 1, OGO 3, ERS 13, ERS 17, Explorer 6, Explorer 12, Explorer 14, Explorer 18, Explorer 26, Injun 3, and ATS 1 spacecraft covering the time period between August 1959 to February 1968. The divisions of solar maximum and solar minimum are designated by AE 4 (epoch 1967) and AE 4 (epoch 1964), respectively.

The B dependence and the local time dependence of the electron fluxes are treated as independent functions. At each discrete L interval, the flux is given as a function of magnetic field, B, and local time, ϕ , by the function

$$J = K \left(\frac{B}{B_0} \right)^{-m} \cdot \left(\frac{B_c - B}{B_c - B_0} \right)^{m+1/2} \cdot (10)^{C_1 \cos \left[\frac{\pi}{12} (\phi - \phi_1) \right]} \quad B < B_c$$

(4-1)

$$= 0 \quad B > B_c$$

where

J is the omnidirectional integral flux in $\text{cm}^{-2} \text{sec}^{-1}$

B is the local magnetic field in gauss

B_0 is the equatorial magnetic field of the given L value

B_c is the cut-off magnetic field of the given L value

ϕ is the local time in hours

and K, m, C_1 , ϕ_1 are the coefficients determined by least-squares fits to various data sets. It should be noted, however, that most of the data used in the determination of AE 4 were obtained near the equator so that the B dependence at high B has not been as extensively studied as at low B values. However, several recently obtained data sets indicated reasonable agreement with AE 4 at intermediate B values.

Comparisons of the AE 4 model spectra with data at several L values are shown in Figures 4-32 and 4-33. In general, the spectra for the epoch 1967 show higher fluxes of lower energy ($E < 2.5 \text{ MeV}$) electrons than those of the epoch 1964. It is noted, however, that the data base for AE 4 is quite limited for threshold energies higher than 2 MeV. At the end of this subsection, some recent data collected by Azur and ATS 6 are introduced to supplement the AE 4 model.

4 January 1977

The values of the coefficient m for the B/B_0 dependence are shown in Figure 4-34. In determining the values of m , it was noted that the data points at each L interval do not show much scatter, reflecting the uniformity of the dependence of B/B_0 for various energies and time epochs (Reference 36). The B_c values of the model were chosen to be 0.58 gauss for $L = 3.0$ and approximately 0.6 gauss for higher L shells, assuming the minimum mirroring altitude of energetic electrons at 200 kilometers.

One can consider the dependence on local time in Equation 4-1 by defining

$$W = (10)^{C_1} \cos \left[\frac{\pi}{12} (\varphi - \varphi_1) \right] \quad (4-2)$$

which gives

$$\text{Log } W = C_1 \cos \left[\frac{\pi}{12} (\varphi - \varphi_1) \right] \quad (4-3)$$

Figure 4-35 illustrates the observations of the variation of $\log W$ for the electron fluxes above two threshold energies. For L less than 5.0, the local time variations are small compared to the other uncertainty factors of the model. However, for L values greater than 5.0, the amplitudes of the local time fluctuations increase very rapidly with increasing L , peaking between 0900 and 1200 local time, depending upon both energy and L shell. For 40-KeV electrons at $L = 8$, the maximum flux near local noon is more than one order of magnitude higher than the minimum flux near local midnight. This large variation in flux associated with the local time is based upon the solar minimum data. As the epoch approached solar maximum in 1967, this local time variation was found to be substantially reduced. The Explorer 12 data of 1962, Explorer data of 1963, IMP 1 data of 1964, ERS 13 data of 1964, ERS 17 data of 1965, and ATS 1 data of 1967 shown in Figure 4-36 indicate the trend of this change. The AE 4 model, therefore, is composed of two different model dependences for solar minimum and solar maximum, as shown in Figures 4-37 and 4-38, respectively.

With the description of B/B_0 and local time dependence given in the preceding paragraphs, AE 4 now can be presented as time-averaged equatorial omnidirectional flux $J(E, L)$ as a function of threshold energy and L value. Figures 4-39 and 4-40 show the

4 January 1977

AE 4 radial profiles for the solar minimum (1964) and the solar maximum (1967) epochs, respectively. Note that the outer-zone peak is located at a lower L value near solar maximum (1967) than near solar minimum (1964), consistent with the observation of Vernov et al. (Reference 35).

Since the outer zone electrons undergo large variations with time, it is useful to provide statistical information regarding these variations in addition to the average flux values. AE 4 represents these statistical variations by means of a log-normal distribution. In this model, the variations about the average are evaluated using the standard deviation, $\sigma(E, L)$. Quantitatively, one has

$$P(J > J_1) = \frac{1}{J(E, L)} \cdot \frac{1}{2\pi} \int_{\log J_1}^{\infty} \exp\left[-\frac{1}{2} \left(\frac{Z-X}{\sigma}\right)^2\right] dZ \quad (4-4a)$$

where the integration variable is

$$Z = \log [J(>E, B, L, \phi, t)] \quad (4-4b)$$

and

$$X = \log [J_{\text{avg}}(>E, B, L, \phi, t)] - 1.15 \sigma^2(E, L) \quad (4-4c)$$

The curves of Figures 4-41 and 4-42 give the standard deviation of the model as a function of threshold energies and L values, respectively. Below $L = 5$, the standard deviation changes slowly with energy, with the high-energy electrons having slightly higher standard deviation than the low-energy electrons. Above $L = 5$, the standard deviation of low-energy electrons fluctuates greatly, which is consistent with the previous observation of large local-time fluctuations for the electron fluxes at large L values.

Because of the considerable spatial and temporal variation in the outer-zone electron fluxes, the environment model AE 4 is frequently tested against new data. Figure 4-43 shows three panels of data comparing the solar maximum AE 4 (1967) model with the $E > 1.5$ -MeV electron data from the Azur omnidirectional measurements in November-December 1969 for $L = 3.0, 4.0, \text{ and } 5.5$. As expected, the scatter of data points increases with the L values. The mean flux for the B interval between 0.14 and 0.16 gauss is marked by an open triangle in each panel. Note that the Azur fluxes are higher

4 January 1977

than the AE 4 fluxes for $L = 4.0$ and 3.0 , but lower than the model for $L = 5.5$. For B values greater than 0.3 gauss, however, the Azur measurements show a steeper cutoff than the AE 4 model in all L shells. In general, these new data are within the uncertainty limit of the model, which is estimated to be about a factor of two.

Another example of the model comparison with some recent equatorial measurements by the ATS 1 and ATS 6 (Reference 37) satellites is shown in Figure 4-44. The OGO 1, OGO 3, and the ATS 1 (1967) data used in the model construction at $L = 6.6$ are presented as references. For energies below 2 MeV, the model essentially agrees with the 1974 observation. At 4 MeV, the ATS 6 flux is substantially higher than that predicted by the model. A similar comparison has been observed at $L = 4.0$ between the model spectrum and the Azur measurement shown in Figure 4-45, which is derived from the quiet-time spectrum published by Häusler and Sckope (Reference 38). It is apparent that the Azur flux at $E > 4$ MeV is also larger than the model estimate near the center of the outer radiation zone.

Details of the discrepancy between the AE 4 model radial profile and some high-energy measurements by the OV1-19 satellite are shown on Figure 4-46. The preliminary estimates of the OV1-19 data between March 1969 and January 1970, excluding the period of two major Dst storms in May and October, were provided by Vampola (Reference 39). For $E \geq 1$ MeV, the data are within the model uncertainty limit of a factor of two. For $E \geq 4$ MeV, the data are an order of magnitude higher than the model.

Results of these observations, quoted in the preceding paragraphs, suggest that the flux estimates of the AE 4 model for $E > 2.5$ MeV are significantly lower than the new data. Further data analysis is underway and the AE 4 model will be updated accordingly.

INNER-ZONE MODELS. The natural environment of the inner-zone electron radiation was complicated by the artificial injection of the Starfish detonation in July 1962. These fission injections persisted in the inner zone for several years and have been well documented (see Section 6). The population of these artificial electrons has decayed continuously, and after 1970 it became insignificant compared to the natural environment.

Since the data available for modeling were collected during periods up to 1967, the measured fluxes contained substantial contributions from the Starfish electrons. Therefore, the inner-zone models

4 January 1977

for the 1964 and 1967 epochs (Reference 40) included the artificial electron fluxes.

For making estimates of the future radiation environment, two projected inner-zone models, AE 5 (1975) (Reference 41) and AE 6 (Reference 42), have been generated for solar minimum and solar maximum, respectively, using an empirical Starfish model (Reference 43) to subtract the artificial fluxes from the 1964-1967 data. The derivation of these two projected models can be illustrated by the equatorial radial flux profiles in Figures 4-47, 4-48, and 4-49 for threshold energies of 250 KeV, 500 KeV, and 1 MeV, respectively. The model flux of AE 5 (1967) is based upon the data from five satellites: OGO 1, OGO 3, 1963-38C, OV3-3, and Explorer 26. On Figures 4-48 and 4-49, the dotted curves show the effect of the corrections to the OV3-3 data resulting from changes in the estimated detector efficiency that were made after publication. The shaded areas in Figures 4-47 through 4-49 show the contribution of the Starfish electrons to the AE 5 (1967) electron fluxes. The differences between the AE 6 and AE 5 (1975 projected) curves result from the effects of the different phases of the solar cycle.

Estimates of the Starfish components in the flux data were calculated with the decay time and cutoff time determined by Teague and Stassinopoulos (Reference 43). The Starfish flux and decay time model was developed by separating the observed fluxes into naturally occurring fluxes and Starfish electrons. Assuming an exponential decay for the Starfish residual, some quiet-time data from 1964 to 1967 have been analyzed by an iteration process to produce time profiles of flux components and a self-consistent model of decay time. An example of the iteration procedure result is shown on Figure 4-50 for $L = 1.5$ and 1.9 with the OGO 1 and OGO 3 data. From the apparent solar-cycle variation in the reduced-time profiles of the ambient flux components, a solar-cycle parameter, R_T , has been estimated for each threshold energy and L value in the inner zone, using the October 1967 flux level as a standard reference. Figure 4-51 is an example of the parameter R_T , which is defined as the ratio

$$R_T = \frac{J(E, L, T = \text{October 1967})}{J(E, L, T)}$$

where T is the number of months counted from September 1964. For $E > 500$ KeV, the solar-cycle variation is largest at $L = 1.8$ where the variation is substantially larger than at lower or higher

4 January 1977

L values. With these values of R_T and the Starfish decay model, an environment model free from artificial fluxes was constructed for the solar minimum in 1975. In a similar fashion, the solar maximum environment model (projected for 1980) AE 6 was derived from the reference model flux of AE 5 (1967) by subtracting the Starfish component.

Because only the natural radiation environment will be considered in practice, only the Starfish-free models are presented in the following paragraphs. The original model documents should be referred to for data analysis details.

In the graphic presentation of the AE 5 (1975) and AE 6 models, a new form of computer-generated nomograph has been made to provide easy scaling in engineering application. Examples of the flux maps with the B-L coordinates are shown on Figures 4-52 and 4-53. Note that the omnidirectional integral flux is higher in AE 6 than in AE 5 (1975), but the B dependence is essentially the same at most of the L values.

The accuracy of the models depends upon the particle energy and B-L coordinates under consideration. In the inner-zone models, AE 5 and AE 6, the expected model accuracy is represented by confidence codes. These codes have integer values from 1 to 10, corresponding to the model uncertainties from a factor in excess of 10 to a factor of 2, respectively. Tables 4-1 and 4-2 give these confidence codes for AE 5 (1975) and AE 6, respectively.

Since the two inner-zone models presented herein are projected models, the data used for model construction cannot be directly compared with the model curves without modification. However, a display of the data used for modeling and some new observations against the model spectrum will be indicative of the development trend of the inner-zone environment. Figures 4-54 and 4-55 are the examples of the time-averaged data from five satellites at $L = 1.4$ and 1.6 , respectively. The reduced data points of OGO 1, OGO 3, and OV3-3 have been used in deriving the models. The OGO 5 and OV1-13 points are measurements taken in 1968, which is near the solar maximum. The model curves for solar maximum epochs are shown by the solid lines.

As described previously, AE 5 (1967) is the model that includes substantial Starfish electrons and AE 6 is the projection model (1980)

4 January 1977

Table 4-1. Omnidirectional flux confidence codes for AE 5 (1975 projected).
(Values 1 through 10 indicate uncertainties ranging from a factor of >10 to a factor of 2.)

Code	L Range	E Range	Remarks
1	<1.25	≥3 MeV	Extrapolation on B, L, and E
4	≥1.3	≥3 MeV	Extrapolation on E and B
5	1.3-1.6	0.5-3 MeV	Starfish model used to estimate artificial flux Agrees with pre-Starfish data at E ~ 1.6 MeV
5	1.9-2.4	>250 KeV	Storm effects. Corrected for OV3-3 data
6	1.3-1.9	0.7-2.5 MeV	Corrected for OV3-3 data
6	1.9-2.4	40-250 KeV	Solar-cycle parameters used
7	1.6-1.9	40-600 KeV	Solar-cycle parameters used
8	1.3-1.6	40-500 KeV	Solar-cycle parameters used

Table 4-2. Omnidirectional flux confidence codes for AE 6. (Values 1 through 10 indicate uncertainties ranging from a factor of >10 to a factor of 2.)

Code	L Range	E Range	Remarks
1	<1.25	≥3 MeV	Extrapolation on B, L, and E
3	≥1.3	≥3 MeV	Extrapolation on E and B
5	1.3-1.6	0.7-3 MeV	Starfish model used to estimate artificial flux
5	1.9-2.4	>250 KeV	Storm effects. Corrected for OV3-3 data
6	1.6-1.9	0.7-3 MeV	Minor adjustment for Starfish flux
6	1.9-2.4	<250 KeV	Some storm effect
9	1.3-1.9	250-700 KeV	Minor modification with respect to AE 5 (1967)
10	1.3-1.9	<250 KeV	Same as AE 5 (1967)

4 January 1977

after the subtraction of the Starfish component. The difference between these two models, i. e., the Starfish component, is larger at $L = 1.4$ than at $L = 1.6$ because the former is closer to the location of the electron injection in July 1962. The dominant effect of the Starfish electrons is most obvious in the OGO 1 data of 1964, which is near solar minimum. For energies above 0.4 MeV, the flux level of the OGO 1 measurement, which is mainly Starfish flux, is substantially higher than the fluxes observed by other satellites in 1966 and 1968, masking the solar-cycle effect. For energies below 0.4 MeV, however, the OGO 1 result is found to be lower than the observations near solar maximum, showing the trend of solar-cycle variation.

According to the study of Teague and Stassinopoulos (Reference 43), the complication of artificial electron fluxes became insignificant by 1970. An improved inner-zone model of the natural radiation, therefore, can be constructed when data from the years after 1970 are available.

AN OVERALL VIEW OF THE ELECTRON ENVIRONMENT. As described in the two preceding subsections, different data analysis techniques have been employed to develop the outer-zone and inner-zone models. These radiation-zone models have been further subdivided to represent the conditions in the epochs of solar maximum and solar minimum. Quantitative details of the combined results over the two zones have been documented in each of the original publications. It is sufficient, here, to summarize the modeling effort by a sample radial profile. Figure 4-56 shows the overall equatorial omnidirectional flux curves for the $E > 0.5$ MeV electrons. The inner-zone and outer-zone models have been combined here. It is interesting to note that most of the solar-cycle variations in the flux levels are found in the L range between 1.5 and 5.0. The lack of obvious solar-cycle variation outside this L range can be attributed to the effect of the dominant short-term variations, such as substorms, in these regions; the short-term variations have been smoothed out in the time-averaging process of modeling.

Another useful estimate of the radiation environment is the orbit-integrated fluxes (1-day fluences) (see Section 8), which are obtained by accumulating the electron doses by "flying" the orbiter at various altitudes and inclinations in the model environment. Detailed results are available in the original model documents. As an example, Figure 4-57 is a graphical presentation of the fluxes as a function of altitude for the $E > 0.5$ -MeV electrons integrated over circular orbits with inclinations at 30 degrees and 90 degrees. Again, both inner-zone and outer-zone models have been included in the calculation.

4 January 1977

4.3.3 Possible Sources, Losses, and Transport Mechanisms of Trapped Electrons

The electron flux enhancements caused by magnetic storms and the subsequent decay have been shown by the long-term variations (in days) of the 1963-38C data in subsection 4.2.1. The short-term particle enhancements (in hours or minutes) associated with sub-storm injections near local midnight, followed by gradient drifts, have been observed by the ATS 1 spectrometer (Reference 44). For each event shown on Figure 4-58, a cloud of enhanced electron flux observed on ATS 1 was correlated with a magnetic bay in the magnetogram recorded by a ground station near local midnight. The local times of ATS 1 and the ground stations are shown by the diagram insets. The farther east ATS 1 is from local midnight, the longer the delay between the flux maximum and the magnetogram bay minimum observed, consistent with eastward gradient drifts of electrons injected near local midnight. These results have been confirmed by the high-resolution data of the later satellite, ATS 5 (Reference 45).

The observation of gradient drift, for example, demonstrates the success of the adiabatic invariant theory. As seen in earlier subsections, the adiabatic theory has also provided a proper frame of coordinates to obtain a quantitative description of the time-averaged configurations of the geomagnetically trapped electrons. However, in the interaction between the electrons and the external medium or field, the theory of adiabatic invariants is often violated. The breakdown of the adiabatic invariants, discussed in more detail in Section 5, is believed to be associated with observed particle injections and losses. The dynamics of these interaction processes, such as Coulomb scattering in the atmosphere, radial convection caused by the dawn-dusk electric field, and the pitch-angle diffusion induced by the electromagnetic waves, are the main ingredients of the recent diffusion theories.

For L values below 1.25, the atmospheric Coulomb scattering is the dominant loss mechanism. The observed decay-time constants for electrons in the energy range between 0.3 to 5 MeV, as shown on Figure 4-59, are found to be quite consistent with the predictions of the theory of atmospheric collisions (Reference 46; also Section 5). Because of the decreasing density of the atmosphere with increasing altitudes, the observed electron decay for $L > 1.25$ cannot be accounted for by the mechanism of Coulomb collisions. Beyond $L \approx 1.5$, the apparent lifetime of the electrons decreases as L increases.

4 January 1977

Now, it is generally accepted that the apparent lifetime profile for higher L values in the radiation zones is produced by two intimately coupled diffusion processes: an inward radial diffusion process, which transports electrons across the drift shell; and a pitch-angle diffusion process, which changes the mirror points of the particles on a given field line. By lowering the particle mirroring point, the electrons can be lost to the Earth's atmosphere. By transporting particles inward from an external source, presumably from the solar wind or plasma sheet, the electrons are accelerated and replenish the losses caused by pitch-angle diffusion. (See Section 5 for a detailed discussion.) There are nondiffusion processes, such as charge-exchange, which can be important to the trapped radiation losses. To include these topics here is beyond the scope of this section.

The interplanetary magnetic field (IMF) is another physical factor which affects the trapped radiation dynamics. The correlation between the magnetosphere physics and the IMF has been reported by many authors. The trigger of a magnetospheric substorm is observed to depend upon the length of time in which the IMF turns southward (Reference 47). Further observations of substorm-related processes of energization and transport of the particles in the trapped region have been described in detail (Reference 48).

One of the most recent observations of the association between the IMF and the population of trapped electrons is shown in Figure 4-60 (Reference 49). Using the ATS 1 and ATS 6 electrons recorded in the autumn of 1974 and in the spring of 1975, Paulikas and Blake (Reference 49) found a modulation in the flux intensity that is correlated to the IMF sector structure. As shown on both panels of Figure 4-60, the enhanced flux intensities (shaded) occur when the Earth is in a (+) sector of the IMF during northern hemisphere autumn and when the Earth is in a (-) sector of the IMF during the spring months. This observation has been interpreted as evidence of the enhanced interaction between the solar wind and the magnetosphere when the latter is immersed in a southward-pointing IMF, in agreement with other phenomenological studies quoted in the preceding paragraphs.

4.3.4 Recent Observations of Low-Energy ($E < 40$ KeV) Electrons

With the new generation of satellite-borne instruments that possess adequate sensitivities in the energy range from approximately

4 January 1977

1 eV to 40 KeV, an abundant wealth of important knowledge of low-energy electrons has been obtained during the last few years. A comprehensive survey of the recent progress on this topic has been reported by Frank (Reference 50). Of particular interest in the new observation is the striking occurrence of a local peak at about 3 KeV in the otherwise monotonic differential energy spectrum. This pattern of low-energy electron fluxes is usually observed near the trapping boundary of 40-KeV electrons and is called "inverted V" substructure because of its appearance on an energy-time spectrogram. Such an example of the Injun 5 spectrum is shown on Figure 4-61. The solid line that goes through the data points is a model spectrum computed by assuming an initial Maxwellian electron distribution with a 400-volt electric potential difference along a magnetic field line (Reference 51). The consistency between the data and the model computation gives strong evidence that the magnetospheric electric field plays a dominant role in the dynamics of low-energy electrons.

The average morphology of low-energy electrons has been mapped by McDiarmid et al. (Reference 52), using data from about 1,100 passes of the polar-orbiting ISIS 2 satellite. Figure 4-62 is a semi-schematic diagram of the location of peak fluxes and corresponding energies mapped to the equatorial plane. The contours shown by heavy lines are the peak flux contours with energies given in KeV units. The local times of the minima in average energy near the closed-field-line limit are marked. The pattern shown by the lighter lines is the model electric potential (Model E3H) of McIlwain (Reference 53), which is derived from the low-energy particle measurements of the ATS 5 satellite near the equatorial plane. Qualitatively, this composite map suggests that two processes might be involved in the entry of magnetosheath particles into the closed-field-line region: a convection process responsible for the premidnight entry, energization, and subsequent flow through the magnetosphere; and a diffusion-like process responsible for the entry around 1500 and 0300 local mean times (LMT) with appreciably less acceleration than the premidnight admission. As expected, this reported behavior of low-energy electrons using average fluxes might have included the penetration of the structured cleft-electrons from the magnetosheath observed by Heikila and Winningham (Reference 54).

The importance of low-energy ($E < 40$ KeV) electrons in the radiation environment has been specifically emphasized by Rosen (Reference 55) in a study of the problems of spacecraft charging and high-voltage arcing. For a synchronous satellite, in particular, the space

4 January 1977

vehicle was observed to charge to potentials as high as 10 KV (Reference 56) by the bombardment of the 3- to 20-KeV electrons injected during a substorm. The implication of this potential environmental hazard in the Earth's vicinity has become increasingly important for future designs. More study is required to produce the needed environment model of the $E < 40$ -KeV electrons. Further details of this subject are beyond the scope of the present section.

4.4 MAGNETOSPHERICALLY TRAPPED IONS WITH $Z \geq 2$

4.4.1 Energetic Ions—Alpha Particles with $E > 100$ KeV

The presence of trapped ions heavier than protons in the radiation belts has been well established by several experimenters. For a recent review, see the article by West (Reference 10). The most extensive observations have centered on alpha particles (References 57 through 60), although the medium nuclei (CNO group) also have been observed (References 60 through 63). The motivation for these efforts results from the insight to be gained concerning the trapped radiation dynamics (References 64 through 66).

Alpha particles have been observed from $L = 1.6$ to greater than 5, with energies between 0.85 and 9.0 MeV. The presence of still higher energy alphas within the inner zone is implied by the hard spectra shown on Figure 4-63 (Reference 67). Differential energy spectra are given for L values between 1.525 and 2.125, with $B/B_0 = 1.3$. In the outer zone, the spectra are much softer in the same energy range shown in Figure 4-64 for $B = 0.1$ gauss (Reference 57).

The nature of the alpha particle population appears to change rather abruptly near $L = 2$, as shown by the B - L plots of Figure 4-65. This figure shows count rate contours for three energy intervals between 2.15 and 9.0 MeV in the inner zone and several corresponding count rate contours for four energy intervals between 0.85 and 5.55 MeV in the outer zone. A sharp bend in the contours near $L = 2$ is apparent. To convert from counts-per-second to flux (α -particles/cm²-sec-ster) in a given energy interval, multiply by: 470 for the 0.85- to 1.5-MeV channel; 380 for the 1.50- to 2.15-MeV channel; 425 for the 2.15- to 3.55-MeV channel; 375 for the 3.55- to 5.55-MeV channel; and 342 for the 5.55- to 9.0-MeV channel (References 57 and 67). A final alpha particle B - L plot of flux (α -particles/cm²-sec-ster) contours is shown on Figure 4-66 for energies between 1.18 and 8.0 MeV in the outer zone (Reference 60).

4 January 1977

These contours differ somewhat from those shown on Figure 4-65, particularly for L values above 4.0. This difference is not completely understood at the present time, but is presumably related to a time variation.

Observations in the outer zone near the geomagnetic equator have been sparse. The Explorer 45 (S³) satellite made the first observations in this region. The radial profile count rate observed for alpha particles between 0.91 and 2.0 MeV is shown on Figure 4-67. This profile is similar to that observed for protons in the same energy per nucleon range, and the ratio of the alpha-to-proton fluxes is found to be approximately 1×10^{-2} (Reference 59).

This ratio is an order of magnitude or more larger than that observed for alpha particles mirroring at large distances from the geomagnetic equator. Typical values at low altitudes are approximately 10^{-4} for energies above 0.5 MeV per nucleon and approximately 10^{-3} for energies above 0.25 MeV per nucleon. The L dependence of this ratio at these altitudes is shown on Figure 4-68 for energy intervals between 0.212 and 2.5 MeV per nucleon (Reference 58). There is some peaking of the ratio at low L values and low energy per nucleon, which is related to the peaking in the proton energy spectrum near 300 KeV.

The alpha-particle flux has been seen to undergo considerable time variations, especially during some storms. Figure 4-69 (Reference 60) covers the time period from September 1968 to May 1970 at L = 3.05 and B = 0.19 gauss. Daily averages of the proton (0.31 to 45 MeV) and alpha-particle (1.18 to 8.0 MeV) fluxes, as well as the ratio J_{α}/J_p , are plotted together with the indices Dst and ΣKp . The triangles indicate the times of sudden commencements. Note the large response to the storm on day 305, 1968, in which the alpha fluxes increased about a factor of 100 while the proton fluxes increased about a factor of 10. Both subsequently decayed with time constants near 40 days. However, a larger storm on day 83, 1969, had no apparent effect on these fluxes.

Alpha-particle distribution functions are seen to increase with increasing L value through L = 4, which indicates the source lies beyond this L value (References 58 and 60). Possible source mechanisms include the polar wind, solar wind, and direct capture of solar-flare particles. Observations supporting the direct capture mechanism have been reported (Reference 68). Other observations and theories indicate that this mechanism might be limited to special circumstances and, thus, favor either the solar or polar wind (Reference 60).

4 January 1977

4.4.2 CNO Nuclei with $E > 100$ KeV

The observation of the medium (CNO) nuclei and, particularly, the determination of the O/C ratio, might make it possible to identify the major source of magnetospheric particles. Trapped $Z \geq 3$ nuclei (most probably CNO nuclei) at approximately 0.3 MeV per nucleon have been reported (Reference 69). The CNO to He flux ratio is $2.8 \pm 0.5 \times 10^{-3}$ with L in the 3 to 3.5 range and B in the range of 0.15 to 0.20 gauss. The separate identification of the carbon and oxygen fluxes in the 3 to 5 L range for energies between 13 and 33 MeV per nucleon also has been reported (Reference 61). The average CNO flux is $9.3 \pm 3.2 \times 10^{-4}$ particles/cm²-sec-ster-MeV-nucleon⁻¹, or about 100 times the interplanetary CNO flux. The abundance ratio is obtained as $O/C = 0.5 \pm 0.4$. This ratio indicates an extraterrestrial source for the magnetospheric particles, such as the solar wind. However, this might not be a definitive test because of the high energies involved (Reference 64).

4.4.3 Heavy Ions with $E < 100$ KeV

The composition of the magnetospheric ions in the important range from a few KeV to a few tens of KeV, which contains the bulk of the plasma energy, is still an open question. Most measurements in this range were obtained with instruments incapable of identifying the species of the ions being detected, and they were commonly referred to as "protons" by assumption only. Recent observations raise doubts as to the general validity of this assumption. Measurements of ions with energies up to 12 KeV, using satellite-borne mass spectrometers, have shown that O^+ is an important and sometimes dominant component of the precipitating population during magnetic storms (References 70 through 73). At times, He^+ has been observed to be prominent in the precipitating species (Reference 74). Equatorial observations of the evolution of the pitch-angle distributions of ring-current ions during a storm recovery phase by Explorer 45 were interpreted as implying that the ring current ions at $L \leq 4$ and energy ≤ 50 KeV are not primarily protons. He^+ was suggested as an alternative candidate (References 75 and 76), but this interpretation was questioned (Reference 77) and the matter is still under discussion (Reference 78).

A recently orbited mass spectrometer experiment on a spinning satellite measured large fluxes [$\approx 10^8$ (cm²-sec-ster-KeV)⁻¹] of O^+ and H^+ ions being accelerated upward, out of the ionosphere, at altitudes between 5,000 and 8,000 kilometers, in the auroral and

4 January 1977

polar regions. These fluxes were interpreted as direct products of an ionospheric acceleration mechanism (Reference 79), underscoring the importance of the ionosphere as a source of magnetospheric ions. Despite these measurements, the lack of mass spectrometer observations at high altitudes in the equatorial plane still leaves open the question of the composition of the trapped energetic ions which constitute the ring current. Hopefully, planned measurements on GEOS, ISEE (the International Sun-Earth Explorer), and EE (Electrodynamics Explorer) will resolve this important issue.

4.5 SUMMARY

This section presents a brief review of the trapped radiation environment in the Earth's vicinity. Models of the proton and electron environments in epochs of solar maximum and solar minimum are described. Results of some updated data analysis are used to supplement the electron models.

For both energetic protons ($E > 100$ KeV) and electrons ($E > 40$ KeV), the particle populations have been shown to exhibit a much more dynamic behavior in the outer zone than in the inner zone. For particles of lower energies, the data are relatively new and no extensive empirical model environment has been developed. Although the heavier ion ($Z \geq 2$) fluxes with $E > 100$ KeV have been found to be two and more orders of magnitude below the proton fluxes, their observation should provide a better understanding of the trapped radiation dynamics.

Much work is still needed to establish the major source and loss processes, and to include the significant temporal variations in the empirical models.

4 January 1977

REFERENCES

1. Roederer, J.G., Dynamics of Geomagnetically Trapped Radiation, Spring-Verlag Co., New York, 1970.
2. Schulz, M., and L.J. Lanzerotti, Particle Diffusion in the Radiation Belts, Spring-Verlag Co., New York, 1974.
3. Hess, W.N., The Radiation Belt and Magnetosphere, Blaisdell Publishing Co., Waltham, Massachusetts, 1968.
4. Hess, W.N., and G.D. Mead, Introduction to Space Science, Second Edition, Gordon and Breach, Science Publishers, New York, 1968.
5. McCormac, B.M., "Radiation Trapped in the Earth's Magnetic Field," Proceedings of the Advanced Study Institute, Bergen Norway, 16 August to 3 September 1965, D. Reidel Publishing Co., Dordrecht, Holland, 1966.
6. McCormac, B.M., "Earth's Particles and Fields," Proceedings of the NATO Advance Study Institute, Freising, Germany, 13 July to 11 August 1967, Reinhold Book Corp., New York, 1968.
7. Williams, D.J., and G.D. Mead, "Proceedings of the International Symposium on the Physics of the Magnetosphere," Washington, D.C., 3 to 13 September 1968, Rev. Geophys., 7, 1-459, 1969.
8. Williams, D.J., "Sources, Losses, and Transport of Magnetically Trapped Particles," in Solar Terrestrial Physics/1970: Part II, E.R. Dyer, ed., p. 66, D. Reidel Publishing Co., Dordrecht, Holland, 1972.
9. Egeland, A., O. Holter, and A. Omholt, Cosmical Geophysics, University Press, Oslo, Norway, 1973.
10. Bell, P.M., Reviews of Geophysics and Space Physics, 13, Special Issue, 925-1048, 1975.

4 January 1977

11. Stevens, J. R., E. F. Martina, and R. S. White, "Proton Energy Distributions from 0.6 to 3.3 MeV at 6.6 Earth," J. Geophys. Res., 75, 5373, 1970.
12. Sawyer, D. M., and J. I. Vette, Trapped Proton Environment for Solar Maximum and Solar Minimum (to be published by NSSDC, 1976).
13. Farley, T. A., and N. Walt, "Source and Loss Processes of the Inner Radiation Belt," J. Geophys. Res., 76, 8223, 1971.
14. Croley, D. R., Jr., M. Schulz, and J. B. Blake, "Radial Diffusion of Inner-Zone Protons: Observations and Variational Analysis," J. Geophys. Res., 81, 585, 1976.
15. Claflin, E. S., and R. S. White, "The Source of Inner Belt Protons," J. Geophys. Res., 78, 4675, 1973.
16. Claflin, E. S., and R. S. White, "A Study of Equatorial Inner Belt Protons from 2 to 200 MeV," J. Geophys. Res., 79, 959, 1974.
17. Blanchard, R. C., and W. N. Hess, "Solar Cycle Changes in Inner-Zone Protons," J. Geophys. Res., 69, 3927, 1964.
18. Nakano, G. H., and H. H. Heckman, "Evidence for Solar-Cycle Changes in the Inner-Belt Protons," Phys. Rev. Lett., 20, 806, 1968.
19. Imhof, W. L., C. O. Bostrom, P. S. Beall, J. C. Armstrong, H. H. Heckman, P. J. Lindstrom, G. H. Nakano, G. A. Paulikas, and J. B. Blake, Models of the Trapped Radiation Environment, Voll III: Long Term Time Variations, NASA SP-3024, 1971.
20. Sörass, F., and L. R. Davis, Temporal Variations of the 100 KeV to 1700 KeV Trapped Protons Observed on Satellite Explorer 26 During the First Half of 1965, NASA-GSFC-X-612-68-328, Goddard Space Flight Center, Greenbelt, Maryland, 1968.
21. Moritz, J., private communication.
22. Davis, L. R., and J. M. Williamson, "Outer Zone Protons," Radiation Trapped in the Earth's Magnetic Field, B. M. McCormac, Ed., D. Reidel Publishing Co., Dordrecht, Holland, 1966.
23. Lanzerotti, L. J., "Access of Solar Protons to Synchronous Altitudes," in Intercorrelated Satellite Observations Related to Solar Events, V. Manno and D. E. Page, eds., D. Reidel Publishing Co., Dordrecht, Holland, 1970.

4 January 1977

24. Frank, L. A., "On the Extraterrestrial Ring Current During Geomagnetic Storms," J. Geophys. Res., 72, 3753, 1967.
25. Smith, P. H., and R. A. Hoffman, "Ring Current Particle Distributions During the Magnetic Storms of December 16-18, 1971," J. Geophys. Res., 78, 4731, 1973.
26. Axford, W. I., "Magnetospheric Convection," Rev. Geophys. Space Phy., 7, 421, 1969.
27. Vasyliunas, V. M., "The Interrelationship of Magnetospheric Processes," Earth's Magnetospheric Processes, B. M. McCormac, ed., p 29-38, D. Reidel Publishing Co., Dordrecht, Holland, 1972.
28. Pizzella, G., and L. A. Frank, "Energy Spectrums for Proton ($200 \text{ eV} \leq E \leq 1 \text{ MeV}$) Intensities in the Outer Radiation Zone," J. Geophys. Res., 76, 88, 1971.
29. Lyons, L. R., and D. J. Williams, "Storm-Associated Variations of Equatorially Mirroring Ring Current Protons, 1-800 KeV, at Constant First Adiabatic Invariant," J. Geophys. Res., 81, 216, 1976.
30. Williams, P. J., and L. R. Lyons, "The Proton Ring Current and Its Interaction With the Plasmapause: Storm Recovery Phase," J. Geophys. Res., 79, 4195, 1974.
31. Vette, J. I., A. B. Lucero, and J. A. Wright, Models of the Trapped Radiation Environment, Vol. II: Inner and Outer Zone Electrons, NASA SP-3024, 1966.
32. Paulikas, G. A., and J. B. Blake, "The Particle Environment at the Synchronous Altitude," in Models of the Trapped Radiation Environment, Vol. VII: Long Term Time Variations, NASA SP-3024, 1971.
33. Bostrom, C. O., D. S. Beall, and J. C. Armstrong, "Time History of the Inner Radiation Zone," in Models of the Trapped Radiation Environment, Vol. VII: Long Term Time Variations, NASA SP-3024, 1971.
34. Williams, D. J., J. F. Arens, and L. J. Lanzerotti, "Observations of Trapped Electrons at Low and High Altitudes," J. Geophys. Res., 73, 5673, 1968.
35. Vernov, S. N., E. V. Gortchakov, S. N. Kuznetsov, Yu. I. Logatchev, E. N. Sosnovets, and V. G. Stolpousky, "Particle Fluxes in the Outer Geomagnetic Field," Rev. of Geophys., 7, 257, 1969.

4 January 1977

36. Singley, G.W., and J.I. Vette, The AE-4 Model of the Outer Radiation Zone Electron Environment, NSSDC 72-06, 1972.
37. Paulikas, G.A., private communication.
38. Häusler, B., and N. Sckope, "The Behaviour of Outer Radiation Belt Electrons (>1.5 MeV) During a Geomagnetically Disturbed Time on 8 March 1970 and its Relationship to Magnetospheric Processes," Planet. Space Sci., 22, 1249, 1974.
39. Vampola, A.L., private communication.
40. Teague, M.J., and J.I. Vette, The Inner Zone Electron Model AE-5, NSSDC 72-10, 1972.
41. Teague, M.J., and J.I. Vette, A Model of the Trapped Electron Population for Solar Minimum, NSSDC 74-03, 1974.
42. Teague, M.J., K.W. Chan, and J.I. Vette, AE 6: A Model Environment of Trapped Electrons for Solar Maximum, NSSDC 76-04, 1976.
43. Teague, M.J., and E.G. Stassinopoulos, A Model of the Starfish Flux in the Inner Radiation Zone, Goddard Space Flight Center Publication X-601-72-487, 1972.
44. Arnoldy, R.L., and K.W. Chan, "Particle Substorms Observed at the Geostationary Orbit," J. Geophys. Res., 74, 5019, 1969.
45. Bogott, F.H., and F.S. Mozer, "Drifting Energetic Particle Bunches Observed on ATS 5," J. Geophys. Res., 79, 1825, 1974.
46. Walt, M., "Loss Rates of Trapped Electrons by Atmospheric Collisions," in Radiation Trapped in the Earth's Magnetic Field, B.M. McCormac, ed., p. 337, D. Reidel Publishing Co., 1966.
47. Arnoldy, R.L. "Signature in the Interplanetary Medium for Substorms," J. Geophys. Res., 76, 5189, 1971.
48. McPherron, R.L., C.T. Russell, and M.P. Aubry, "Phenomenological Models for Substorms," J. Geophys. Res., 78, 3131, 1973.
49. Paulikas, G.A., and J.B. Blake, "Modulation of Trapped Energetic Electrons at $6.6 R_E$ by the Direction of the Interplanetary Magnetic Field," Geophys. Res. Letters, 3, 277, 1976.
50. Frank, L.A., "Magnetospheric and Auroral Plasmas: A Short Survey of Progress," Rev. of Geophys. and Space Phys., 13, 974, 1975.

4 January 1977

51. Evans, D.S., "Precipitating Electron Fluxes Formed by a Magnetic Field Aligned Potential Difference," J. Geophys. Res., 79, 2853, 1974.
52. McDiarmid, I.B., J.R. Burrows, and E.E. Budzinski, "Average Characteristics of Magnetospheric Electrons (150 eV to 200 KeV) at 1400 km," J. Geophys. Res., 80, 73, 1975.
53. McIlwain, C.E., "Substorm Injection Boundaries," in Magnetospheric Physics, B.M. McCormac, ed., p. 143, D. Reidel Publishing Co., Dordrecht, Holland, 1974.
54. Heikkila, W.J., and J.D. Winningham, "Penetration of Magnetosheath Plasma to Low Altitude through the Dayside Magnetospheric Cusps," J. Geophys. Res., 76, 883, 1971.
55. Rosen, A., "Large Discharges and Arcs on Spacecraft," Aeronautics and Aeronautics, 13, No. 6, p. 36, 1975.
56. DeForest, S.E., "Spacecraft Charging at Synchronous Orbit," J. Geophys. Res., 77, 651, 1972.
57. Blake, J.B., and G.A. Paulikas, "Geomagnetically Trapped Alpha Particles: 1, Off-Equator Particles in the Outer Zone," J. Geophys. Res., 77, 3431, 1972.
58. Fennell, J.F., J.B. Blake, and G.A. Paulikas, "Geomagnetically Trapped Alpha Particles: 3, Low-Altitude Outer Zone Alpha-Proton Comparisons," J. Geophys. Res., 79, 521, 1974.
59. Fritz, T.A., and D.J. Williams, "Initial Observations of Geomagnetically Trapped Alpha Particles at the Equator," J. Geophys. Res., 78, 4719, 1973.
60. Krimigis, S.M., and P. Verzariu, "Measurements of Geomagnetically Trapped Alpha Particles, 1968-1970: 1, Quiet-Time Distributions," J. Geophys. Res., 78, 7275, 1973.
61. Mogro-Compero, J.A., "Geomagnetically Trapped Carbon, Nitrogen, and Oxygen Nuclei," J. Geophys. Res., 77, 2799, 1972.
62. Randall, B.A., "Time Variations of Magnetospheric Intensities of Outer Zone Protons, Alpha Particles and Ions ($Z \geq 2$)," University of Iowa Report, 73:3, 1973.
63. Verzariu, P., "Observations of Storm-Associated Low-Energy Protons, Alpha Particles, and $Z \geq 3$ Nuclei within the Magnetosphere on March 8, 1970," J. Geophys. Res., 78, 8367, 1973.

4 January 1977

64. Blake, J.B., "Experimental Test to Determine the Origin of Geomagnetically Trapped Radiation," J. Geophys. Res., 78, 5827, 1973.
65. Cornwall, J.M., "Radial Diffusion of Ionized Helium and Protons: A Probe for Magnetospheric Dynamics," J. Geophys. Res., 77, 1756, 1972.
66. Krimigis, S.M., "The Charge Composition Aspect of Energetic Trapped Particles," in Proceedings of the Solar Terrestrial Relations Conference, p. 207, University of Calgary, Calgary, Alberta, Canada, 1973.
67. Blake, J.B., J.E. Fennell, M. Schulz, and G.A. Paulikas, "Geomagnetically Trapped Alpha Particles: 2, The Inner Zone," J. Geophys. Res., 78, 5498, 1973.
68. Van Allen, J.A., and B.A. Randall, "Evidence for Direct Durable Capture of 1- to 8-MeV Solar Alpha Particles onto Geomagnetically Trapped Orbits," J. Geophys. Res., 76, 1971.
69. Van Allen, J.A., B.A. Randall, and S.M. Krimigis, "Energetic Carbon, Nitrogen, and Oxygen Nuclei in the Earth's Outer Radiation Zone," J. Geophys. Res., 75, 6085, 1970.
70. Shelley, E.G., R.G. Johnson, and R.D. Sharp, "Satellite Observations of Energetic Heavy Ions During a Geomagnetic Storm," J. Geophys. Res., 77, 6104, 1972.
71. Shelley, E.G., R.G. Johnson, and R.D. Sharp, "Morphology of Energetic O^+ in the Magnetosphere," in Magnetospheric Physics, B.M. McCormac, ed., pp 135-139, Reidel Publishing Co., Dordrecht, Holland, 1974.
72. Sharp, R.D., R.G. Johnson, and E.G. Shelley, "The Morphology of Energetic O^+ Ions During Two Magnetic Storms: Temporal Variations," J. Geophys. Res., 81, 3283, 1976.
73. Sharp, R.D., R.G. Johnson, and E.G. Shelley, "The Morphology of Energetic O^+ Ions During Two Magnetic Storms: Latitudinal Variations," J. Geophys. Res., 81, 3292, 1976.
74. Johnson, R.G., R.D. Sharp, and E.G. Shelley, "The Discovery of Energetic He^+ Ions in the Magnetosphere," J. Geophys. Res., 79, 3135, 1974.
75. Lyons, L.R., and D.S. Evans, "The Inconsistency Between Proton Charge Exchange and the Observed Ring Current Decay," J. Geophys. Res. (in press), 1976.

4 January 1977

76. Tinsley, B.A., "Evidence that the Recovery Phase Ring Current Consists of Helium Ions," J. Geophys. Res. (in press), 1976.
77. Sharp, R.D., E.G. Shelley, and R.G. Johnson, "A Search for Helium Ions in the Recovery Phase of a Magnetic Storm," submitted to J. Geophys. Res., 1976.
78. Lyons, L.R., "An Alternative Analysis of Low and High Altitude Observations of Ring Current Ions During a Storm Recovery Phase," submitted to J. Geophys. Res., 1976.
79. Shelley, E.G., R.D. Sharp, and R.G. Johnson, "Satellite Observations of an Ionospheric Acceleration Mechanism," to be published in the November issue of Geophys. Res. Letters, 1976.
80. Schofield, N.S., M.J. Teague, and J.I. Vette, A Study of Inner Zone Electron Data and Their Comparison with Trapped Radiation Models, (to be published by NSSDC) 1976.

4 January 1977

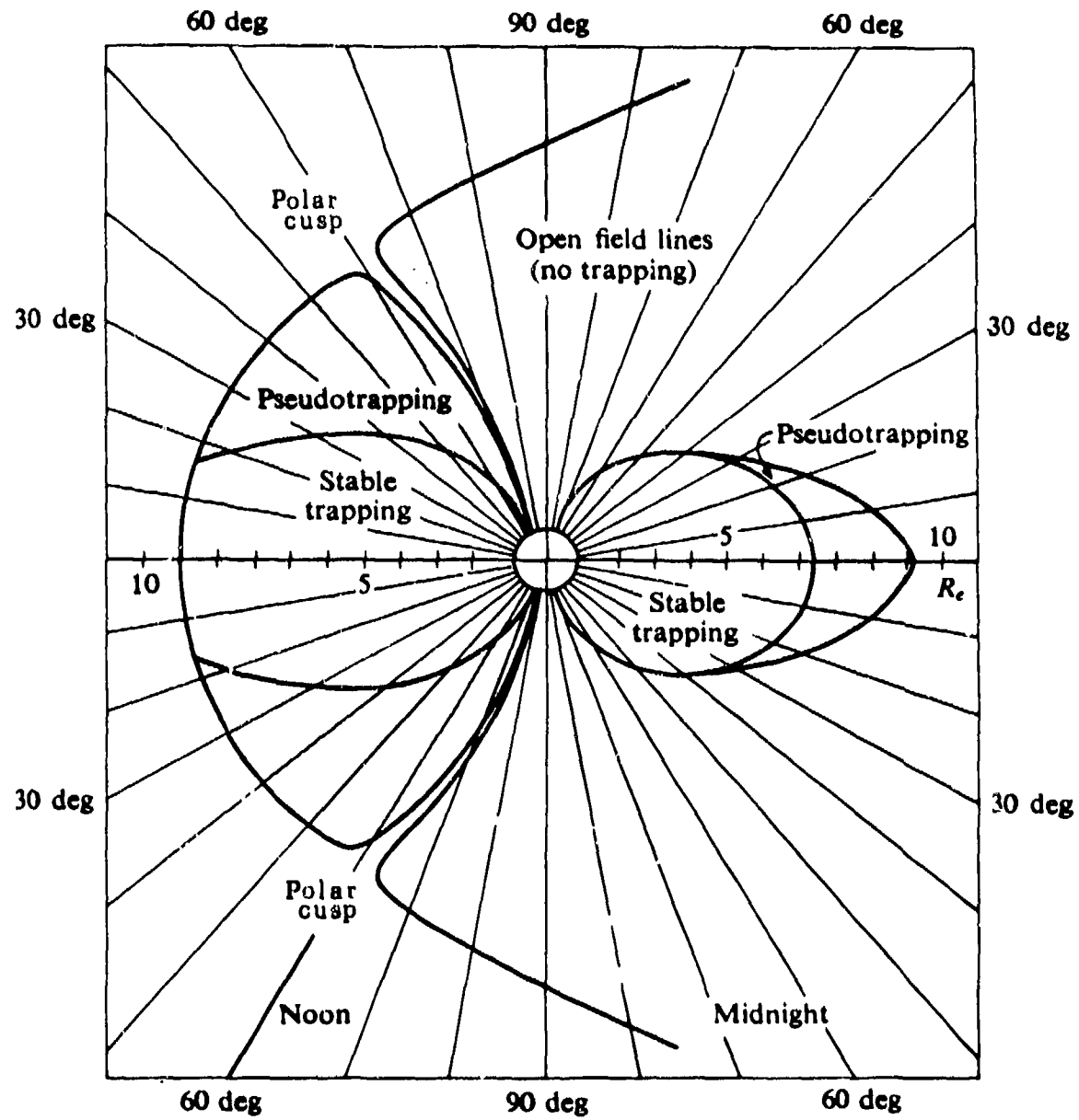


Figure 4-1. Trapping regions for a model magnetosphere.

4 January 1977

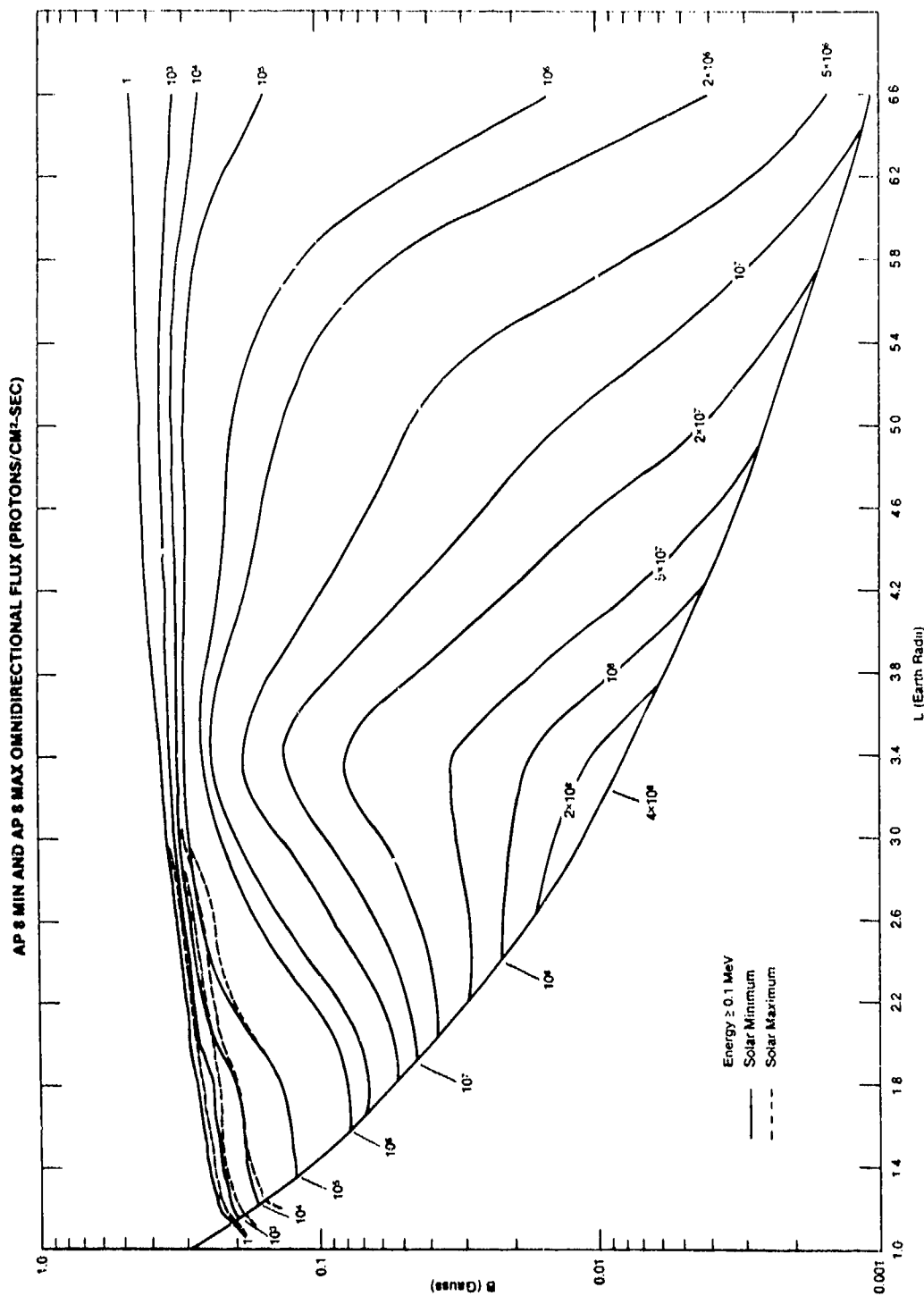


Figure 4-2. B-L omnidirectional flux map for protons with $E \geq 0.1$ MeV at times of solar minimum and solar maximum—models AP8MIN and AP8MAX (Reference 12).

4 January 1977

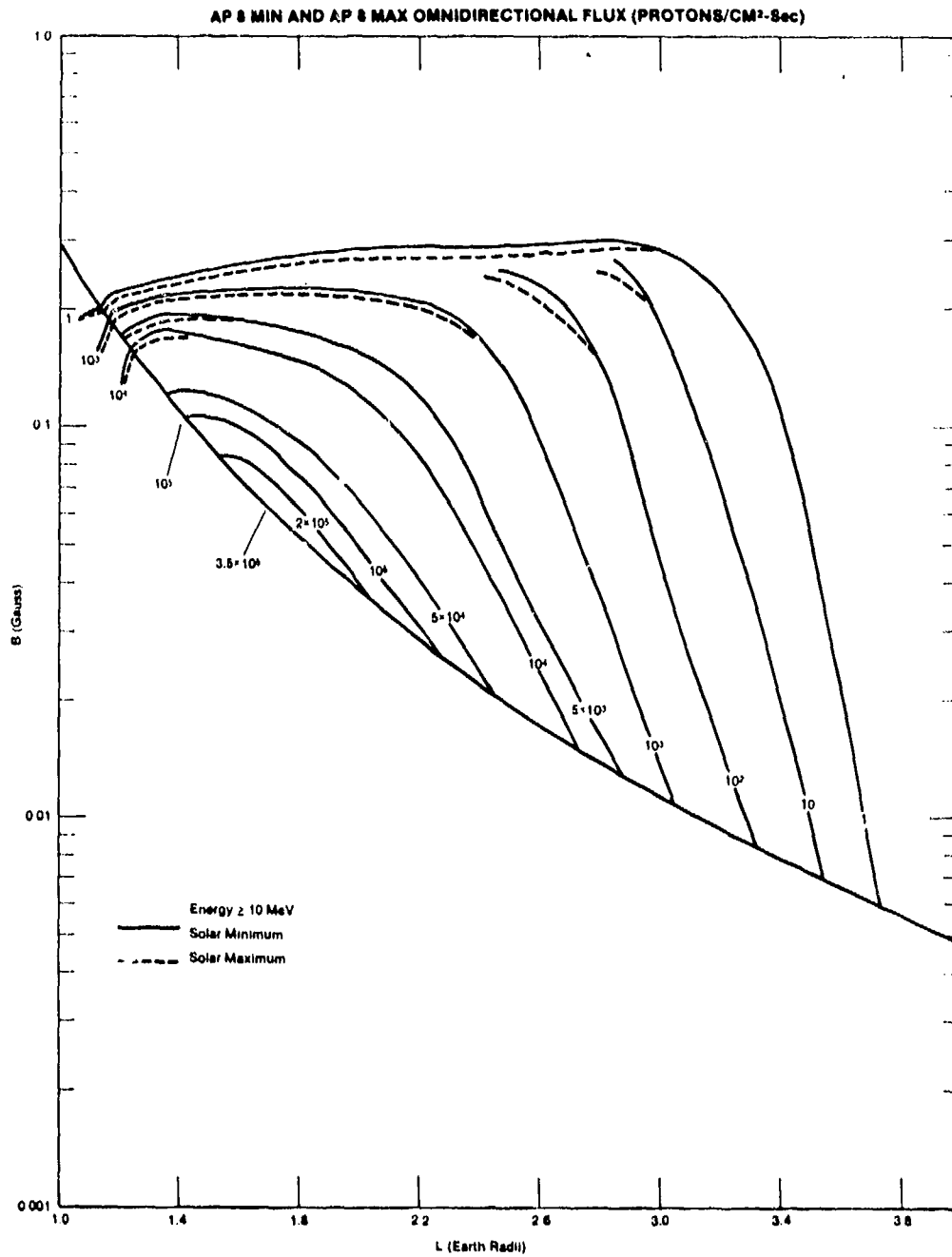


Figure 4-4. B-L omnidirectional flux map for protons with $E \geq 10.0$ MeV at times of solar minimum and solar maximum—models AP8MIN and AP8MAX (Reference 12).

4 January 1977

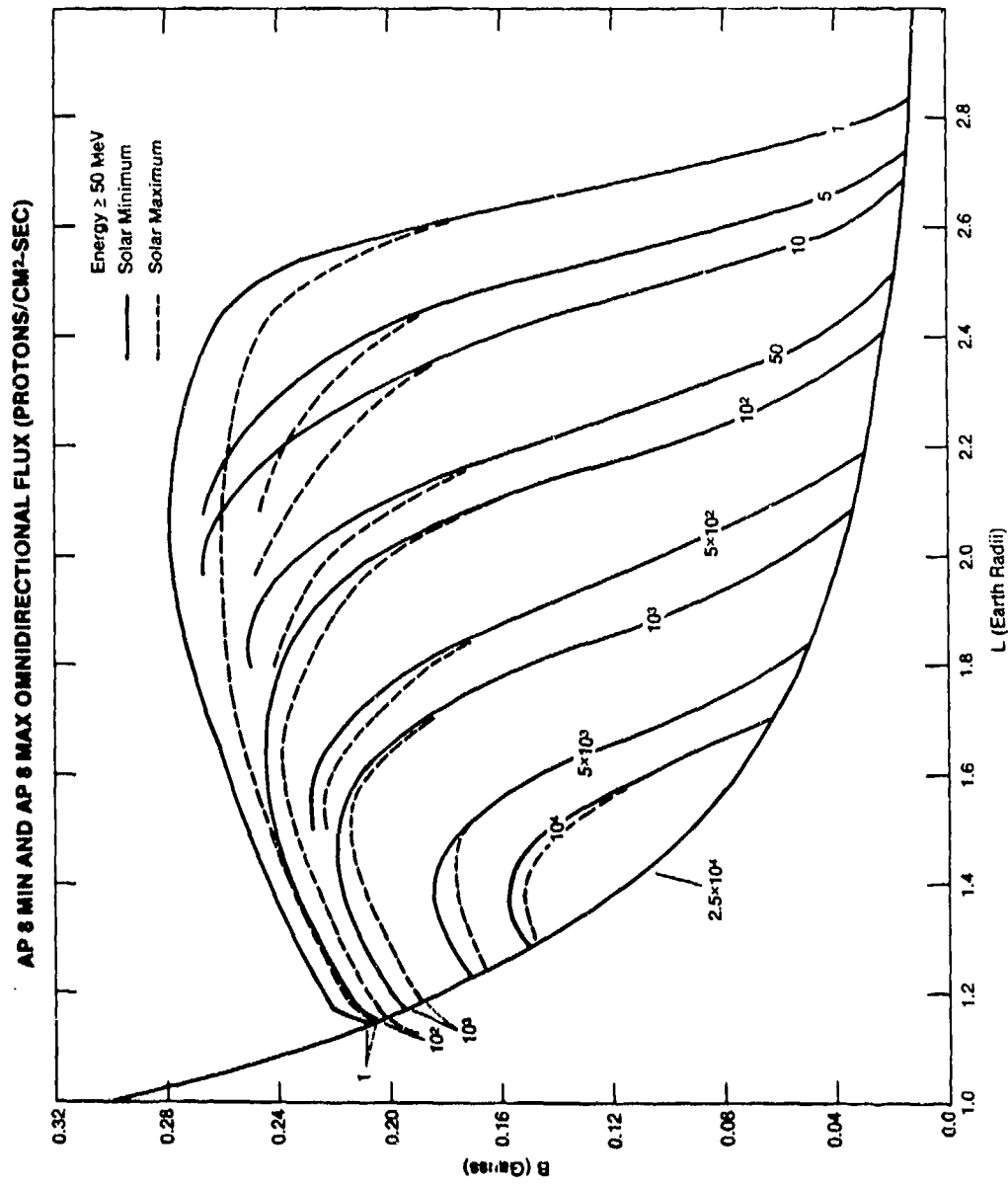


Figure 4-5. B-L omnidirectional flux map for protons with $E \geq 50.0$ MeV at times of solar minimum and solar maximum—models AP8MIN and AP8MAX (Reference 12).

4 January 1977

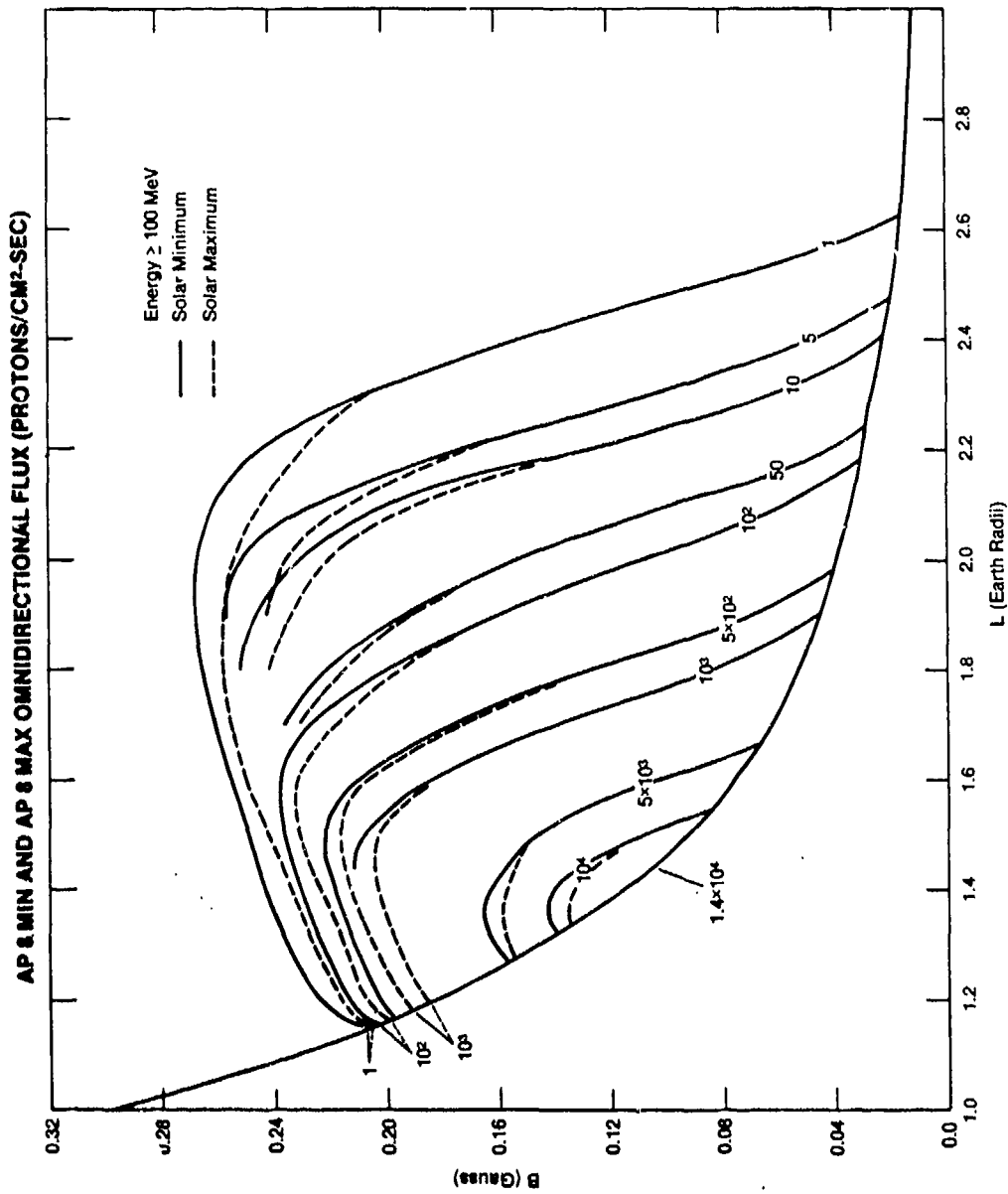


Figure 4-6. B-L omnidirectional flux map for protons with $E \geq 100.0$ MeV at times of solar minimum and solar maximum—models AP8MIN and AP8MAX (Reference 12).

4 January 1977

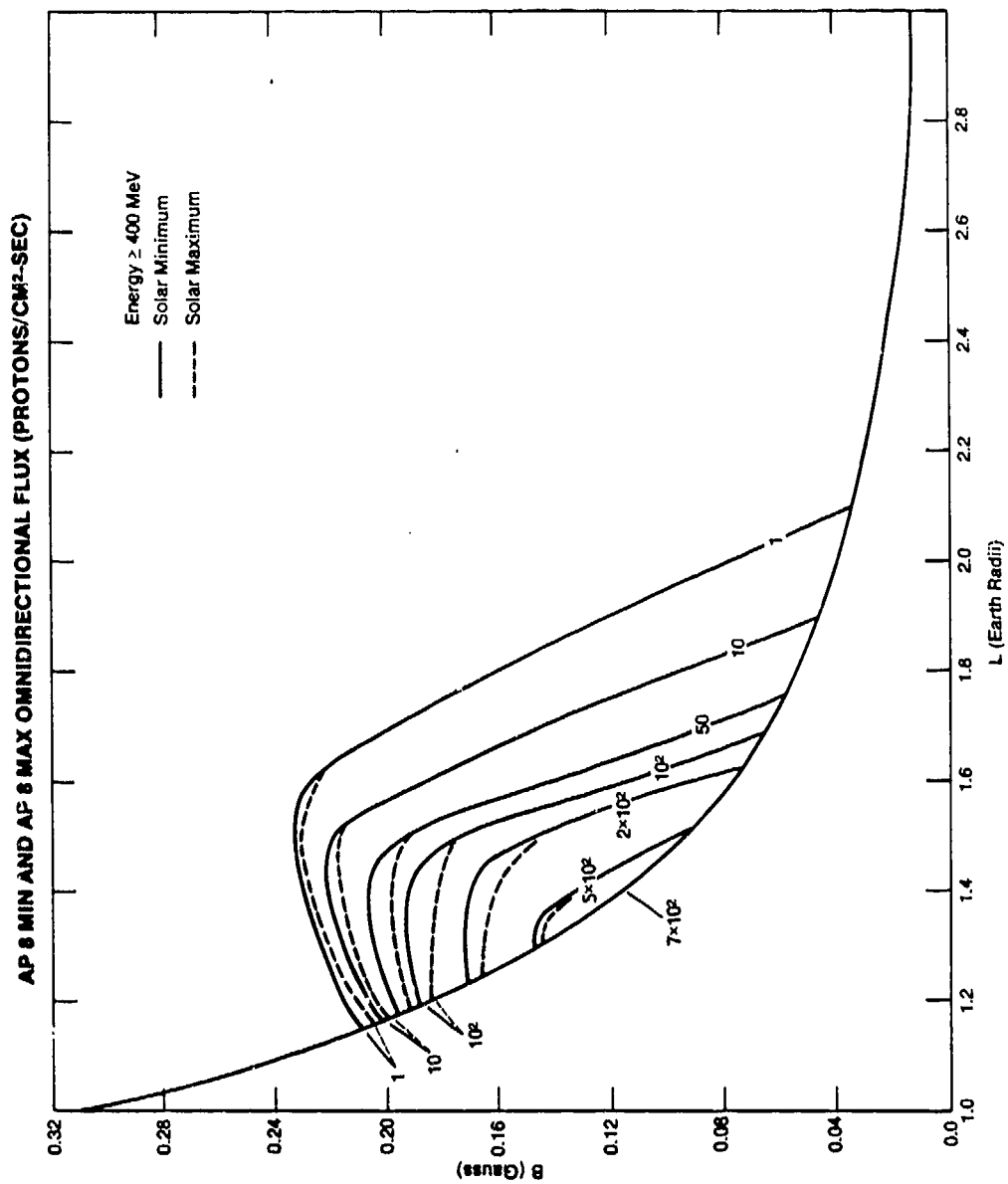


Figure 4-7. B-L omnidirectional flux map for protons with $E \geq 400.0$ MeV at times of solar minimum and solar maximum—models AP8MIN and AP8MAX (Reference 12).

4 January 1977

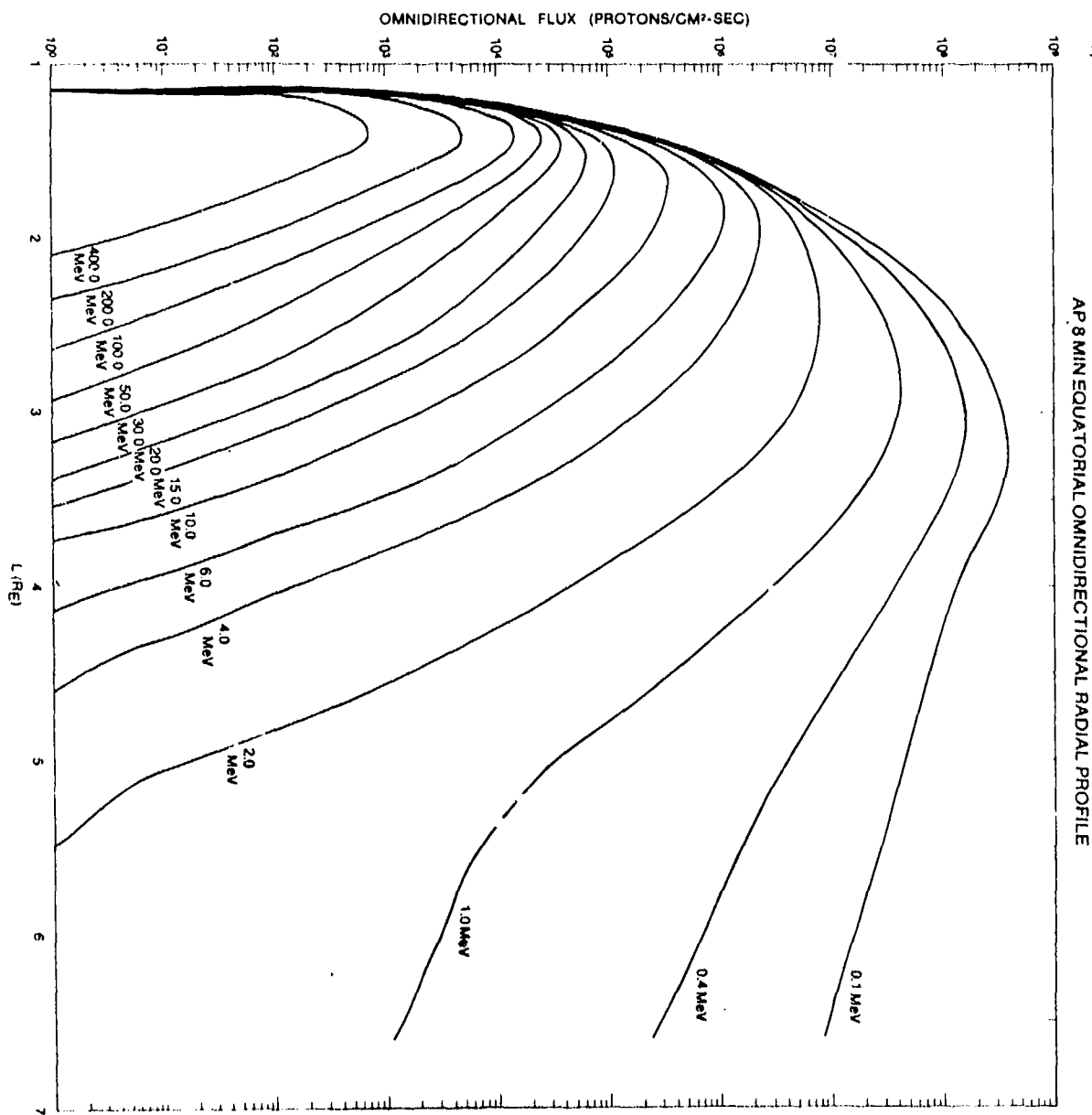


Figure 4-8. Radial distributions of AP8MIN omnidirectional fluxes of protons in the equatorial plane with energies above threshold values between 0.1 and 400.0 MeV (Reference 12).

4 January 1977

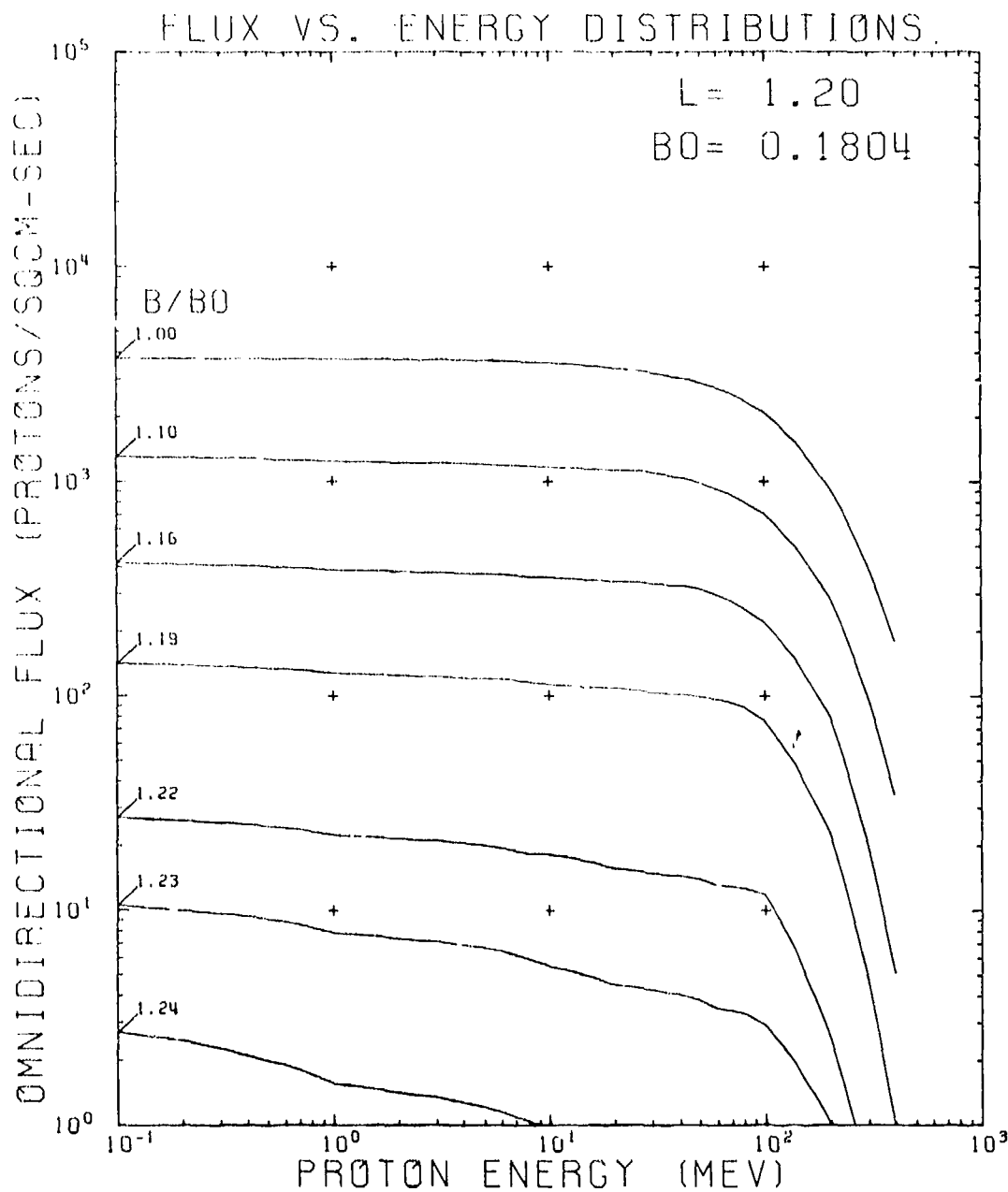


Figure 4-9. Integral spectra of AP8MIN omnidirectional fluxes of protons for various values of B at L = 1.2 (Reference 12).

4 January 1977

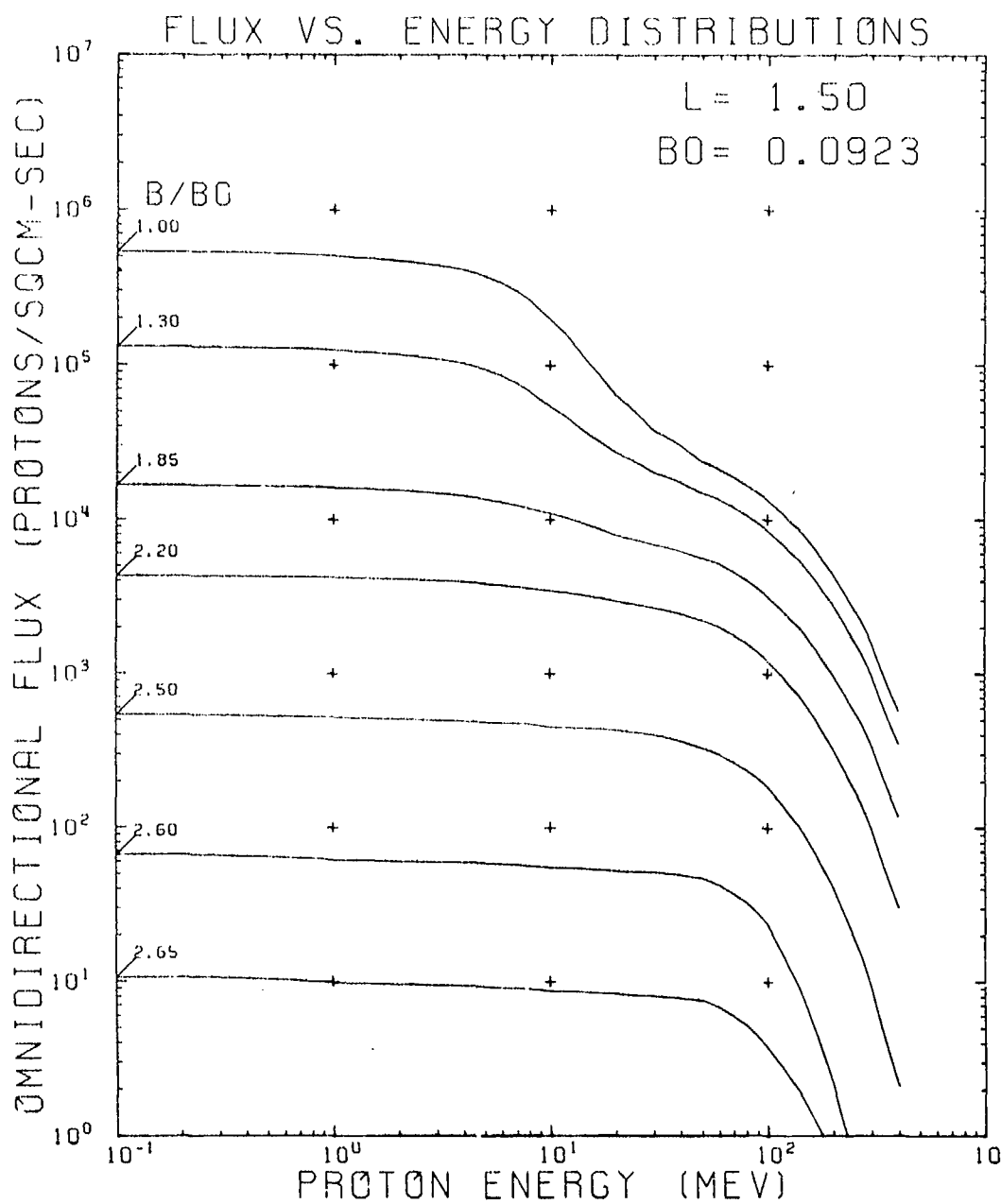


Figure 4-10. Integral spectra of AP8MIN omnidirectional fluxes of protons for various values of B/BC at $L = 1.5$ (Reference 12).

4 January 1977

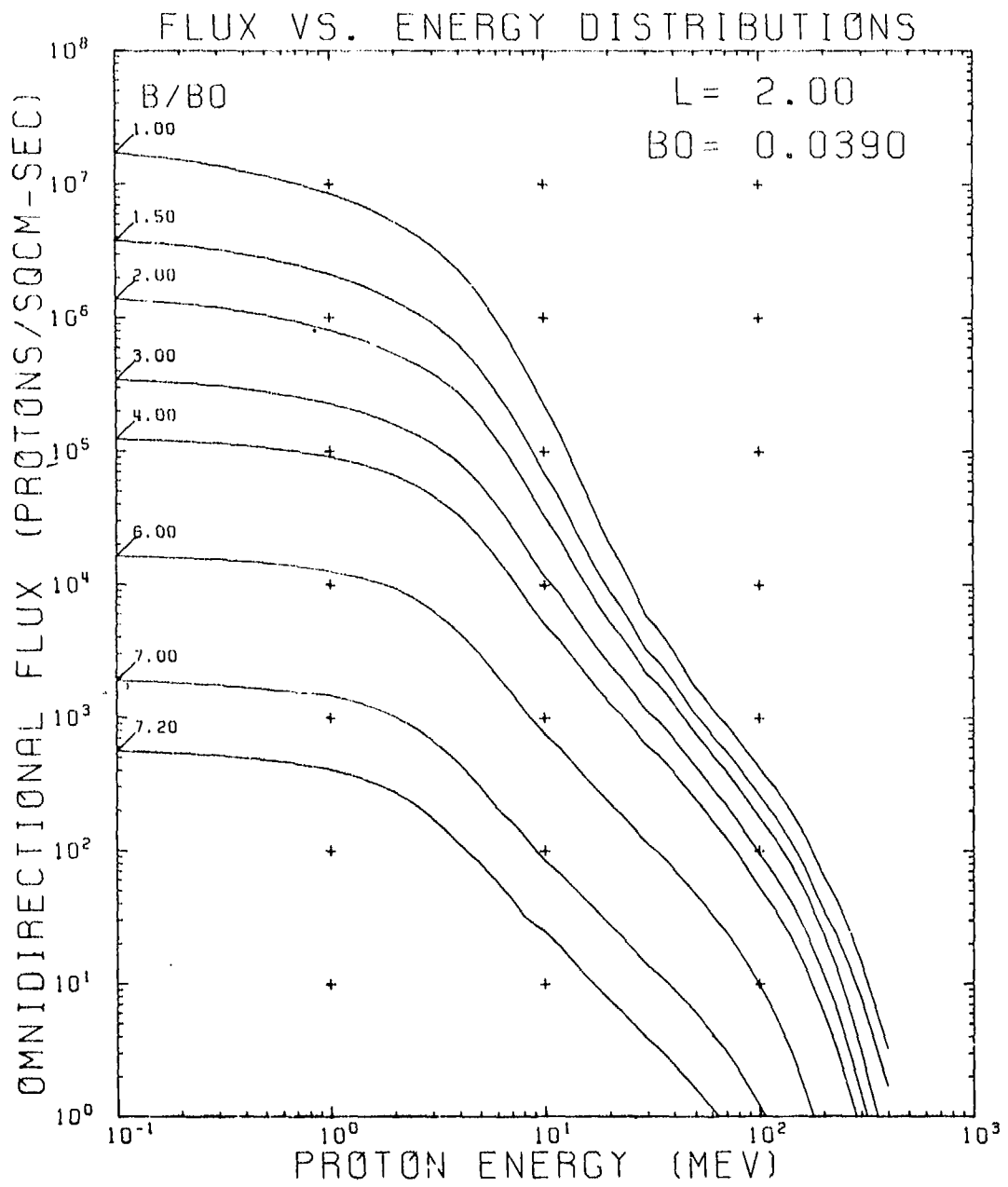


Figure 4-11. Integral spectra of AP8MIN omnidirectional fluxes of protons for various values of B at $L = 2.0$ (Reference 12).

4 January 1977

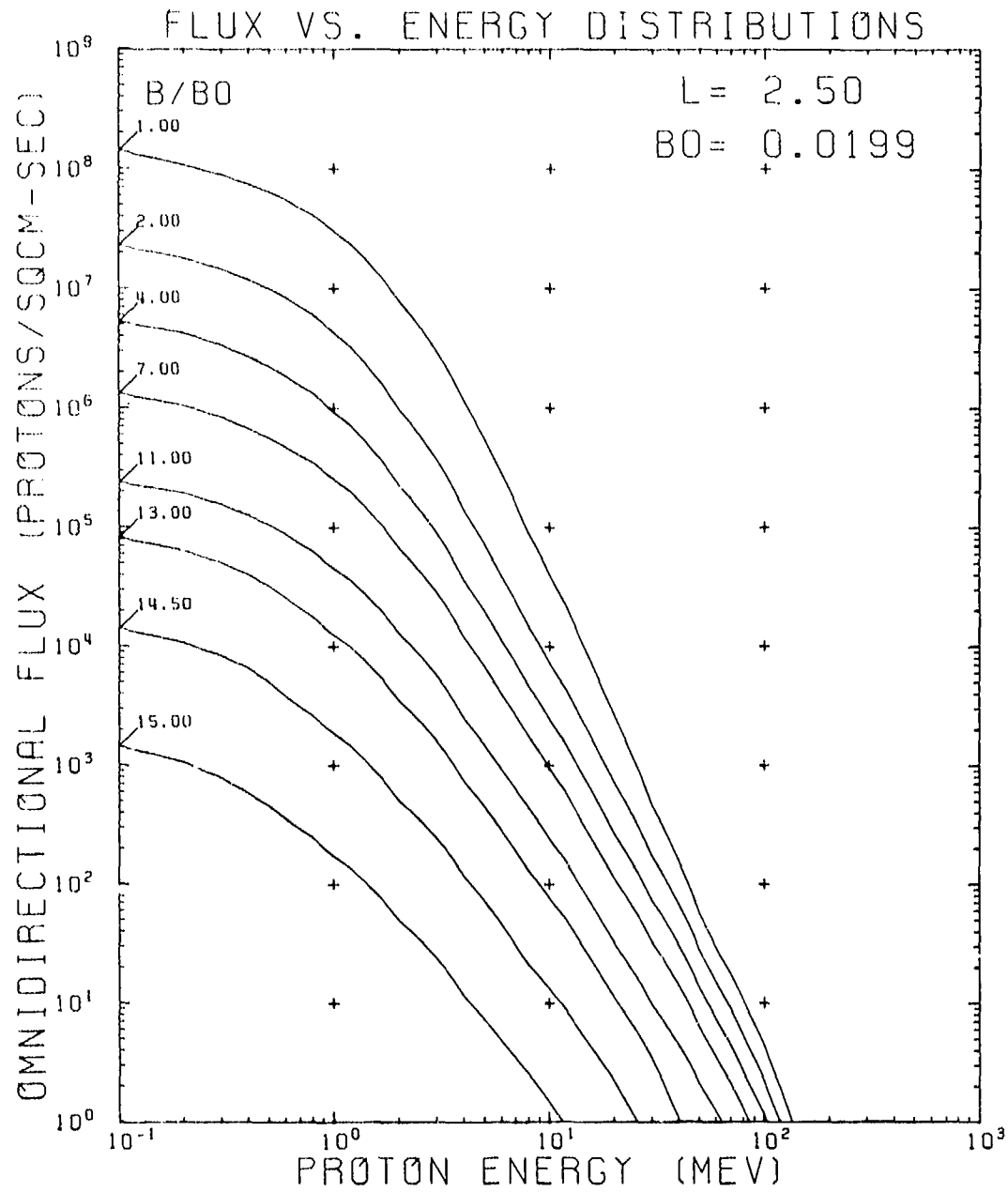


Figure 4-12. Integral spectra of AP8MIN omnidirectional fluxes of protons for various values of B at L = 2.5 (Reference 12).

4 January 1977

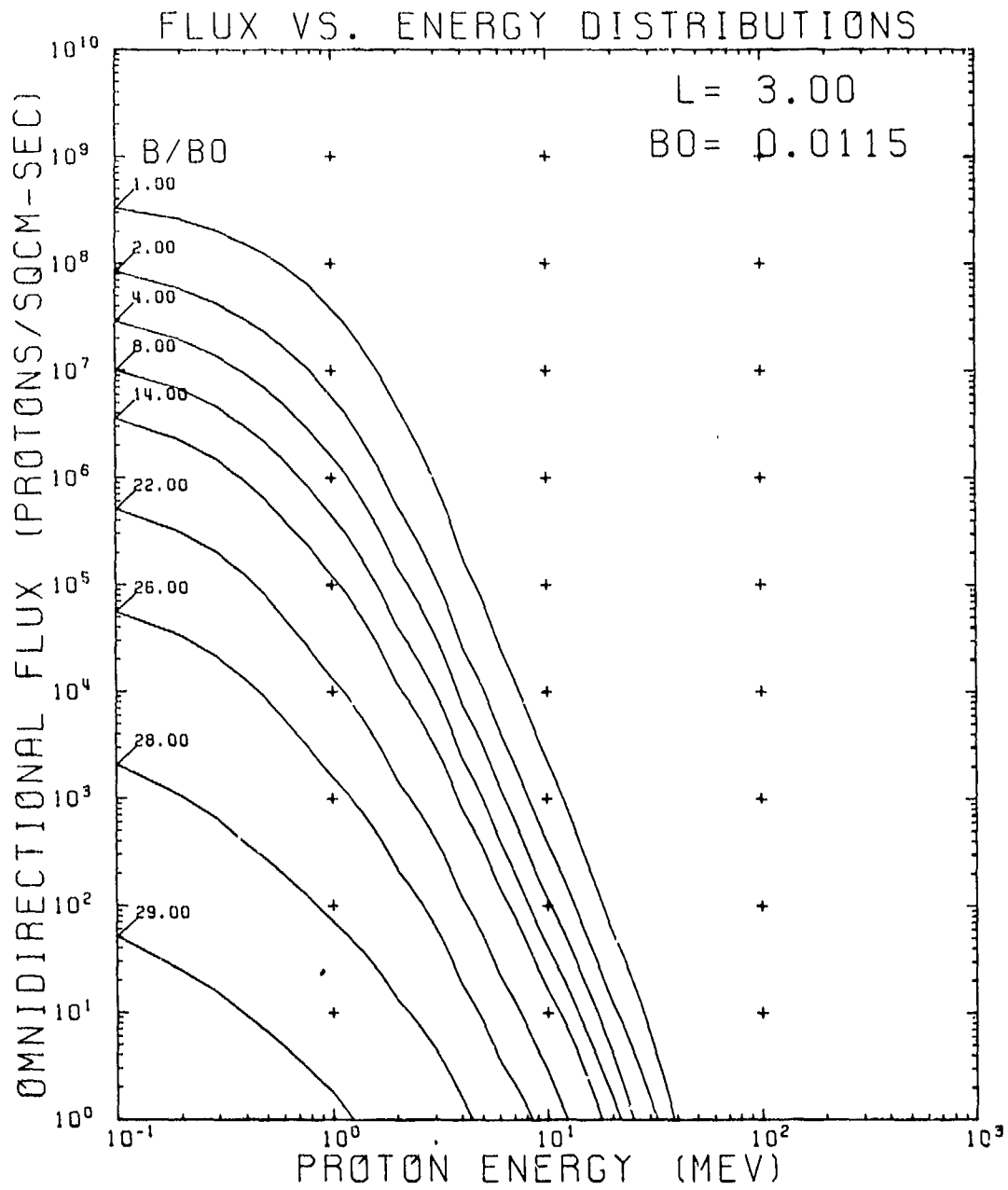


Figure 4-13. Integral spectra of AP8MIN omnidirectional fluxes of protons for various values of B at L = 3.0 (Reference 12).

4 January 1977

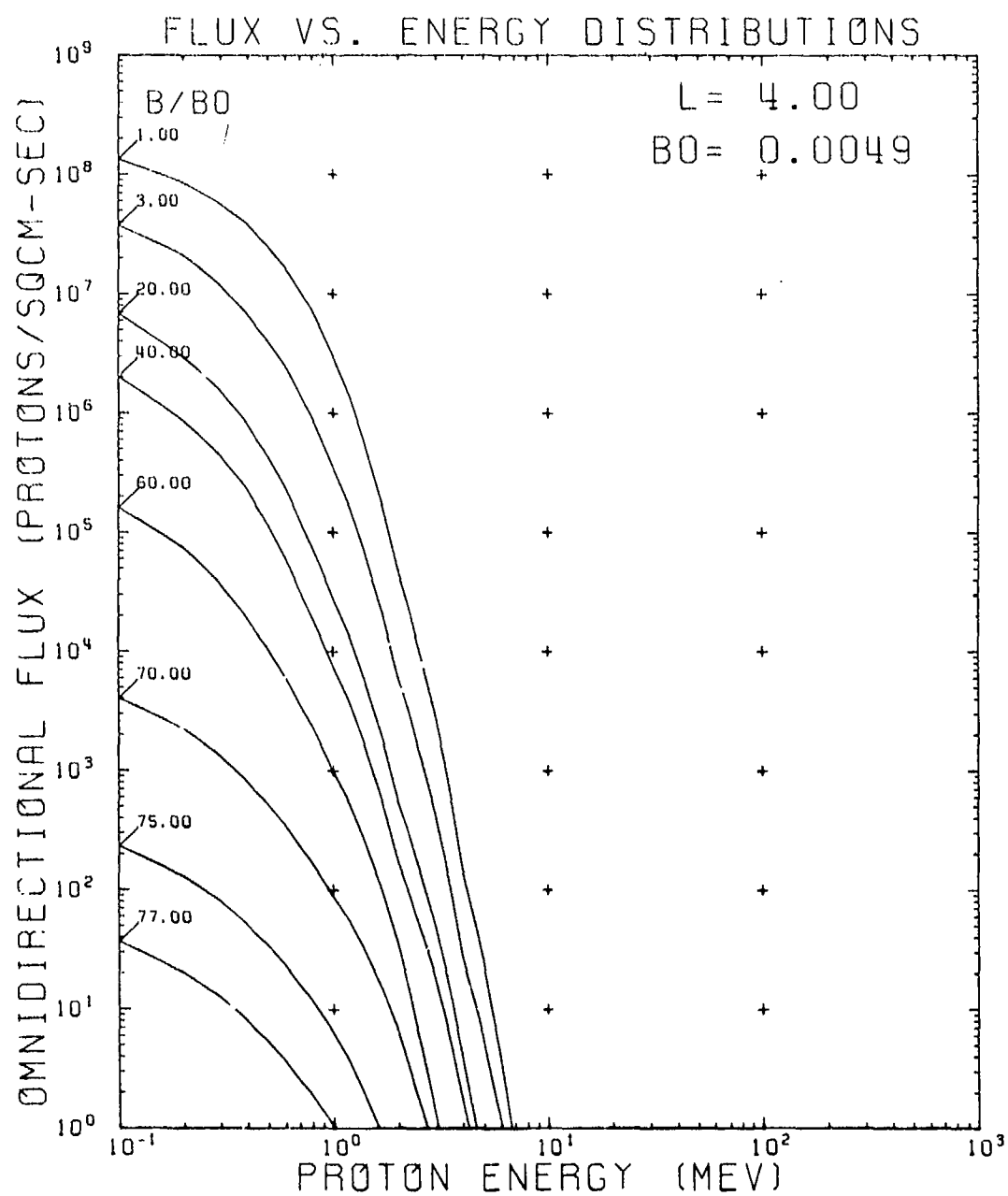


Figure 4-14. Integral spectra of AP8MIN omnidirectional fluxes of protons for various values of B at L = 4.0 (Reference 12).

4 January 1977

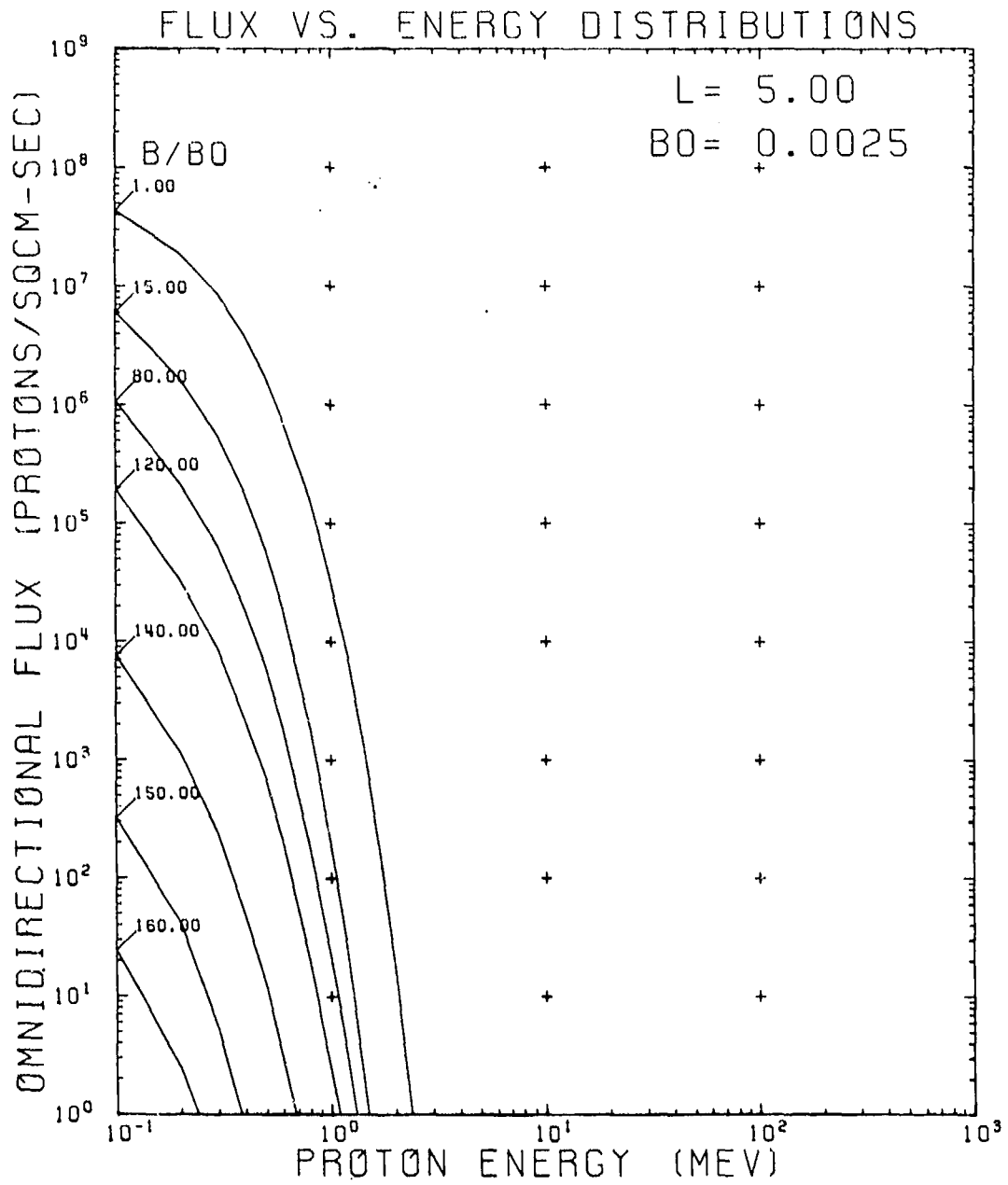


Figure 4-15. Integral spectra of AP8MIN omnidirectional fluxes of protons for various values of B at L = 5.0 (Reference 12).

4 January 1977

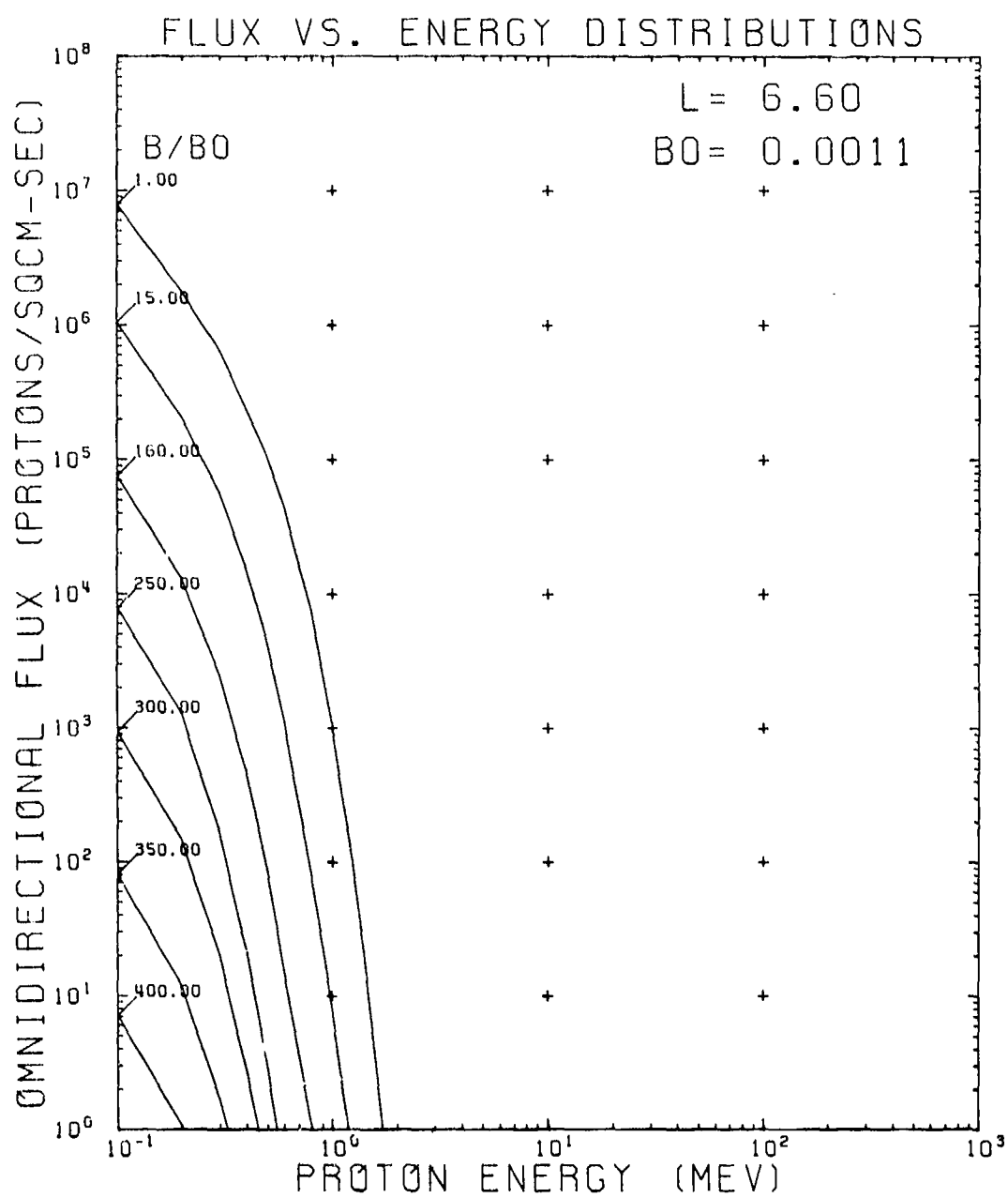


Figure 4-16. Integral spectra of AP8MIN omnidirectional fluxes of protons for various values of B at L = 6.6 (Reference 12).

4 January 1977

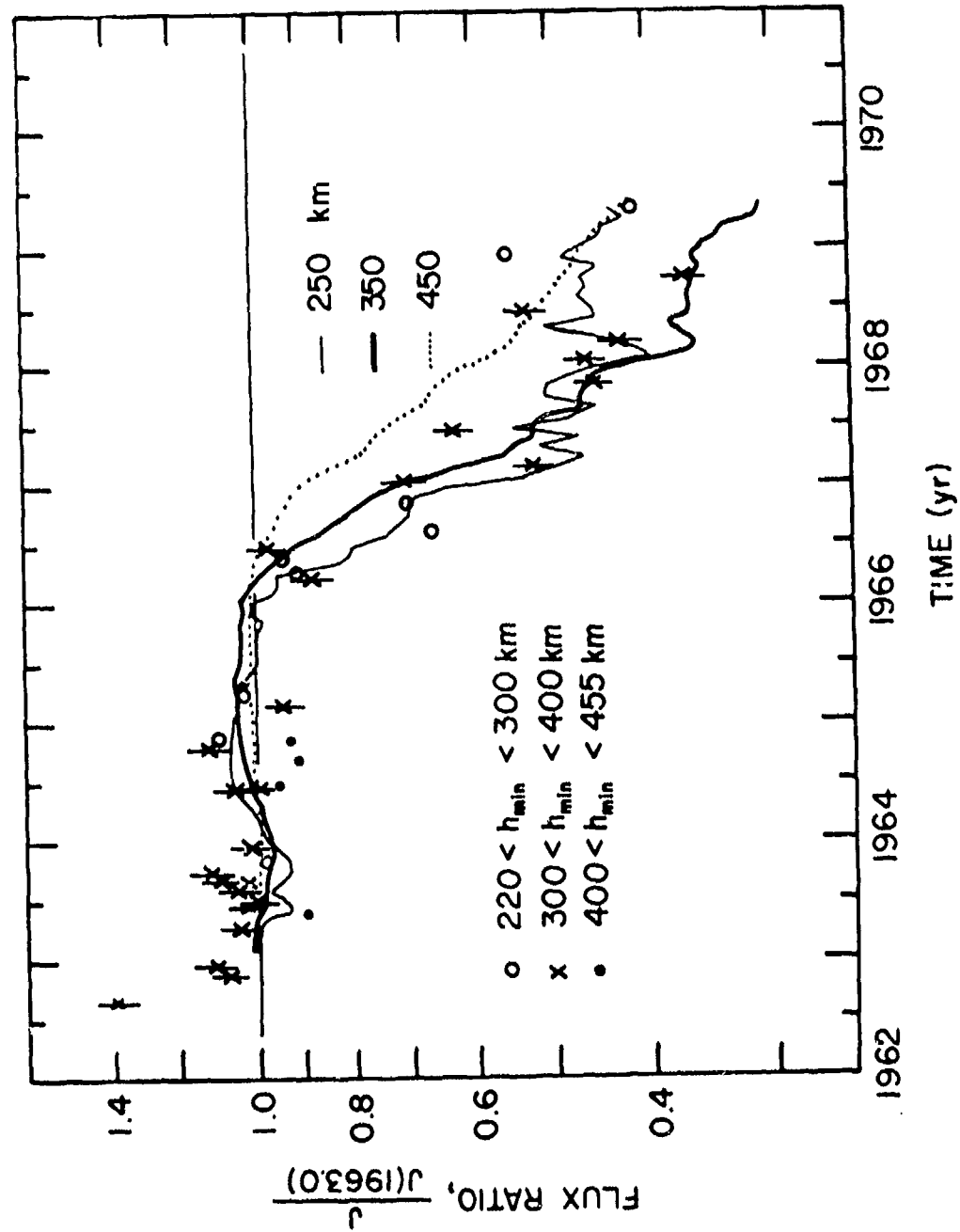


Figure 4-17. Computed ratio of $J(t)/J(1963.0)$ at 60 MeV and minimum mirror point altitudes of 250, 350, and 450 km, $L = 1.40$, between January 1963 and May 1969 (Reference 19).

4 January 1977

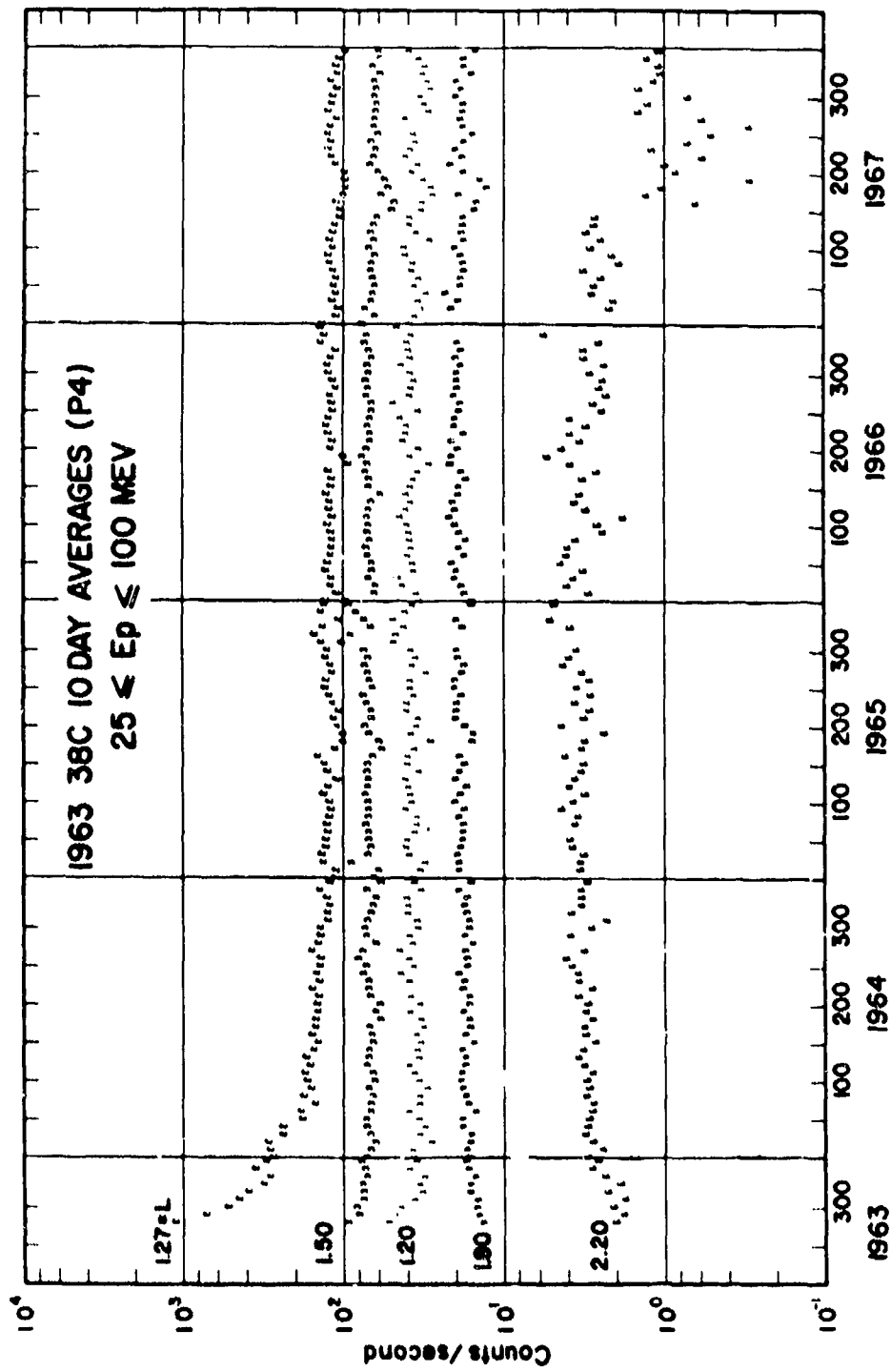


Figure 4-18. Time behavior of high-energy protons (Reference 19).

4 January 1977

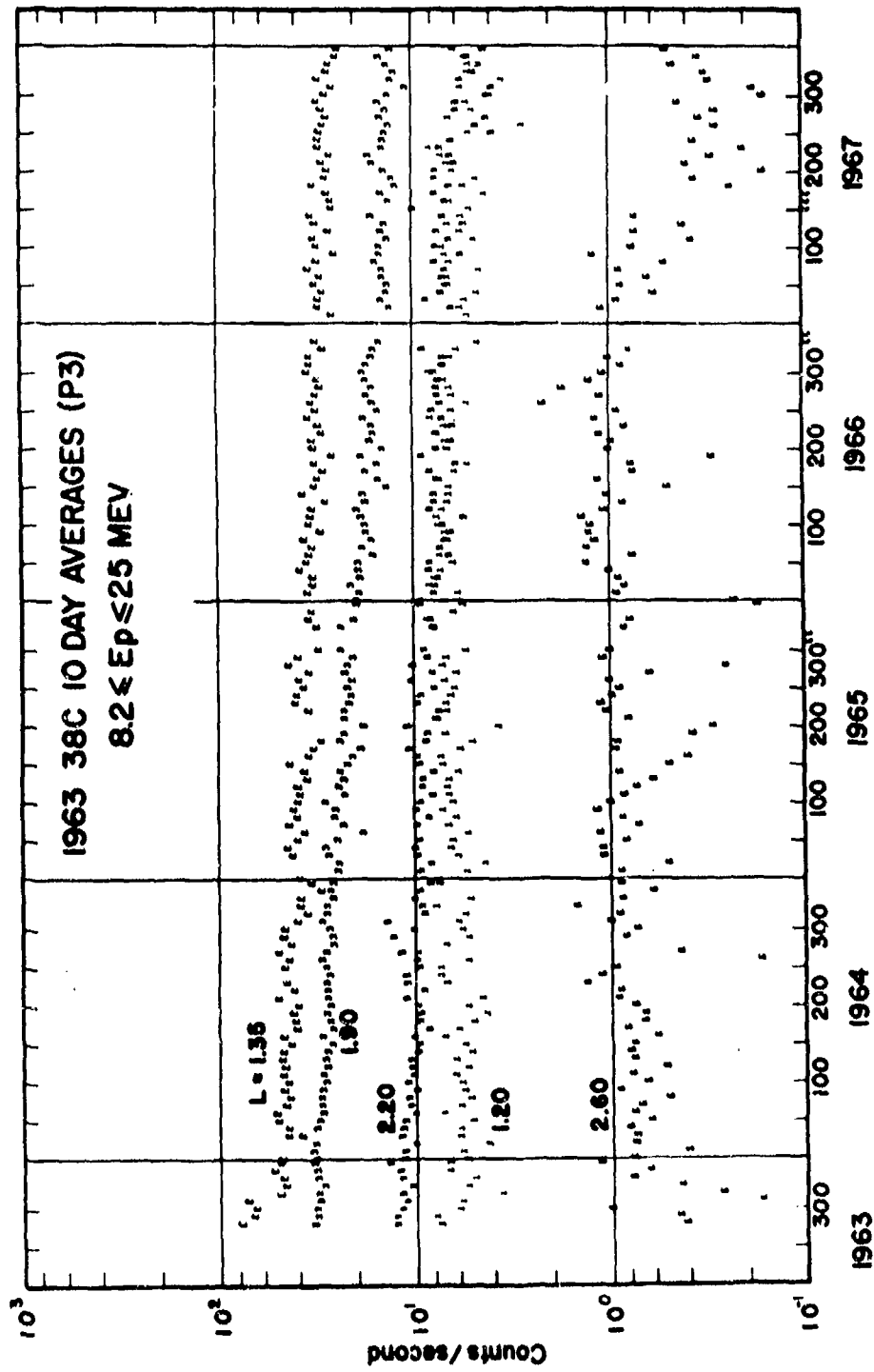


Figure 4-19. Time behavior of medium-energy protons (Reference 19).

4 January 1977

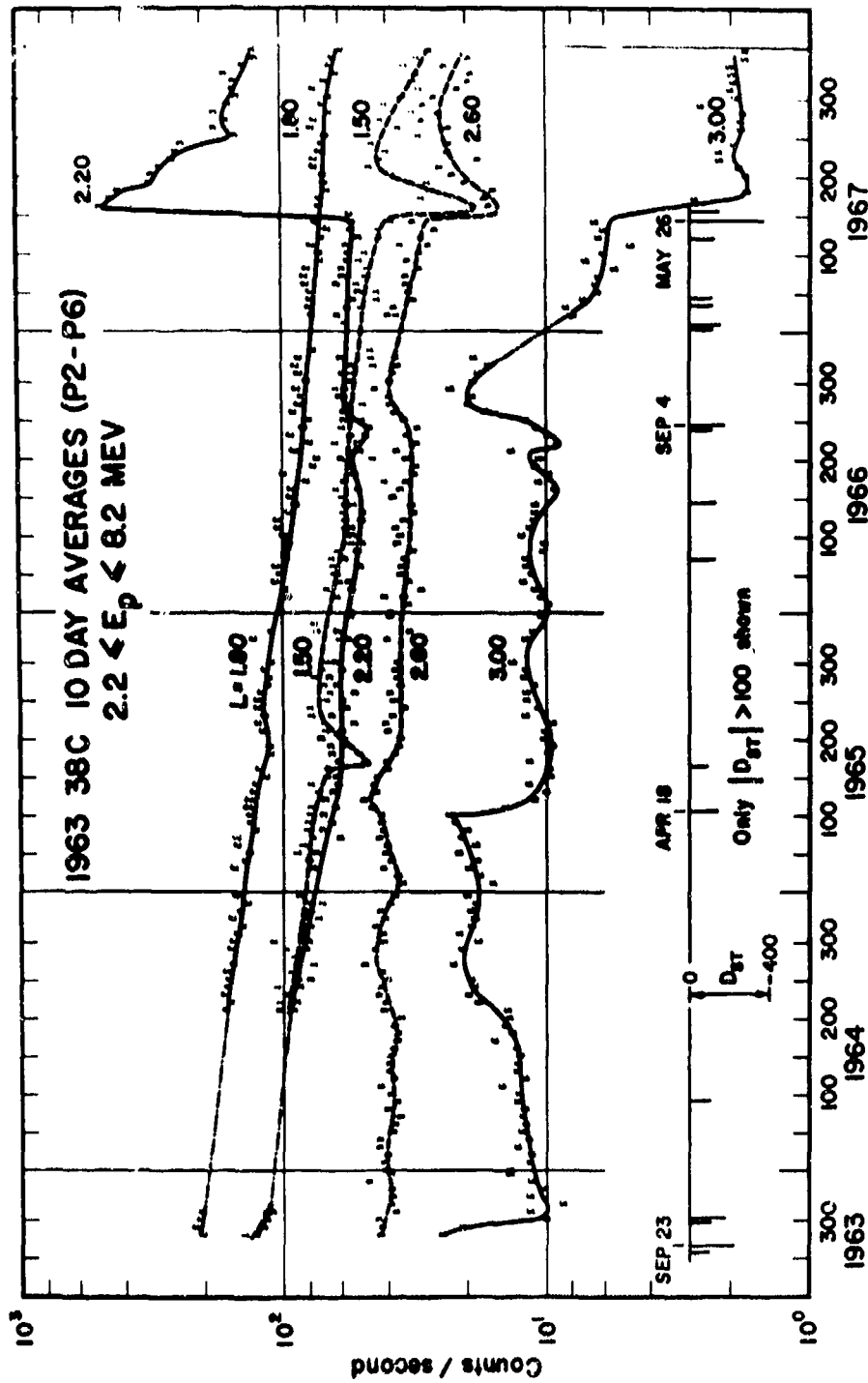


Figure 4-20. Time behavior of low-energy protons. The initial increase at $L = 2.2$ is contaminated by electrons which 20 days later have decayed to the point of not contributing to the count rate (Reference 19).

4 January 1977

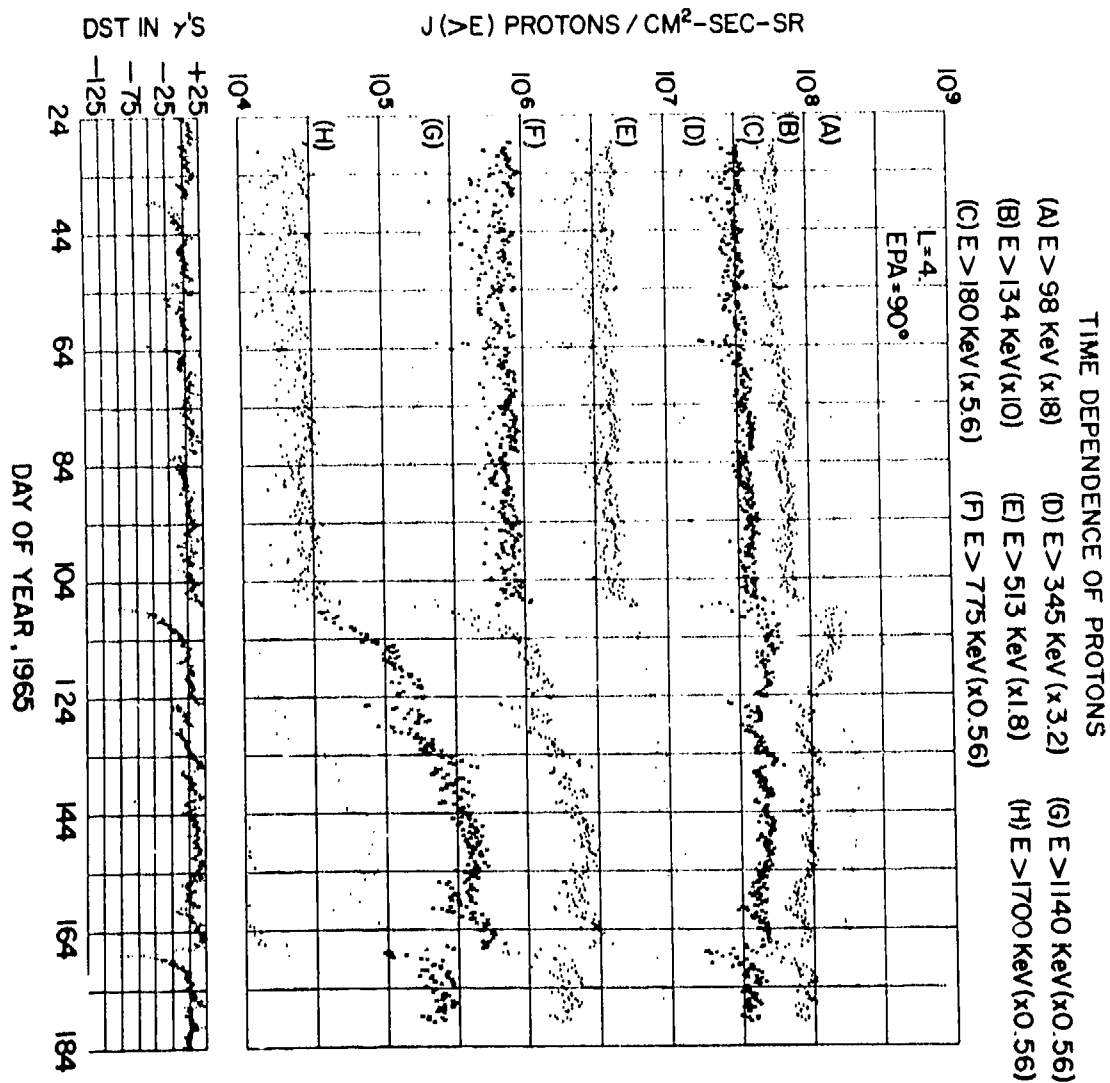


Figure 4-22. Time behavior of low-energy protons at L = 4.0. The curves are displaced to avoid overlap, and values for curves A to H must be multiplied by 10 raised to the exponents: -1.25, -1.00, -0.75, -0.50, -0.25, 0.25, 0.25, and 0.25 to obtain the integral intensity (Reference 20).

4 January 1977

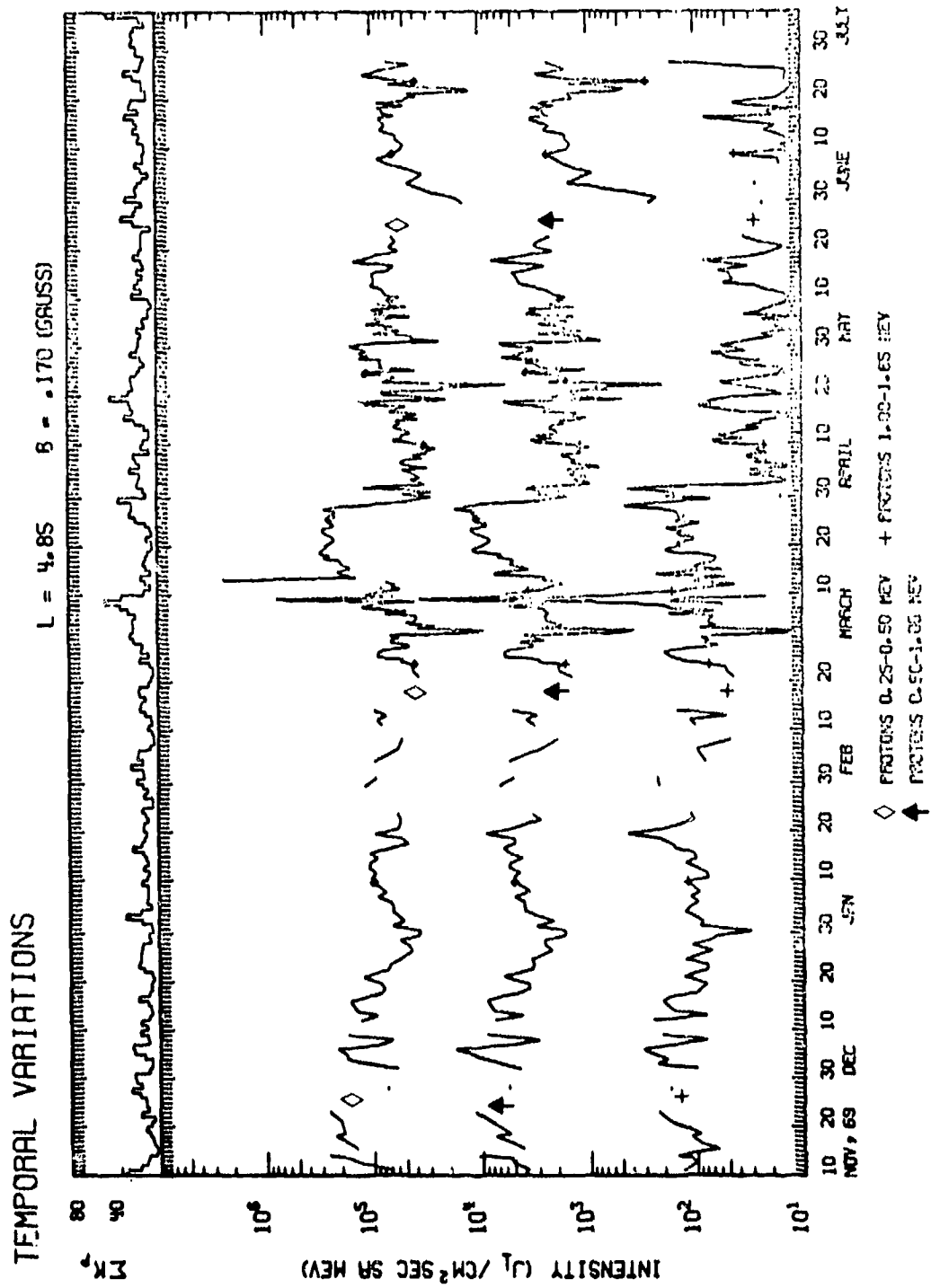


Figure 4-23. Low-altitude proton observations at $L = 4.85$ with energies between 0.25 and 1.65 MeV, as obtained by the Azur satellite (Reference 21).

4 January 1977

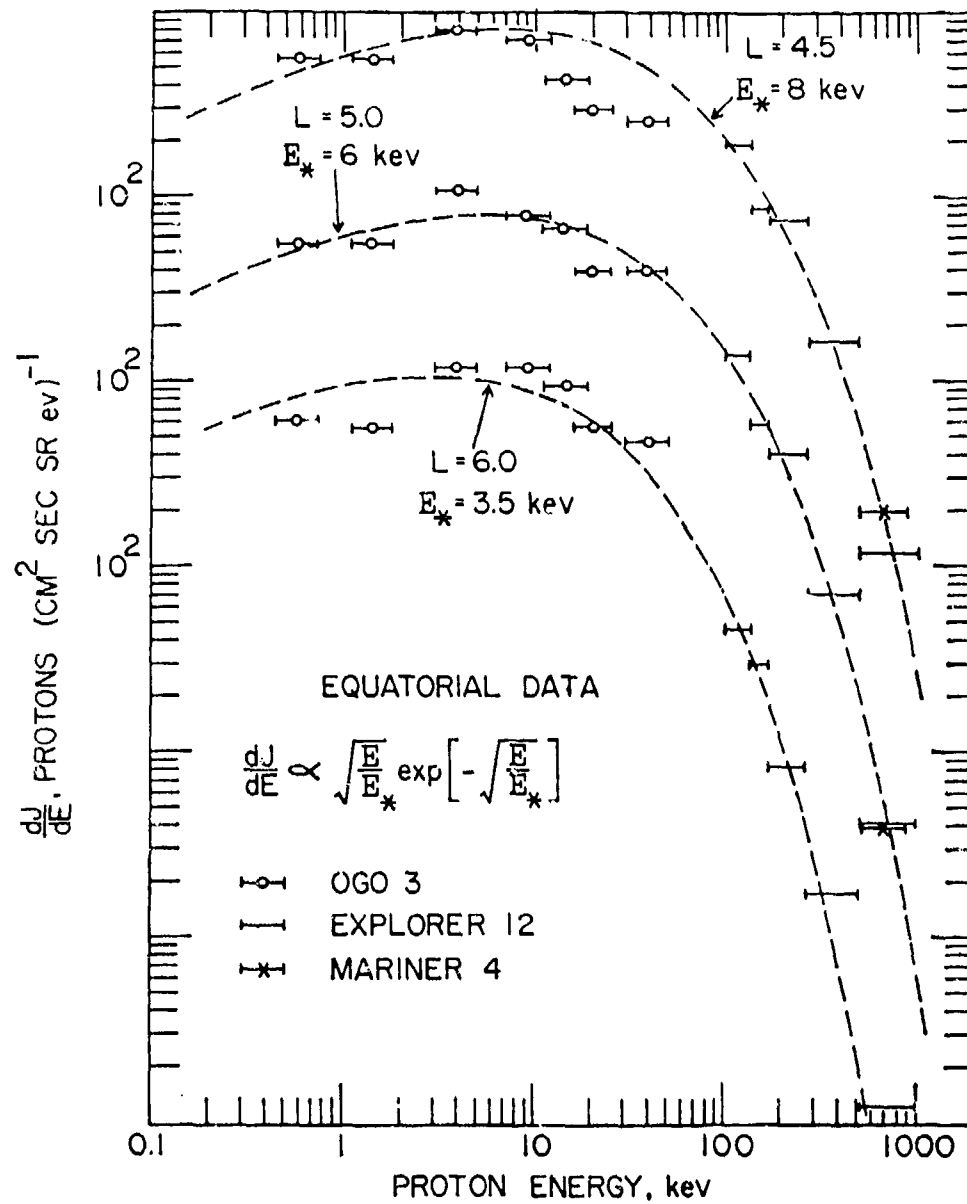


Figure 4-24. Differential spectra of directional proton fluxes over the energy range of $200 \text{ eV} \leq E \leq 1 \text{ MeV}$ mirroring at the magnetic equator as compiled from observations with OGO 3, Explorer 12, and Mariner 4. The ordinate scales for the proton spectra at $L = 4.0$, 5.0 , and 6.0 have been displaced by factors of 10, as noted on the left ordinate scale (Reference 28).

4 January 1977

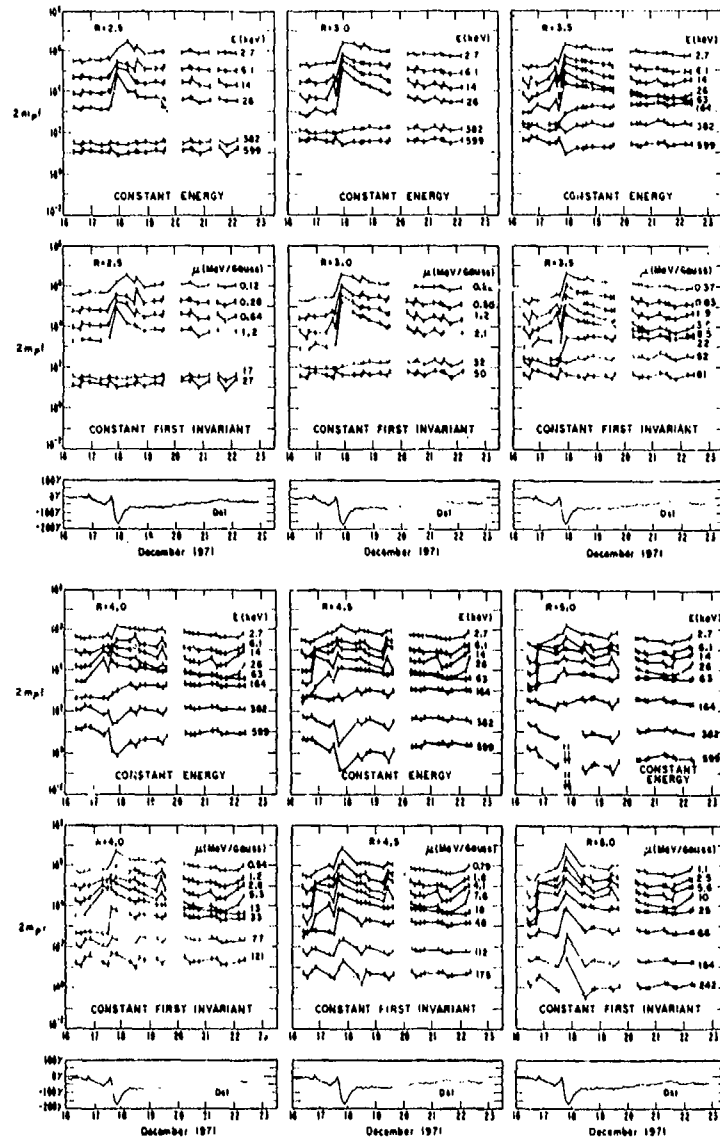


Figure 4-25. Distribution function, multiplied by two times the proton mass for equatorially mirroring protons as a function of time throughout the period of the December 17, 1971 storm. Curves are shown at both constant energy E and constant first adiabatic invariant μ . Dst is also shown. Note that the pre-storm intensities for energies of ≤ 26 KeV are upper limits to the true intensities at $L = 2.5$ and 3.0 (Reference 29).

4 January 1977

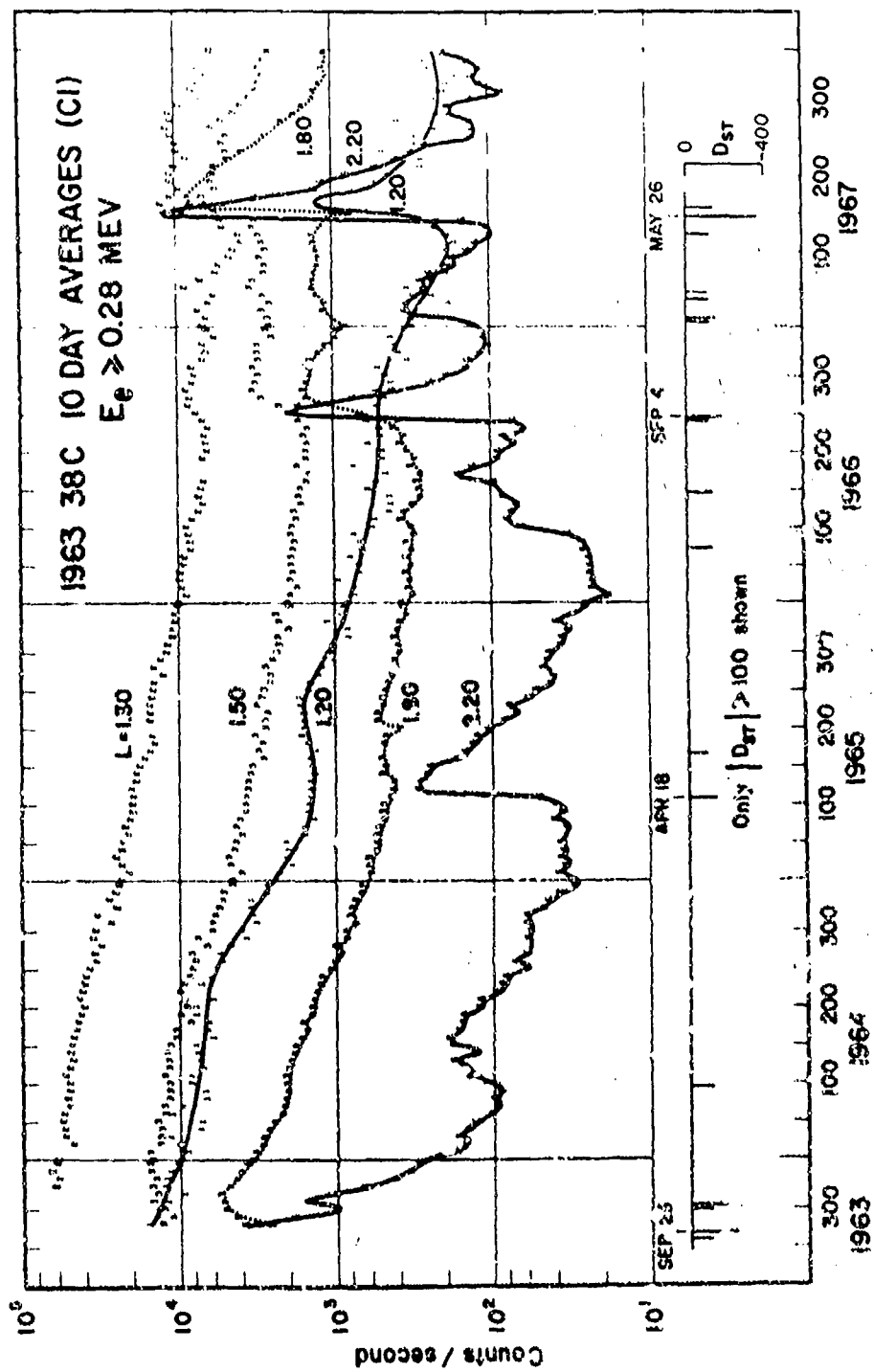


Figure 4-27. Time behavior of >280-KeV electrons in the inner zone (Reference 33).

4 January 1977

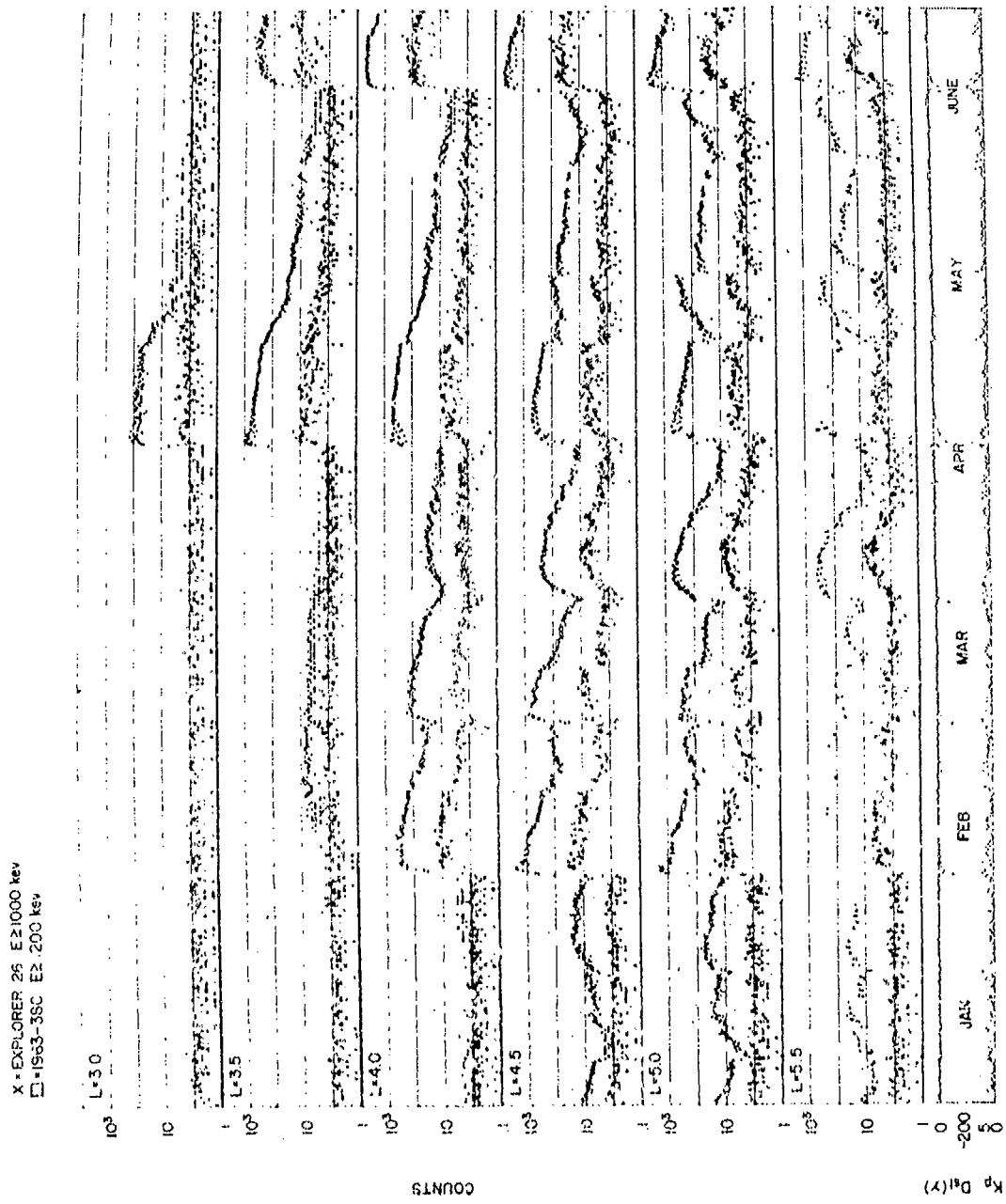


Figure 4-28. Time behavior of >1-MeV electrons in the outer zone (Reference 34).

4 January 1977

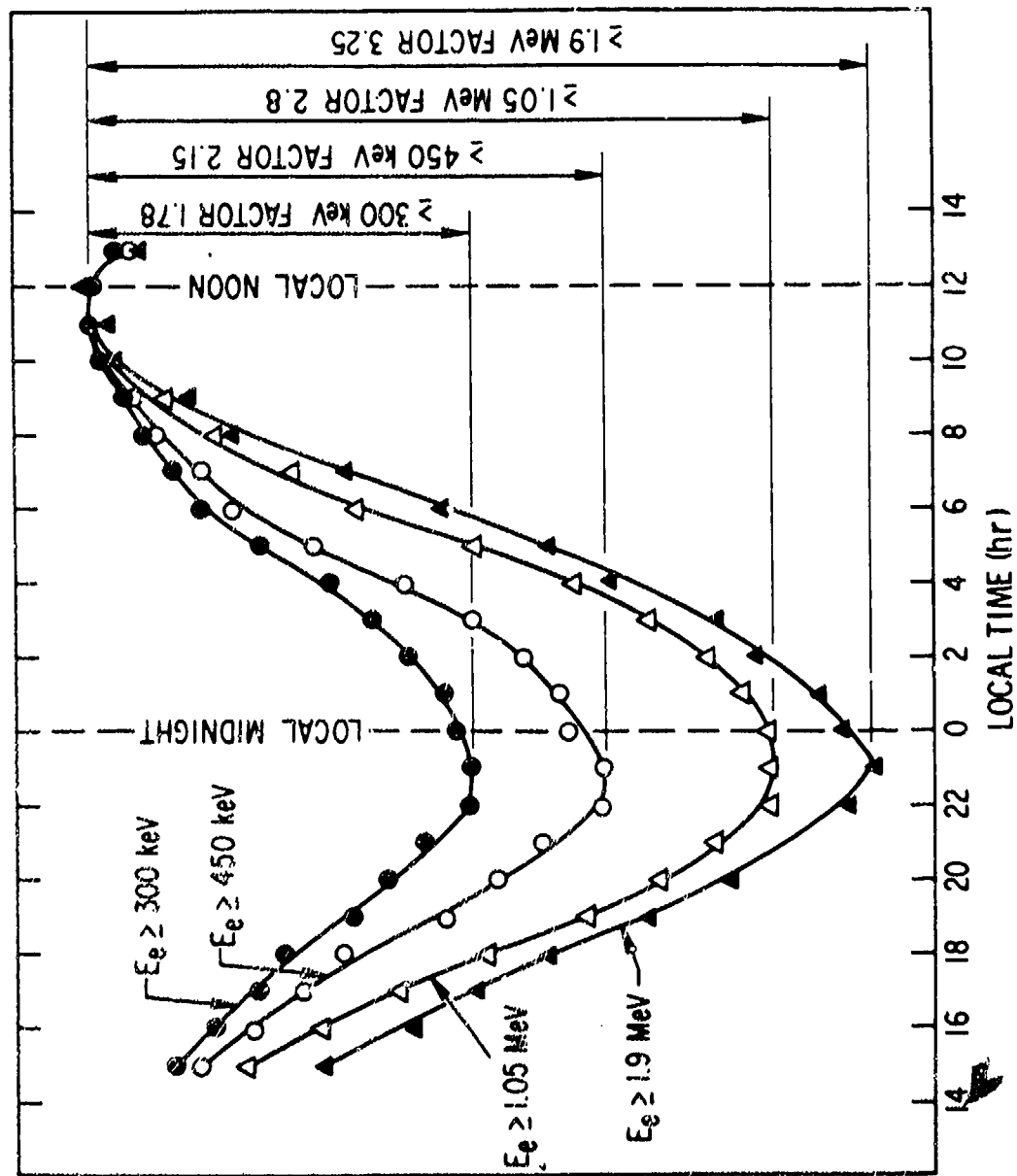


Figure 4-29. The diurnal variation of the mean of logarithm of ATS 1 observation. Data are normalized at 1100 local time (Reference 32).

4 January 1977

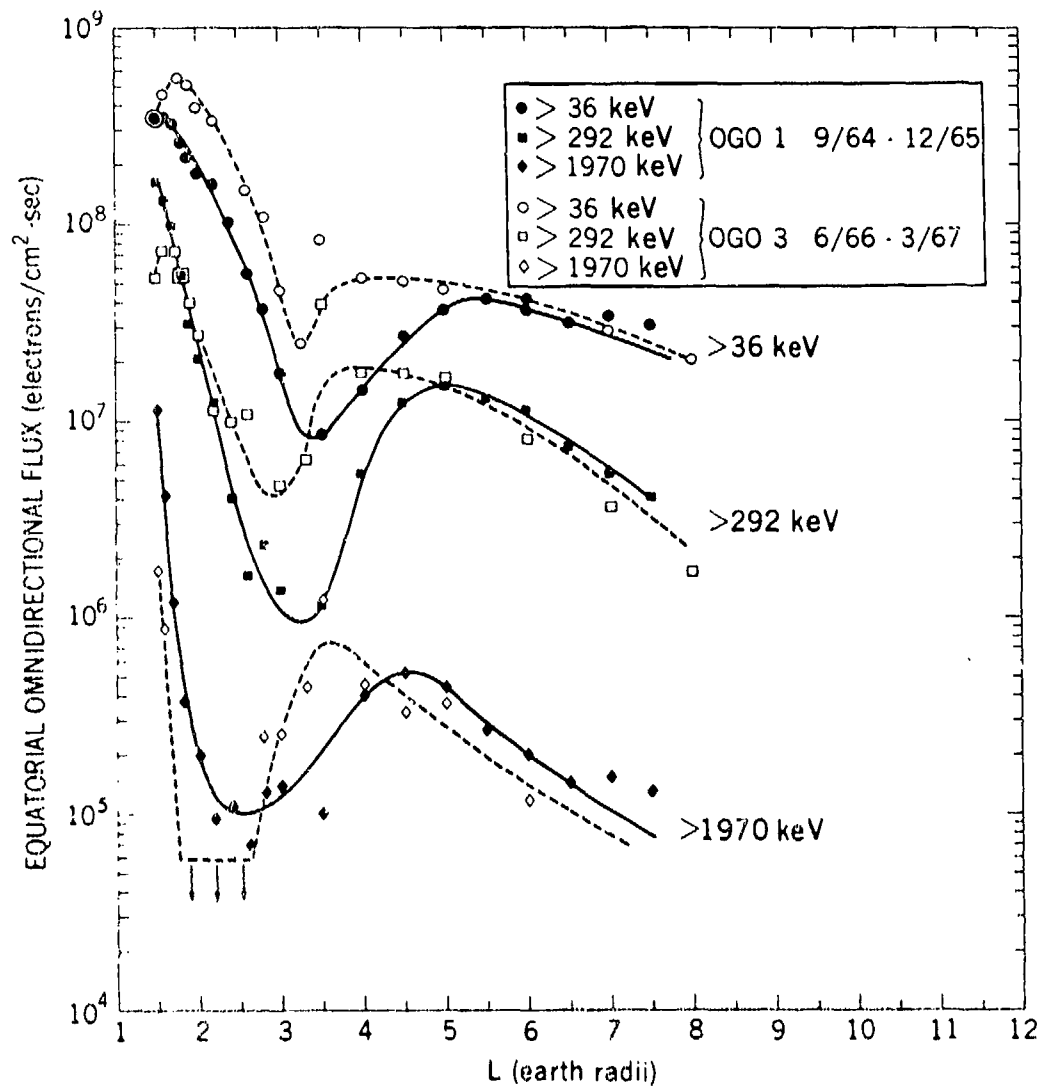


Figure 4-30. Equatorial radial profiles of OGO 1 and OGO 3 data, showing the solar-cycle effect (Reference 36).

4 January 1977

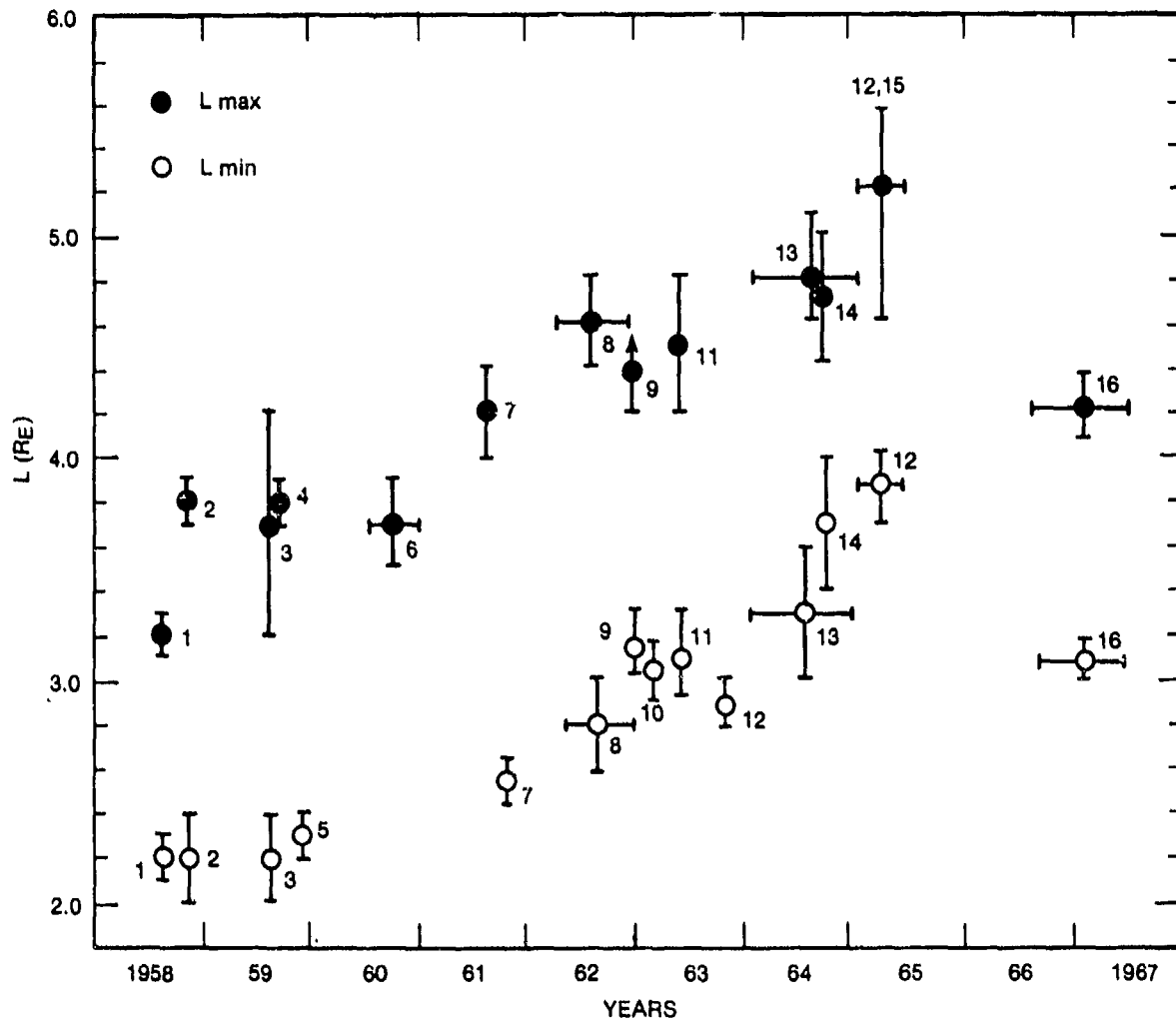


Figure 4-31. Position of the slot minimum (L min) and the outer belt maximum (L max) in various periods of the solar cycle. The numbers denote measurements obtained from satellites: 1 - Explorer 4; 2 - Pioneer 3; 3 - Explorer 6; 4 - Luna 2; 5 - Explorer 7; 6 - Spaceship-satellite 2; 7 - Explorer 12; 8 - Cosmos 4, 7, 9; 9 - Explorer 15; 10 - Injun 3; 11 - Explorer 14; 12 - 1963-38C; 13 - Electron 1, 2, 3, 4; 14 - OGO 1; 15 - Explorer 26 (Reference 35); and 16 - OGO 3 (Reference 36).

4 January 1977

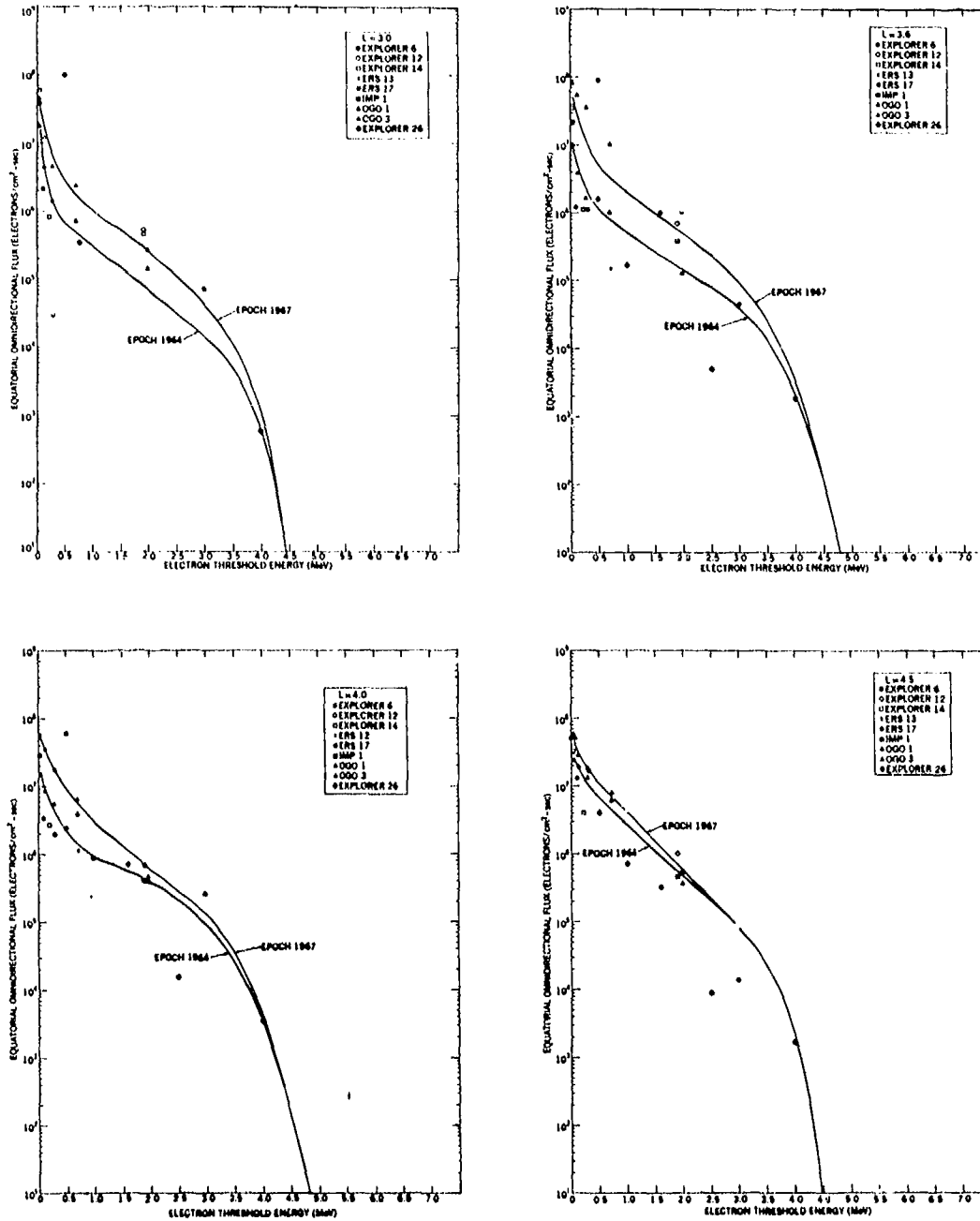


Figure 4-32. Comparison of AE 4 model spectra with the source data at L = 3.0, 3.6, 4.0, and 4.5 (Reference 36).

4 January 1977

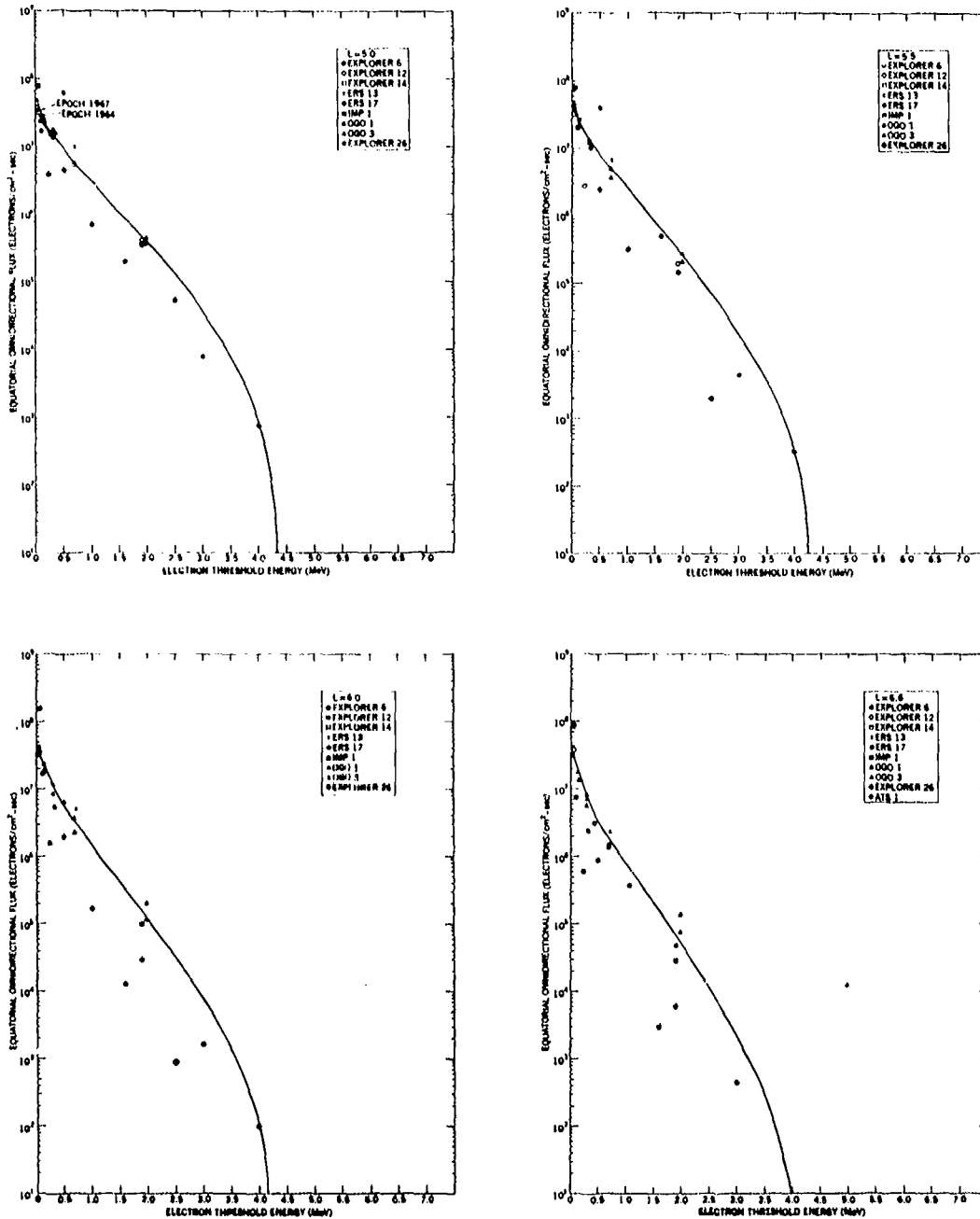


Figure 4-33. Comparison of AE 4 model spectra with the source data at L = 5.0, 5.5, 6.0, and 6.6 (Reference 36).

4 January 1977

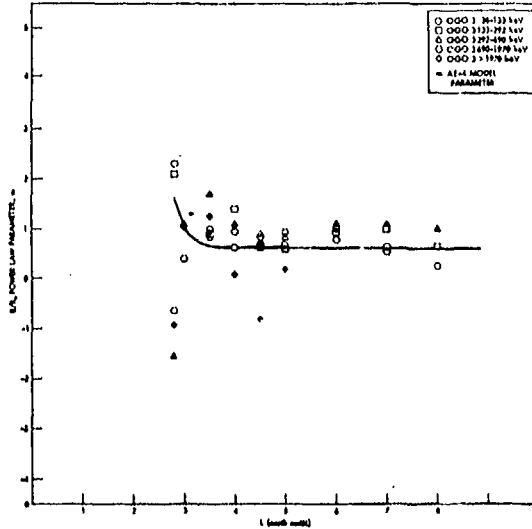
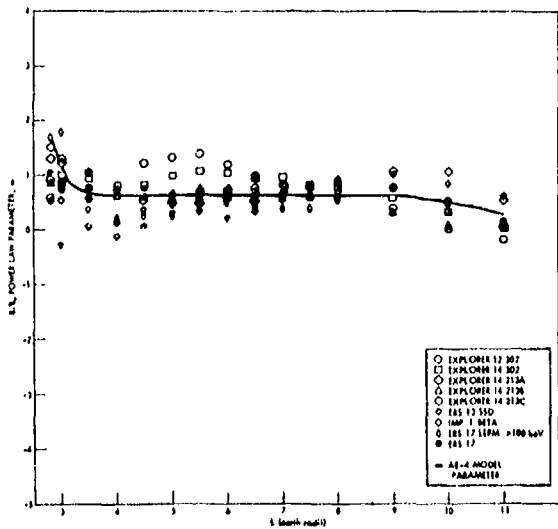
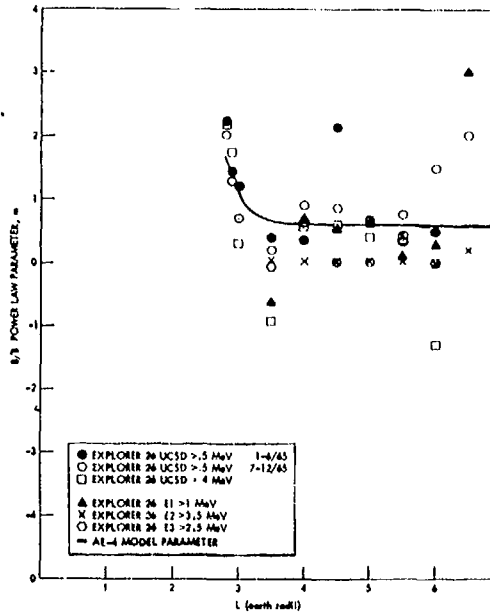
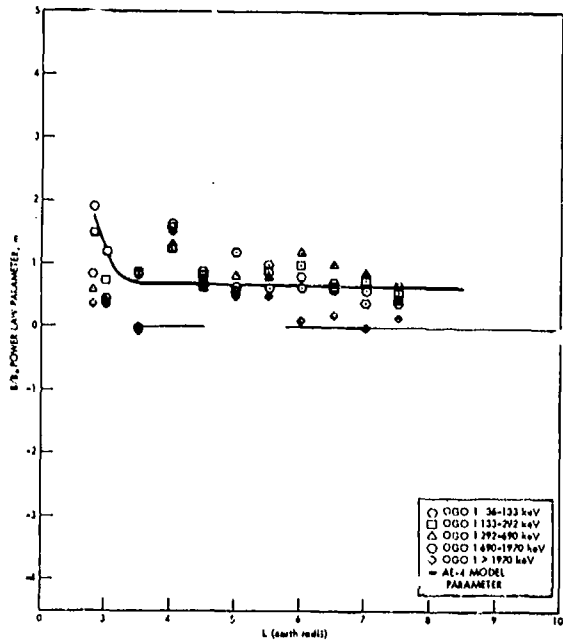


Figure 4-34. Comparison of model power law parameter for B/B₀ dependence with the calculated parameter from various source data sets (Reference 36).

4 January 1977

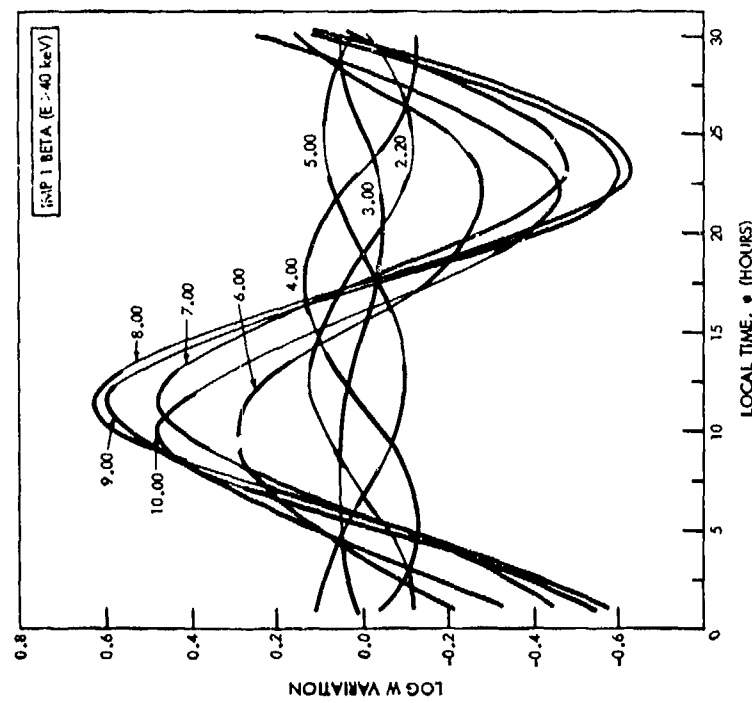
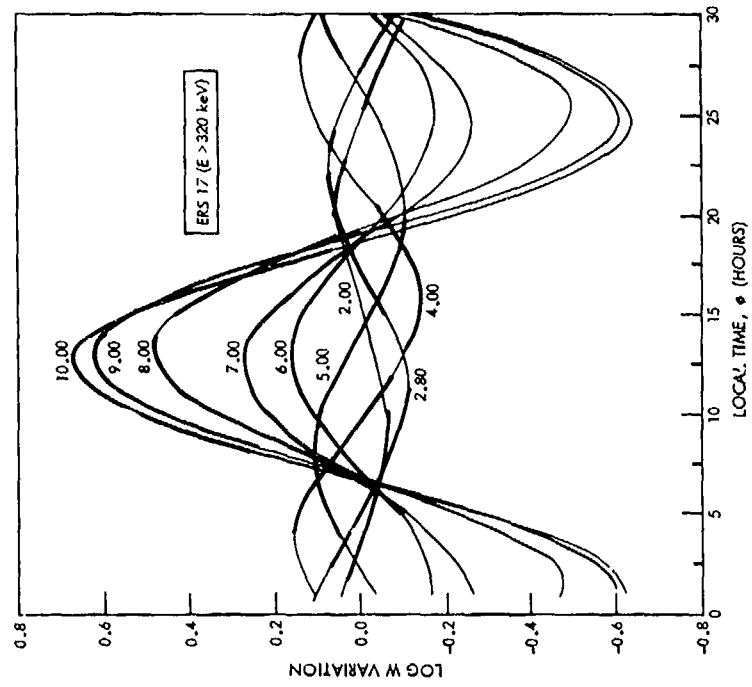


Figure 4-35. Local time variation of the AE 4 model. The thick section of each curve represents the data base (Reference 36).

4 January 1977

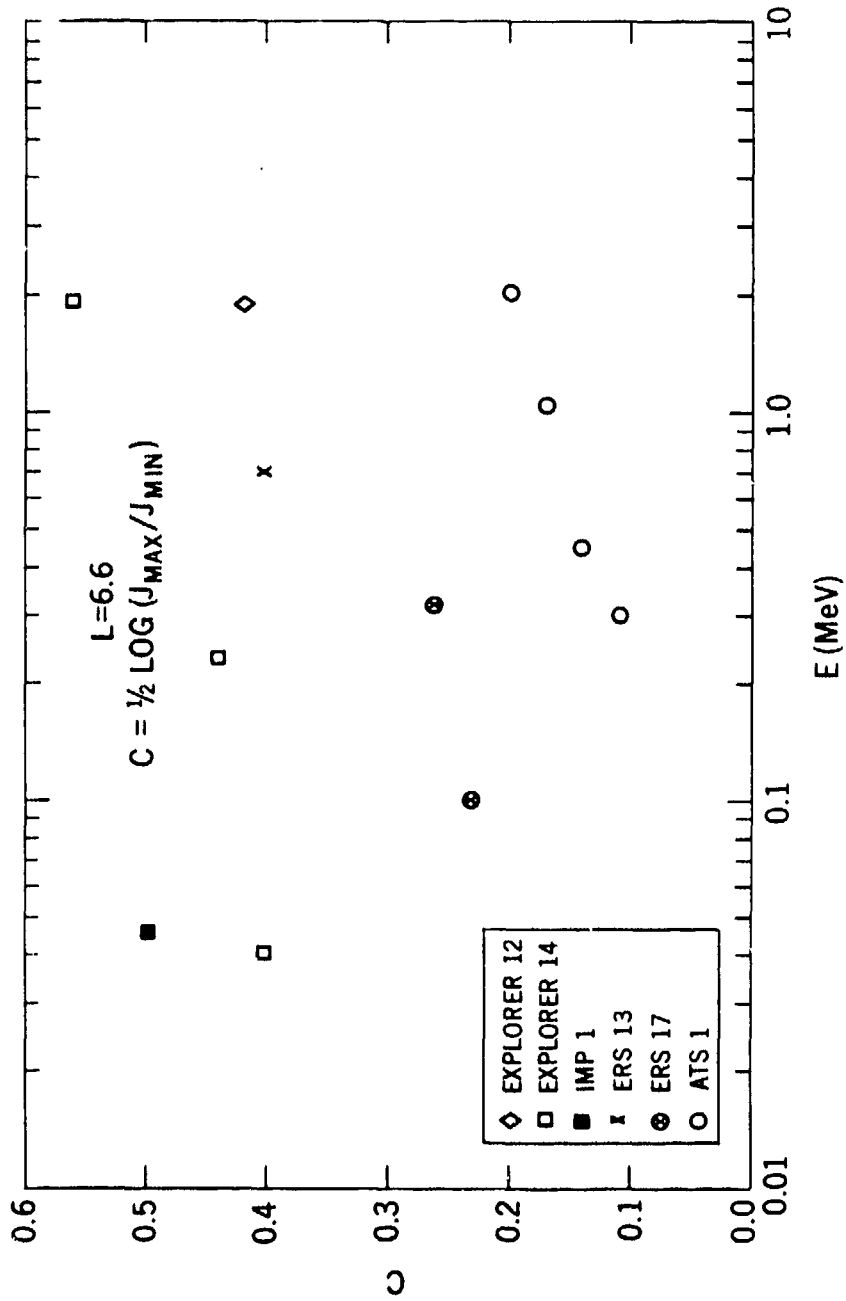


Figure 4-36. Magnitude of the maximum local time variation at $L = 6.6$ for the data set of different epochs: Explorer 12-1962, Explorer 14-1963, IMP 1-1964, ERS 13-1965, and ATS 1-1967 (Reference 36).

4 January 1977

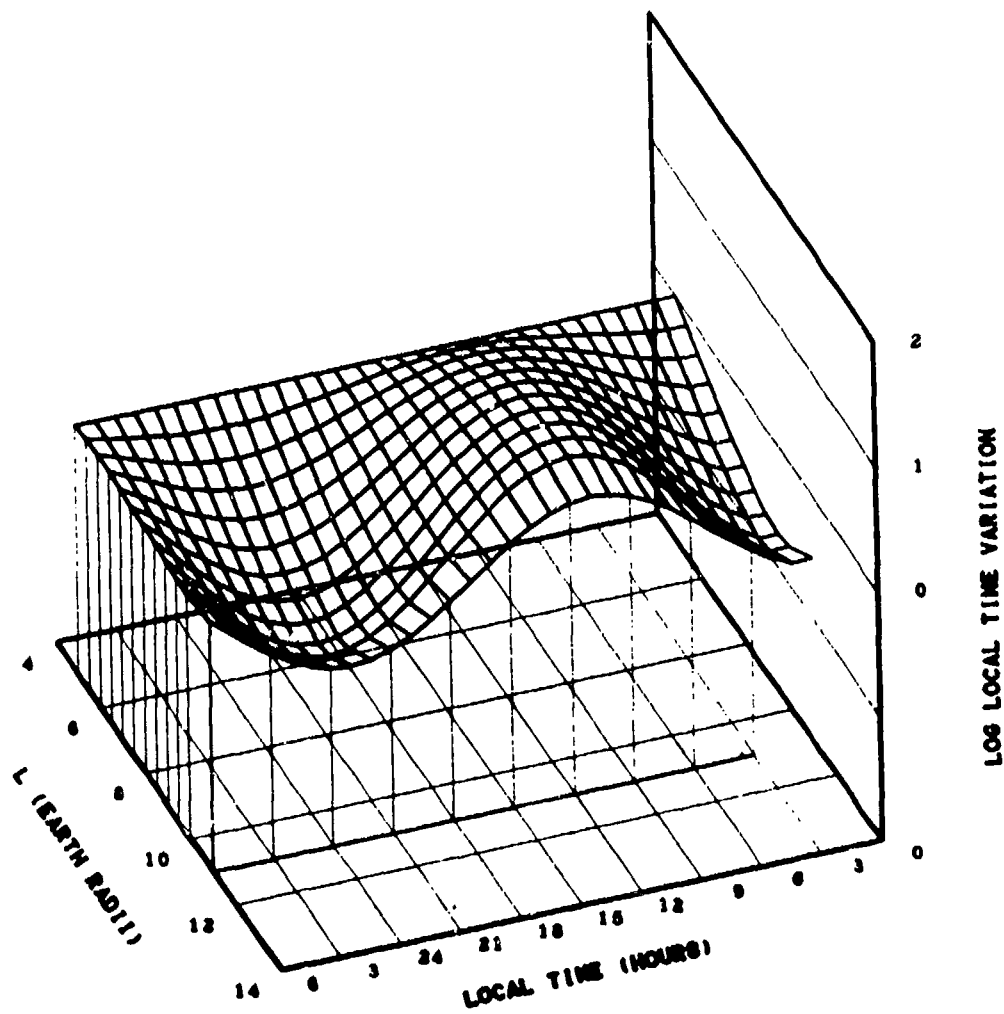


Figure 4-37. Logarithmic presentation of AE 4 local time model for epoch 1964, threshold energy 0.5 MeV (Reference 36).

4 January 1977

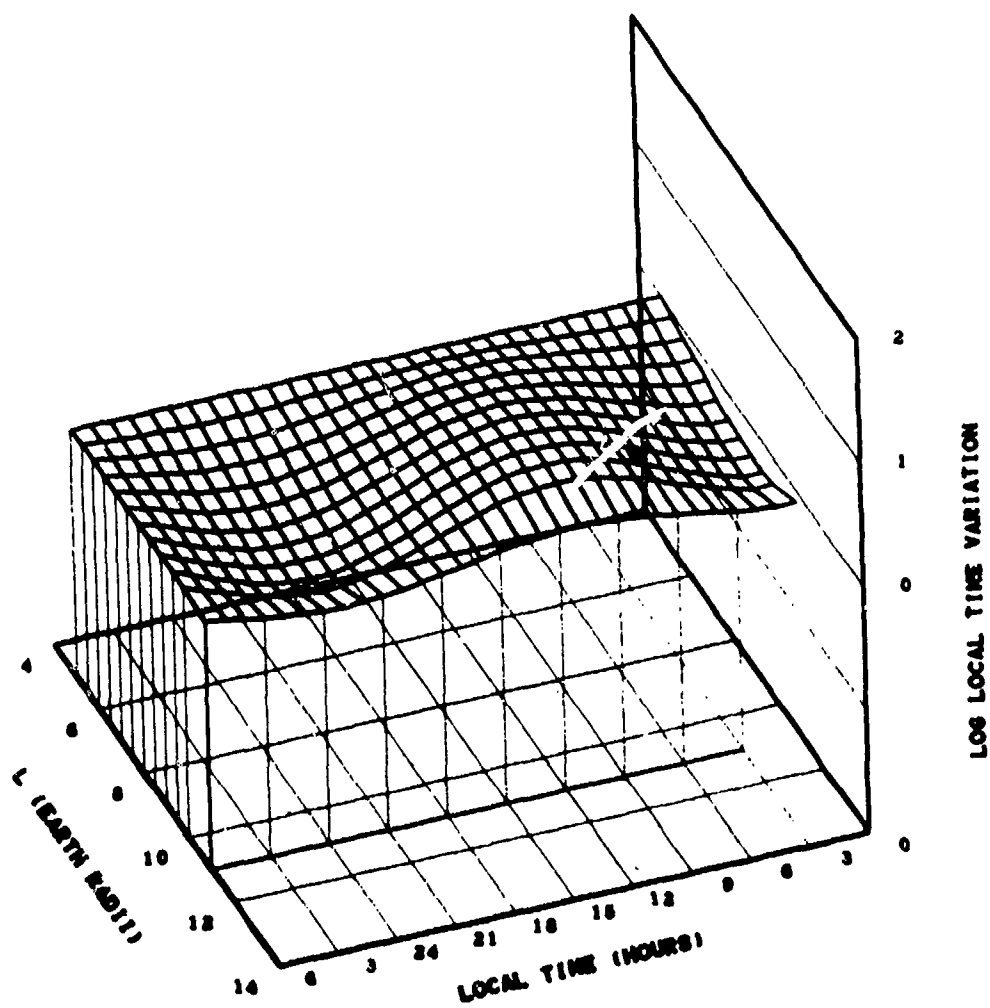


Figure 4-38. Logarithmic presentation of AE 4 local time model for epoch 1967, threshold energy 0.5 MeV (Reference 36).

4 January 1977

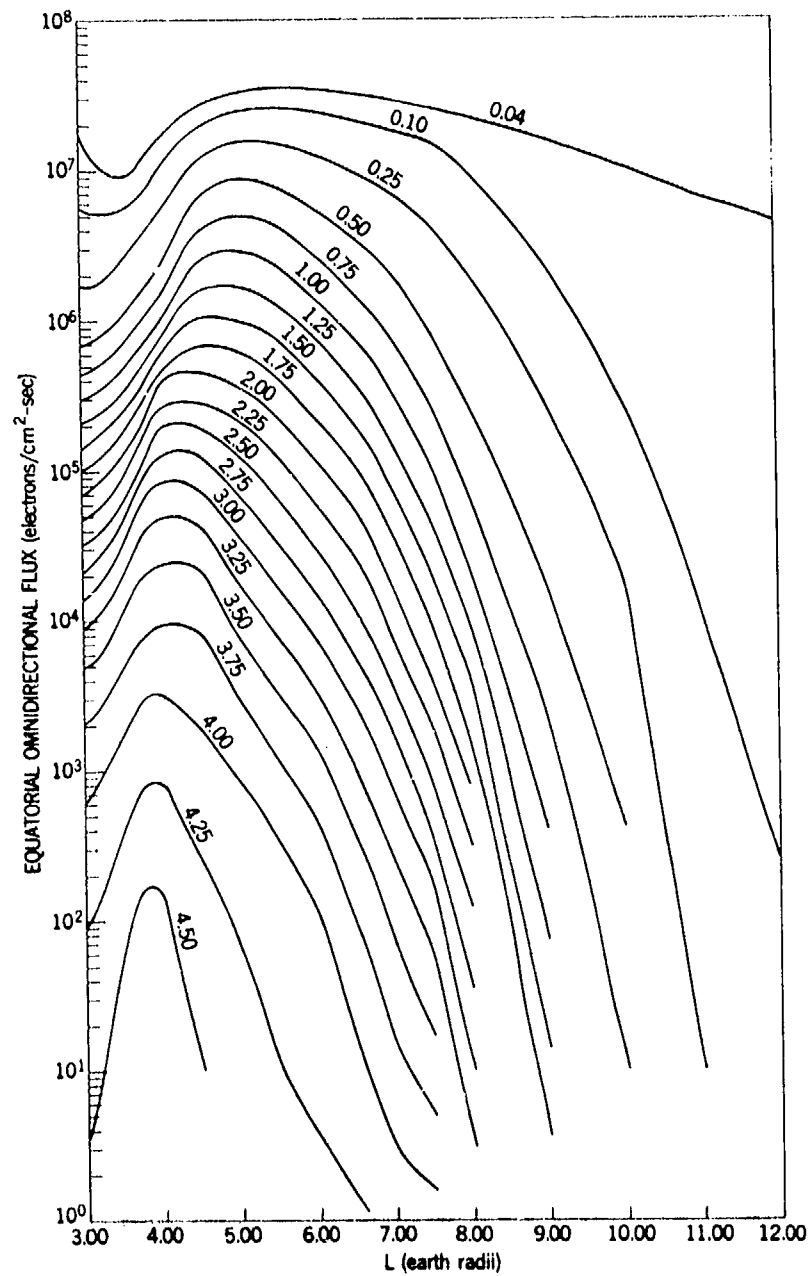


Figure 4-39. AE 4 radial profile of equatorial omnidirectional flux for various energy thresholds, epoch 1964 (Reference 36).

4 January 1977

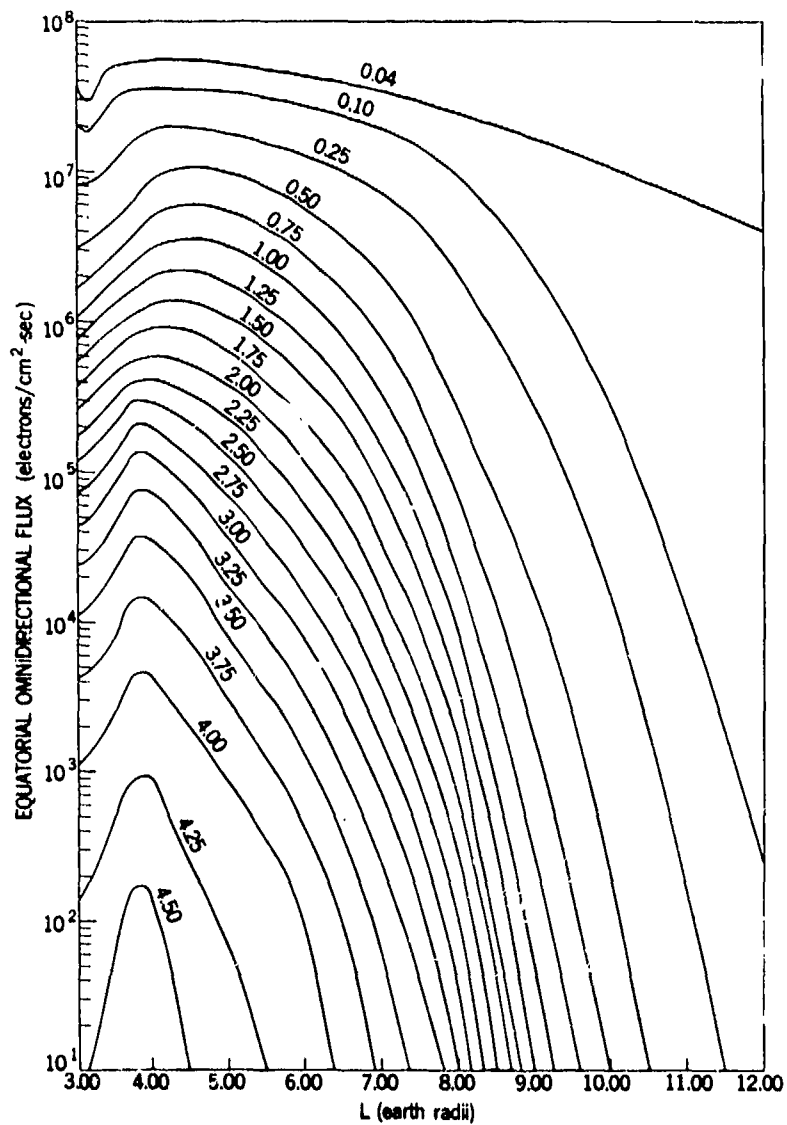


Figure 4-40. AE 4 radial profile of equatorial omnidirectional flux for various energy thresholds, epoch 1967 (Reference 36).

4 January 1977

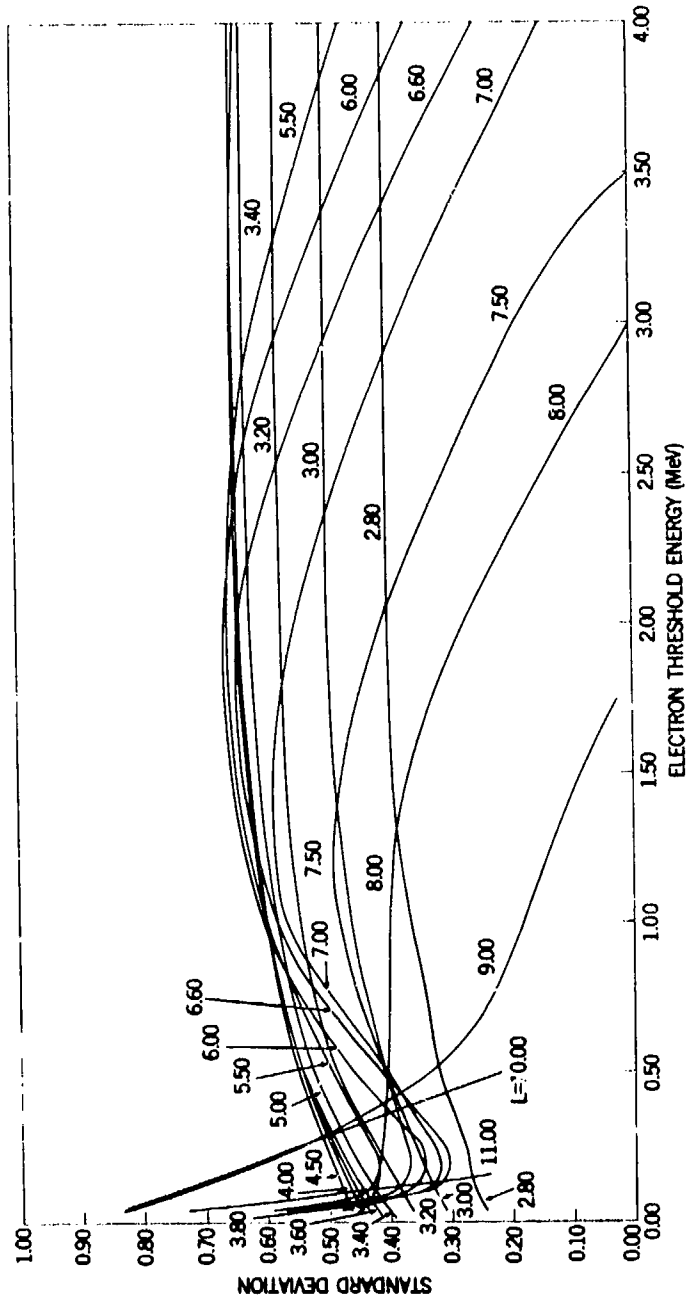


Figure 4-41. Model standard deviation of the AE 4 fluxes as a function of energy plotted for constant L (Reference 36).

4 January 1977

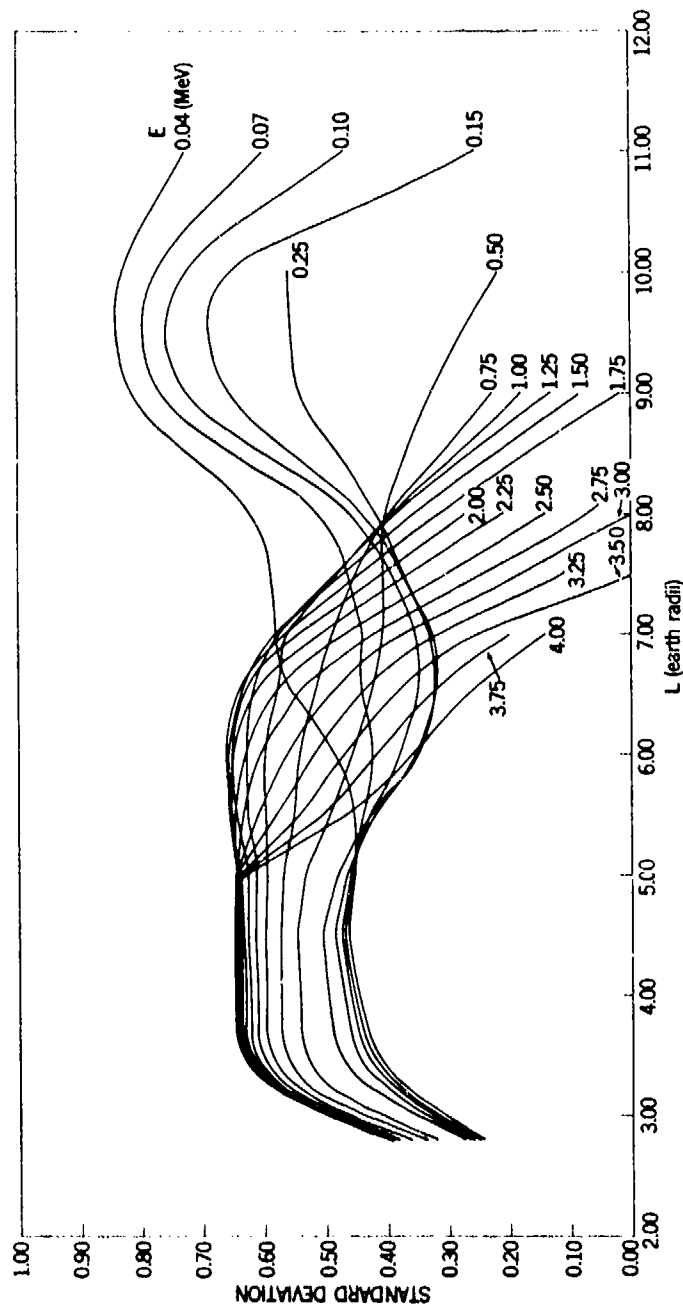


Figure 4-42. Model standard deviation of the AE 4 fluxes as a function of L plotted for constant energy (Reference 36).

4 January 1977

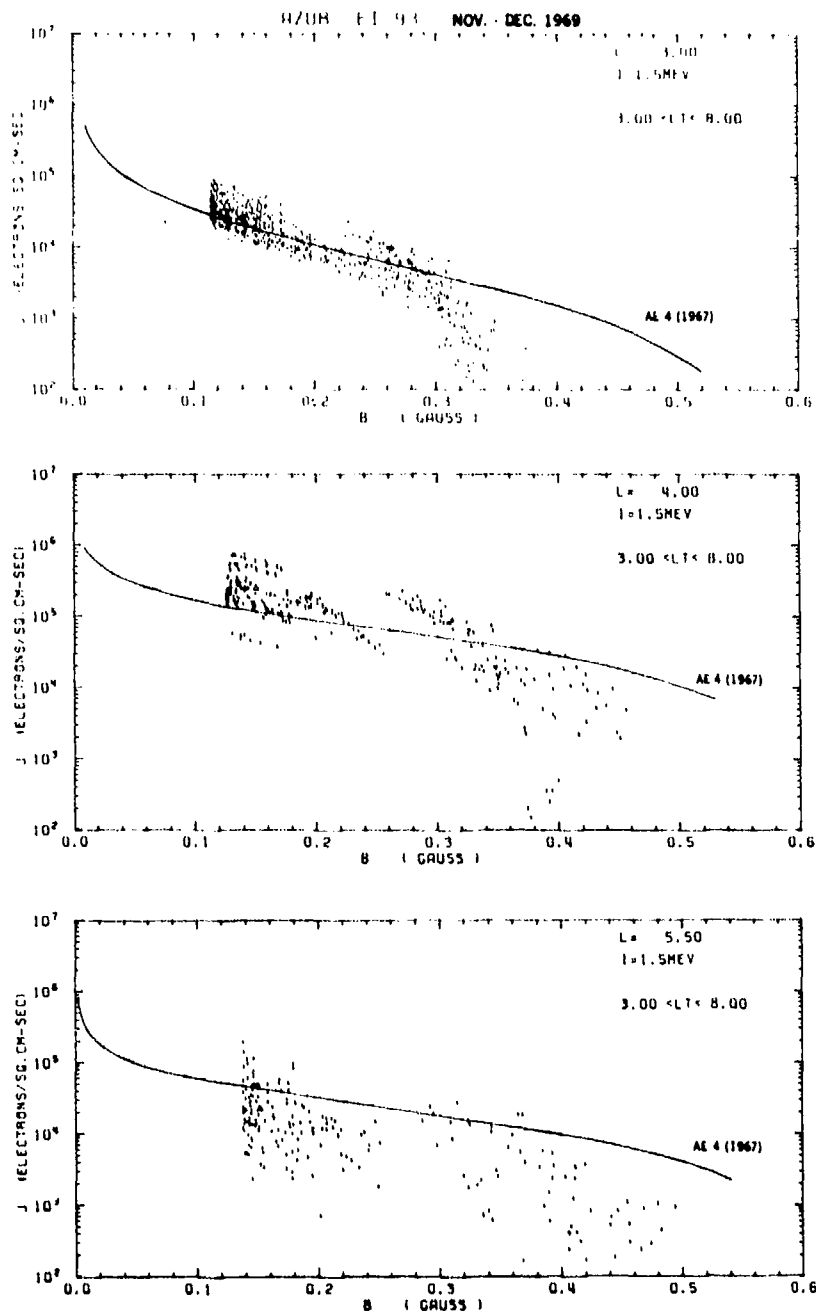


Figure 4-43. Comparison of AE 4 model B dependence with Azur data at $L = 3.0, 4.0, \text{ and } 5.5$.

4 January 1977

Comparison of AE 4 Electron Spectrum with Various Data at L = 6.6

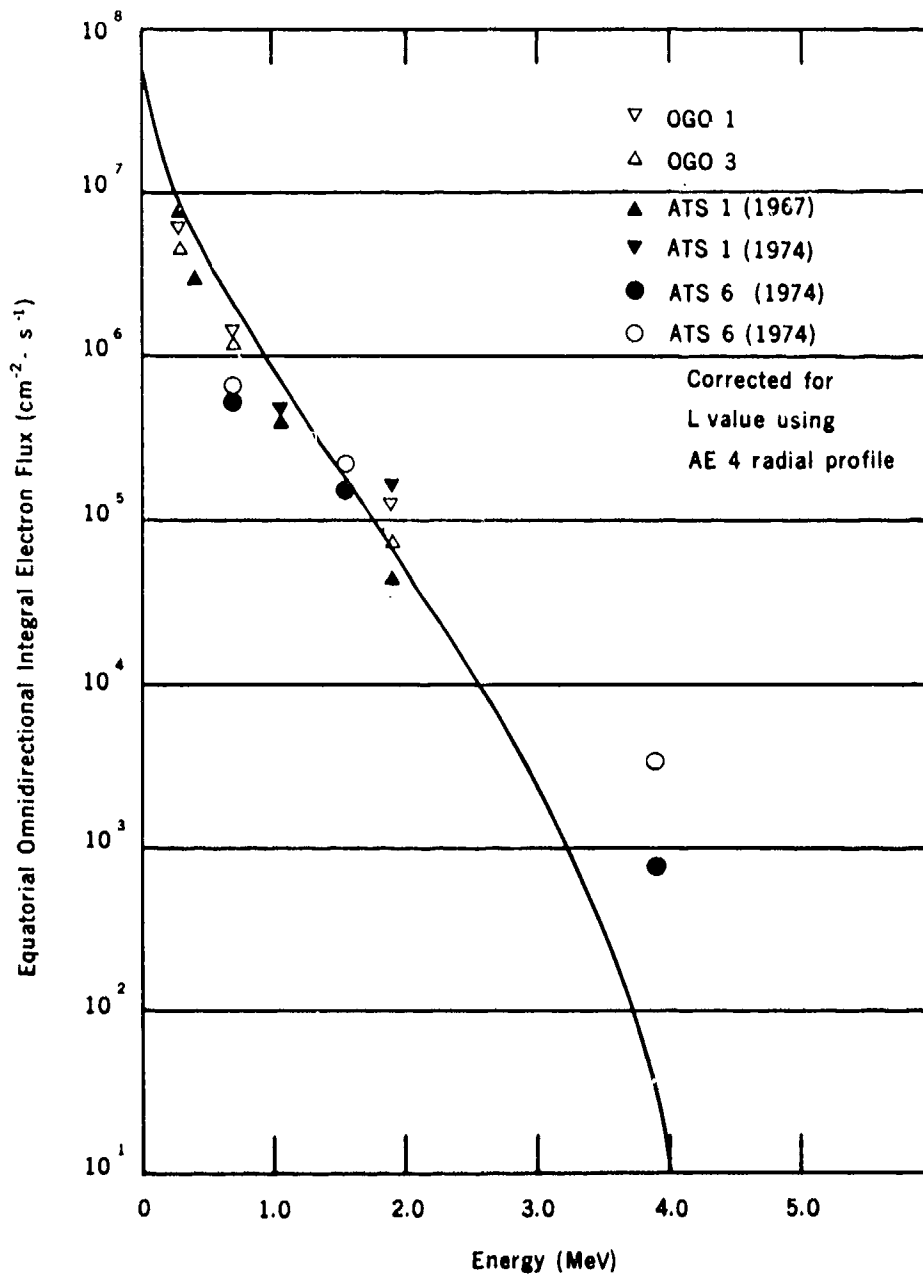


Figure 4-44. Comparison of AE 4 model electron spectrum with various data at L = 6.6.

4 January 1977

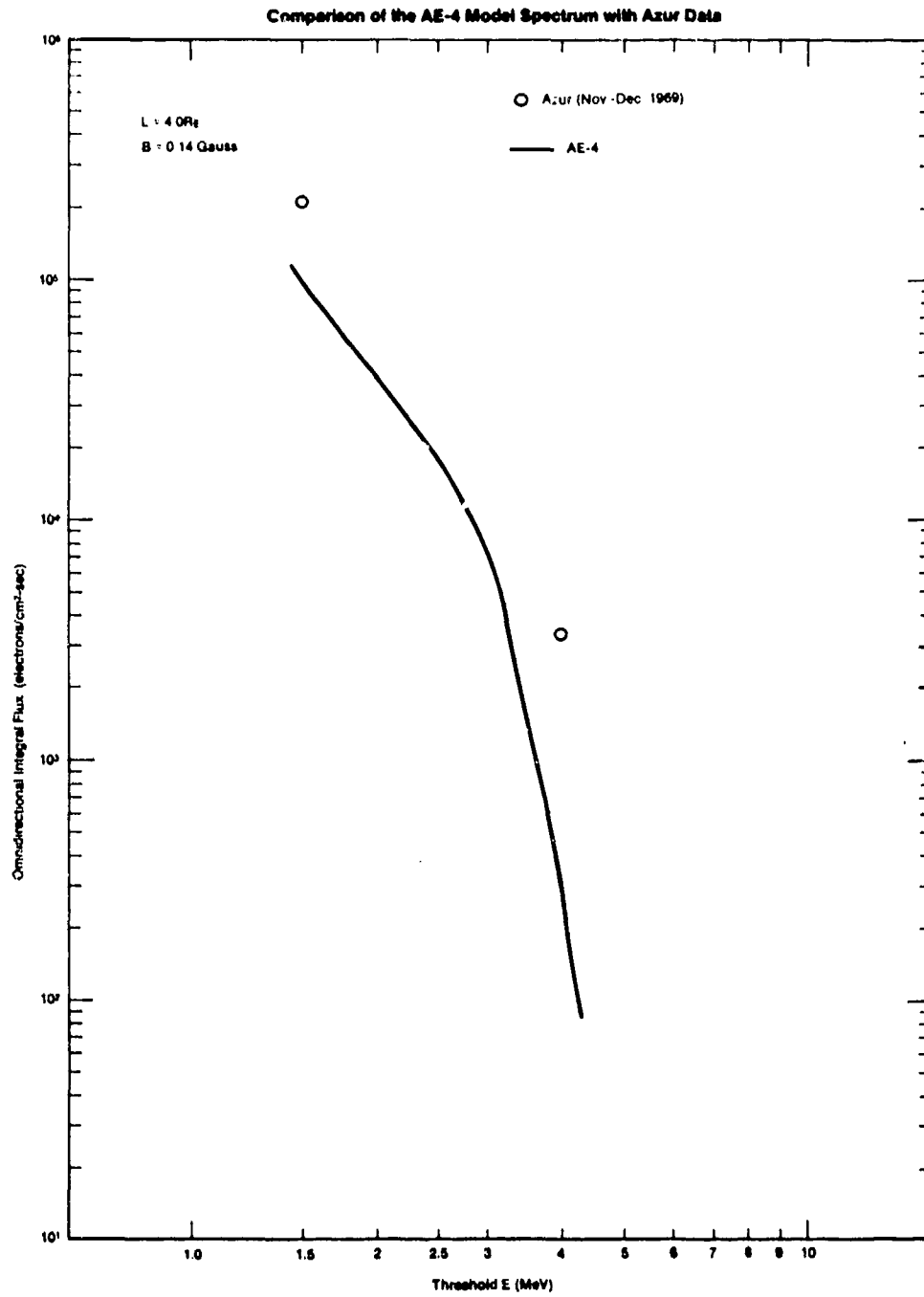


Figure 4-45. Comparison of AE 4 model spectrum with Azur data at L = 4.0 and B = 0.14 gauss.

4 January 1977

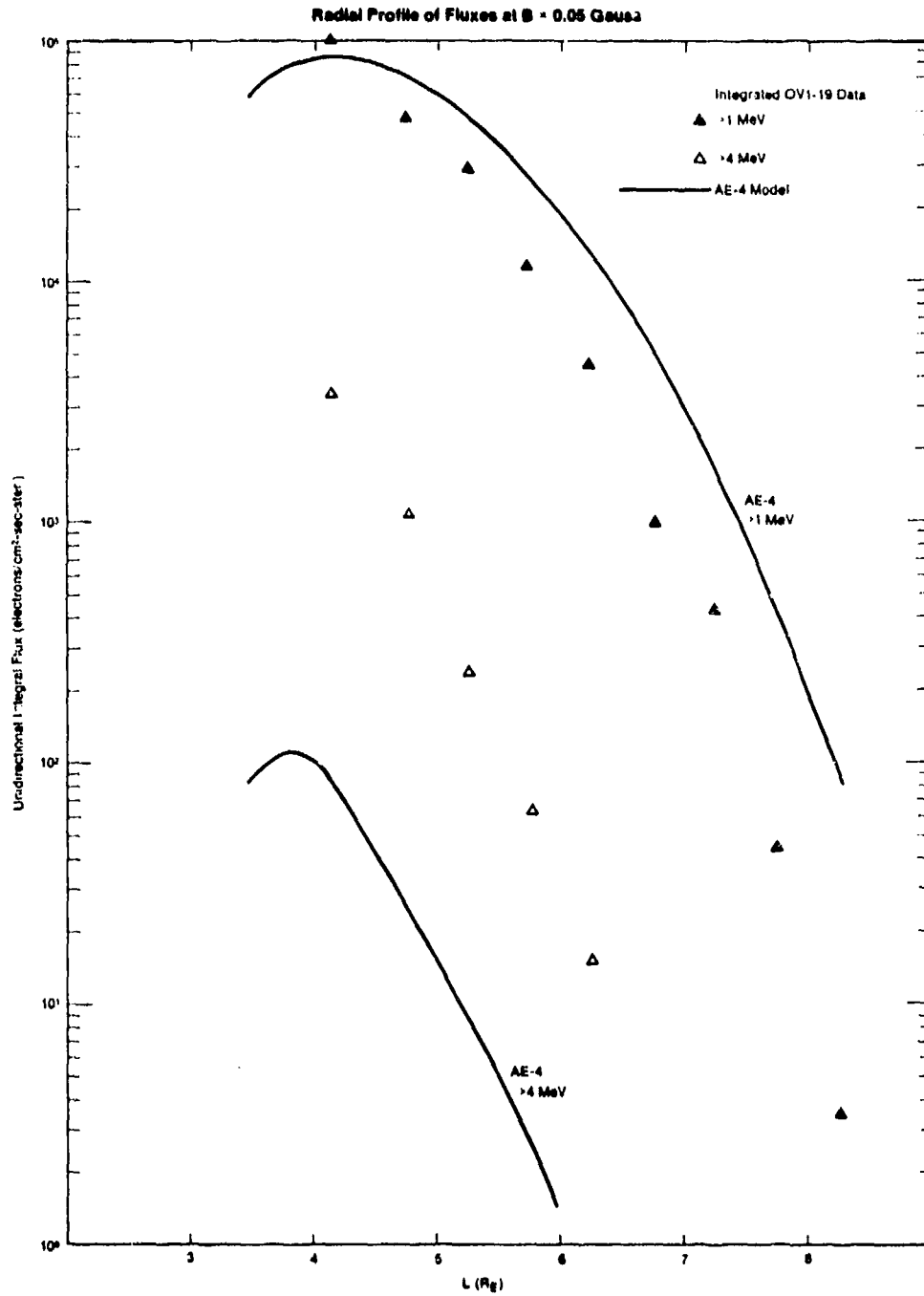


Figure 4-46. Comparison of AE 4 radial profile with OV1-19 data at $B = 0.05$ gauss.

4 January 1977

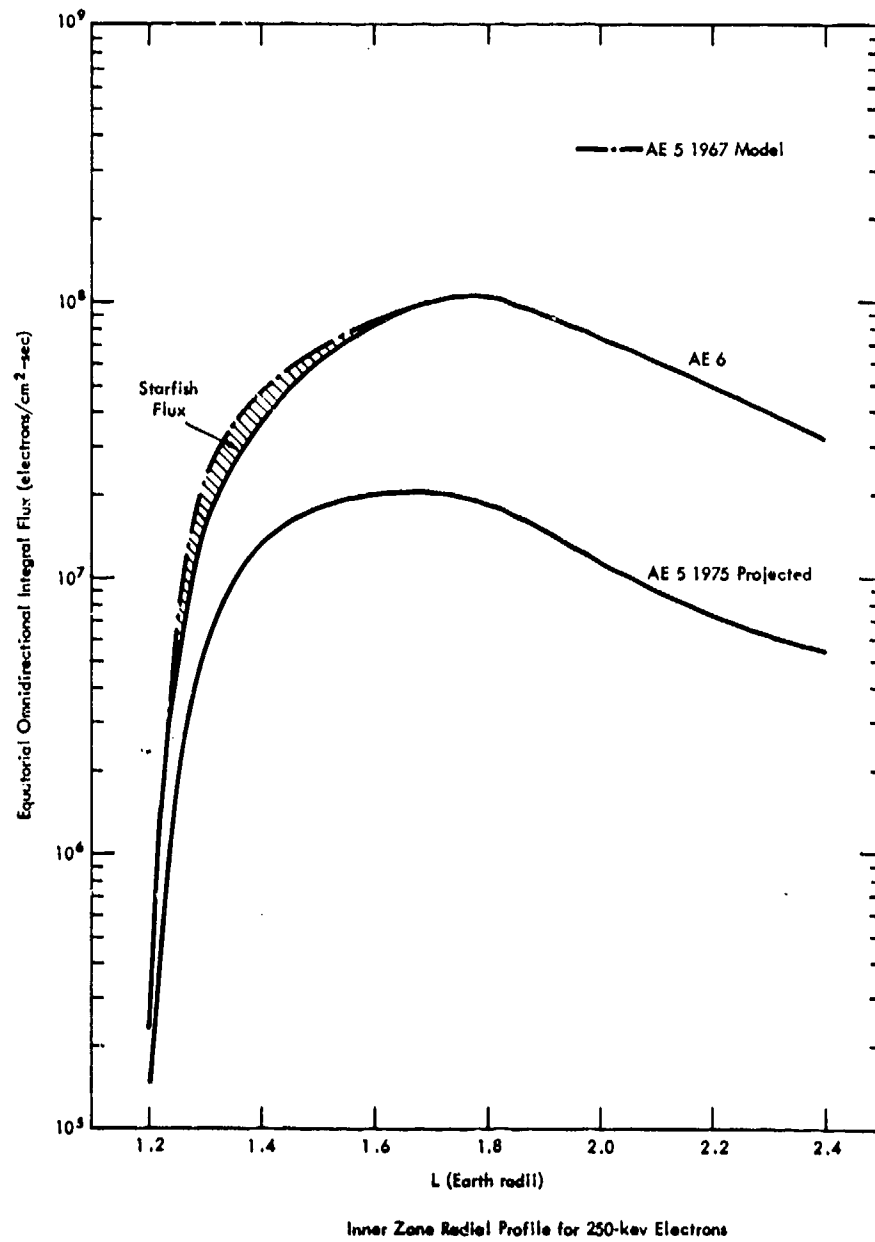


Figure 4-47. Model radial profiles for 250-KeV electrons in the inner zone. The difference between AE 6 and AE 5 (1975) is the solar-cycle effect. The difference between AE 6 and AE 5 (1967) is the Starfish electrons (Reference 42).

4 January 1977

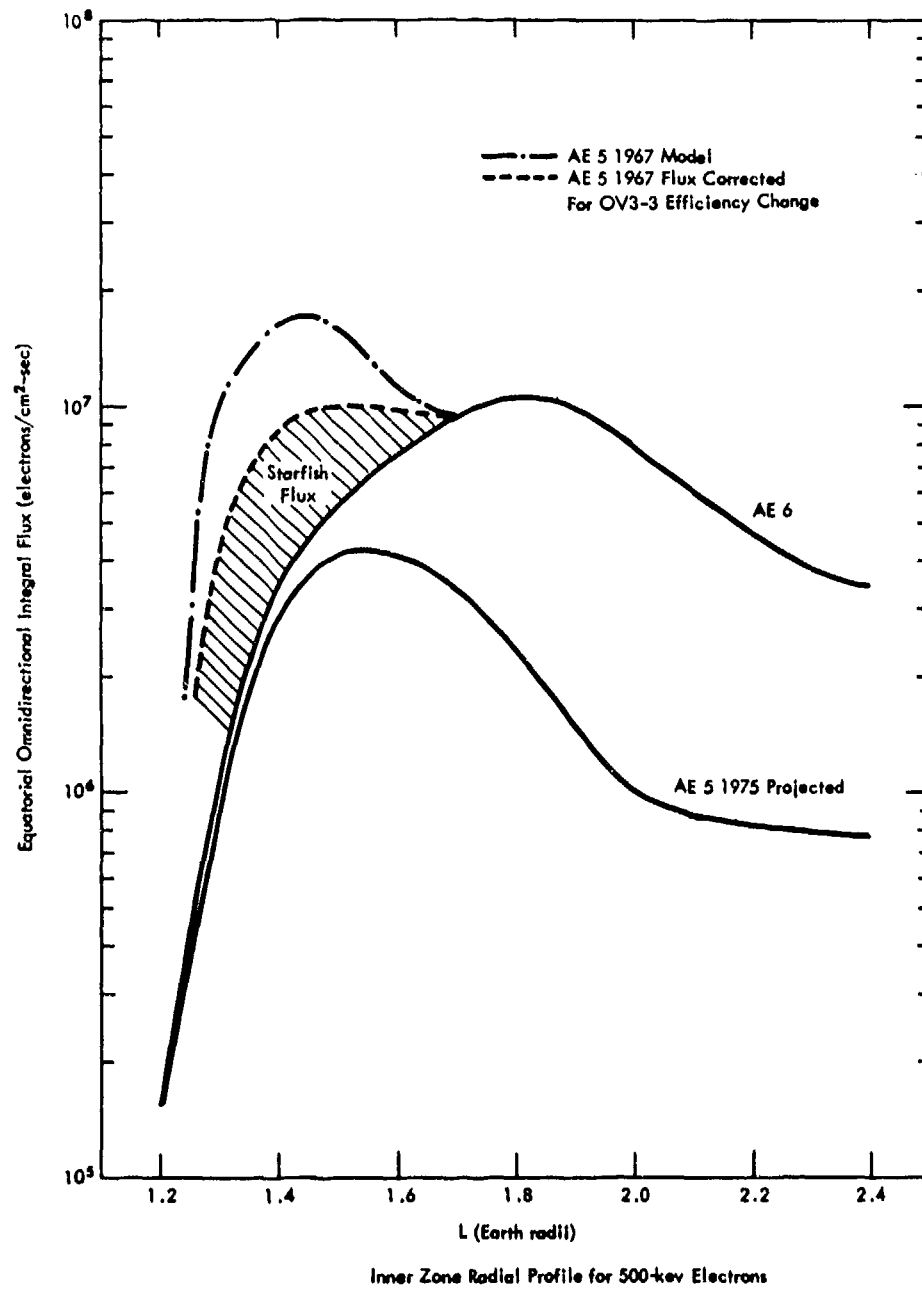


Figure 4-48. Model radial profiles for 500-KeV electrons in the inner zone (Reference 42).

4 January 1977

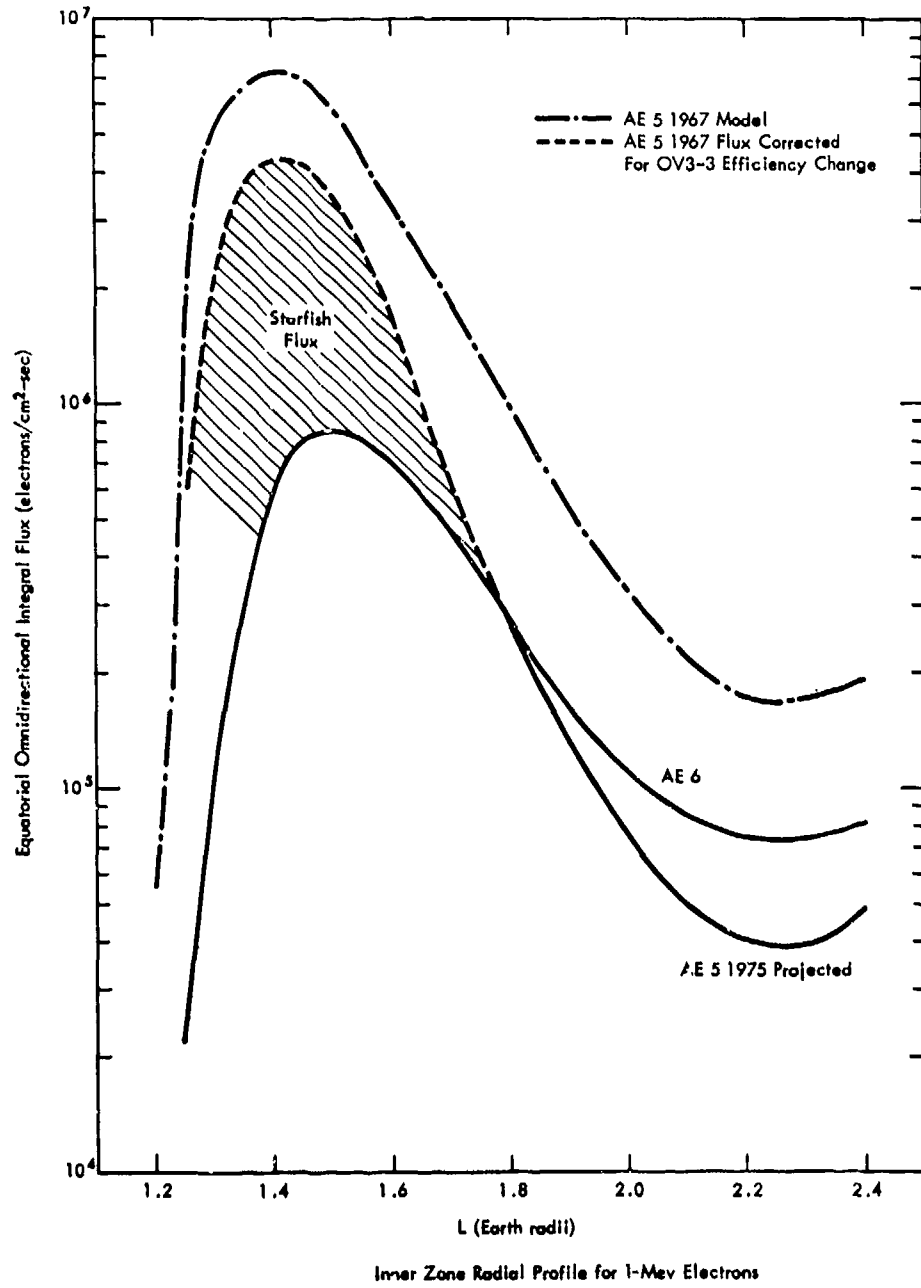


Figure 4-49. Model radial profiles for 1-MeV electrons in the inner zone (Reference 42).

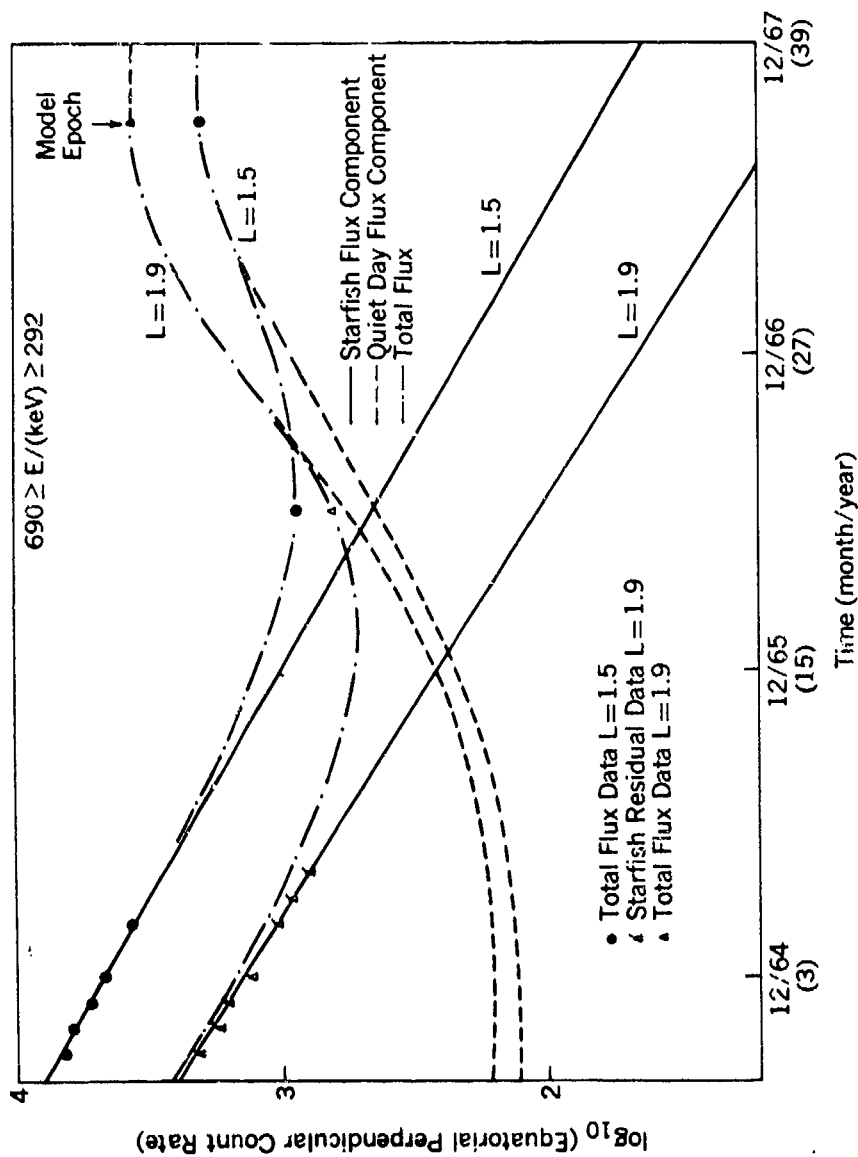


Figure 4-30. Relative importance of the Starfish and quiet-day flux components as a function of time for energy between 292 and 690 KeV at L = 1.5 and 1.9. The numbers in parentheses on the abscissa scale are months from solar minimum (Reference 43).

4 January 1977

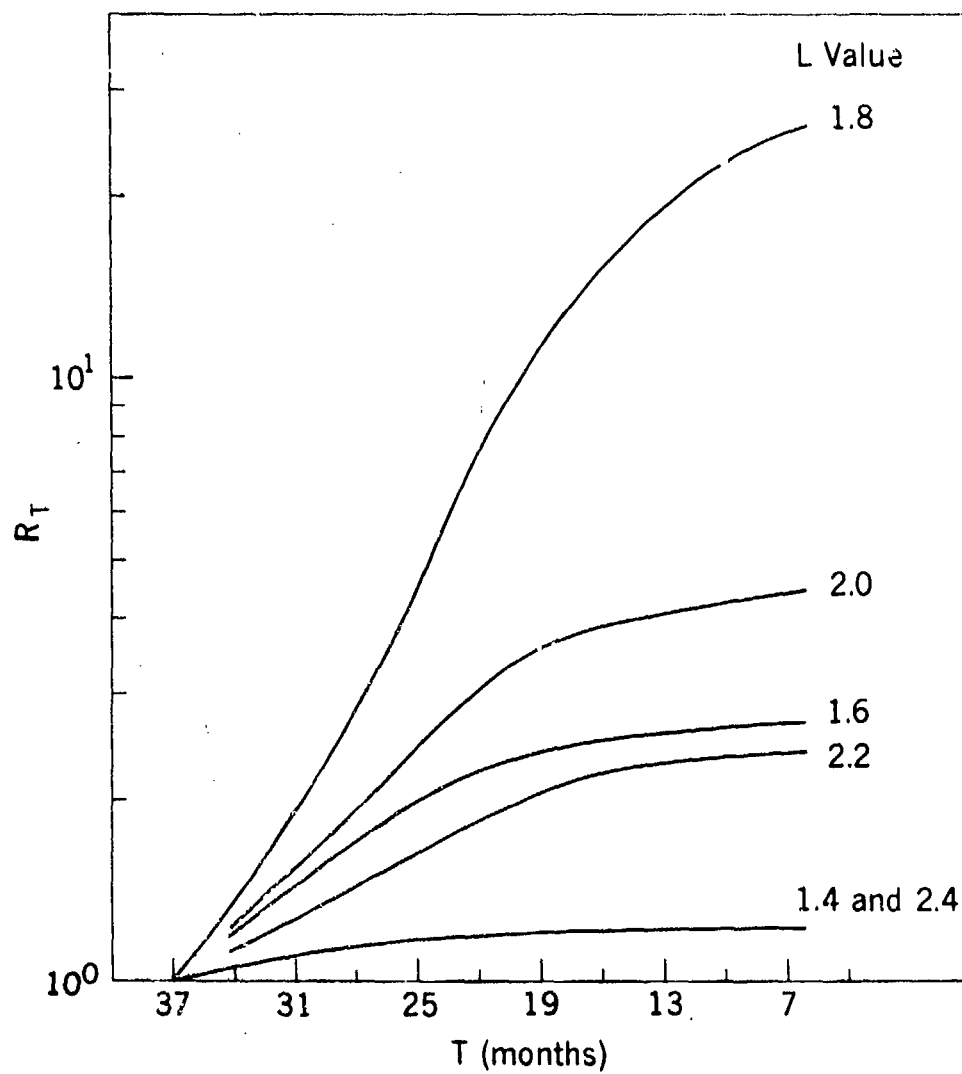


Figure 4-51. Ratio, R_T , of the integral flux ($E > 500$ KeV) in October 1967 to the corresponding flux in various phases of the solar cycle. T is the number of months counted from September 1964 (Reference 40).

4 January 1977

OMNIDIRECTIONAL INTEGRAL FLUX MAP
 500 KEV ELECTRONS L LE 2.4
 MODEL AE5 SOLAR MINIMUM PROJECTED

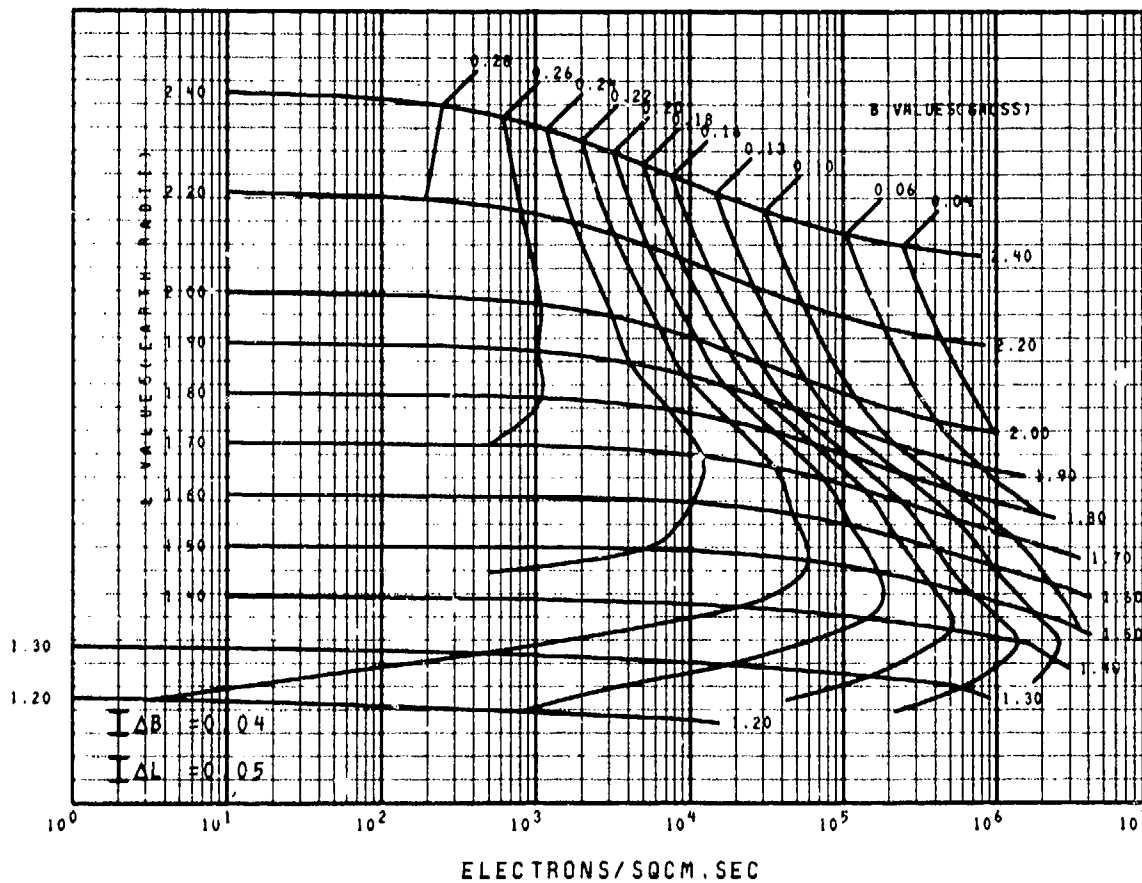


Figure 4-52. Nomograph map for AE 5 (1975) model fluxes of electrons with $E > 500$ KeV (Reference 40). This multidimensional nomograph presents the model flux as abscissa and the independent variables B and L as ordinates. Curves of constant B and L are plotted. The abscissa scale is shown as powers of 10 and the scale increments of the ordinate are given by ΔB (gauss) and ΔL (R_E) for B and L, respectively. The model flux for a given (B, L) point can be determined by the abscissa value of the intercept of the corresponding B-L curves. Interpolation of high accuracy can be obtained from the figure. Consult the source reference for details.

4 January 1977

OMNIDIRECTIONAL INTEGRAL FLUX MAP
500 KEV ELECTRONS FOR L LE 2.4
MODEL AE6 SOLAR MAXIMUM PROJECTED

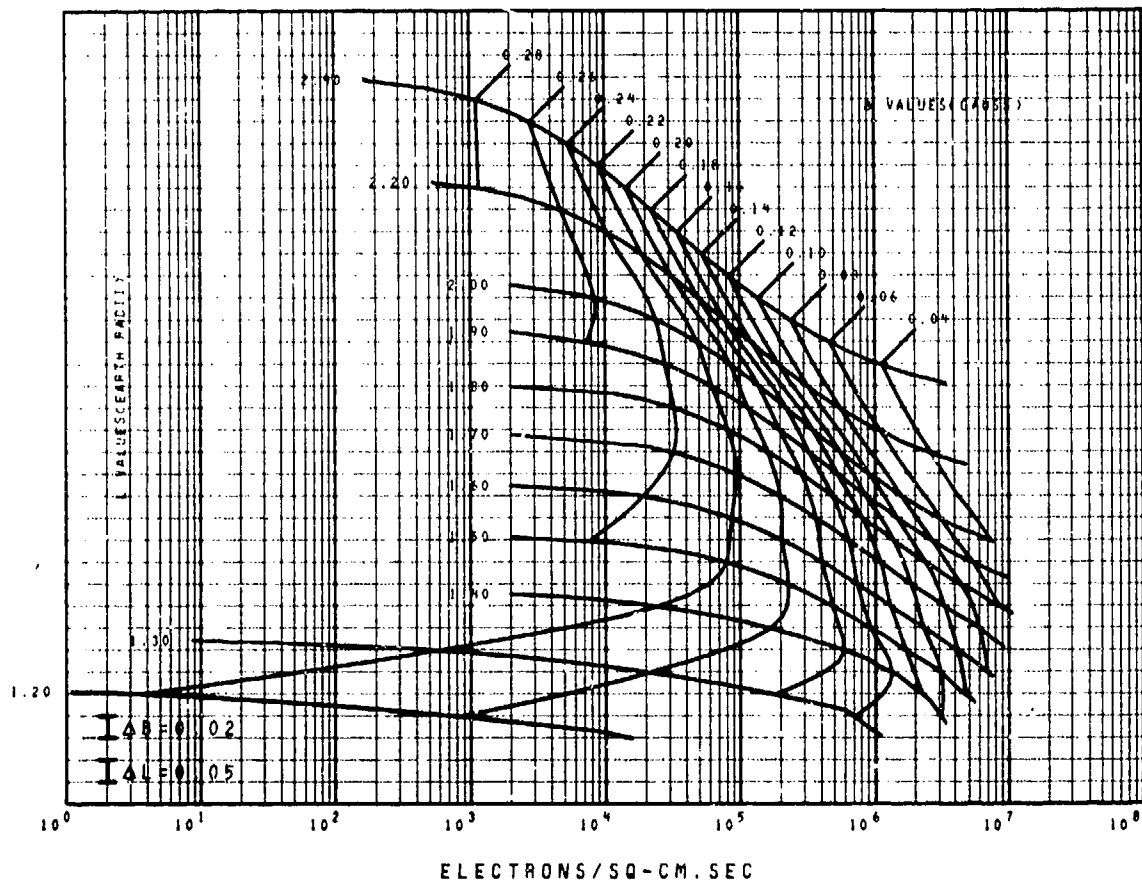


Figure 4-53. Nomograph map for AE 6 model fluxes of electrons with $E > 500$ KeV (Reference 42). This multidimensional nomograph presents the model flux as abscissa and the independent variables B and L as ordinates. Curves of constant B and L are plotted. The abscissa scale is shown as powers of 10 and the scale increments of the ordinate are given by ΔB (gauss) and ΔL (R_E) for B and L, respectively. The model flux for a given (B, L) point can be determined by the abscissa value of the intercept of the corresponding B-L curves. Interpolation of high accuracy can be obtained from the figure. Consult the source reference for details.

4 January 1977

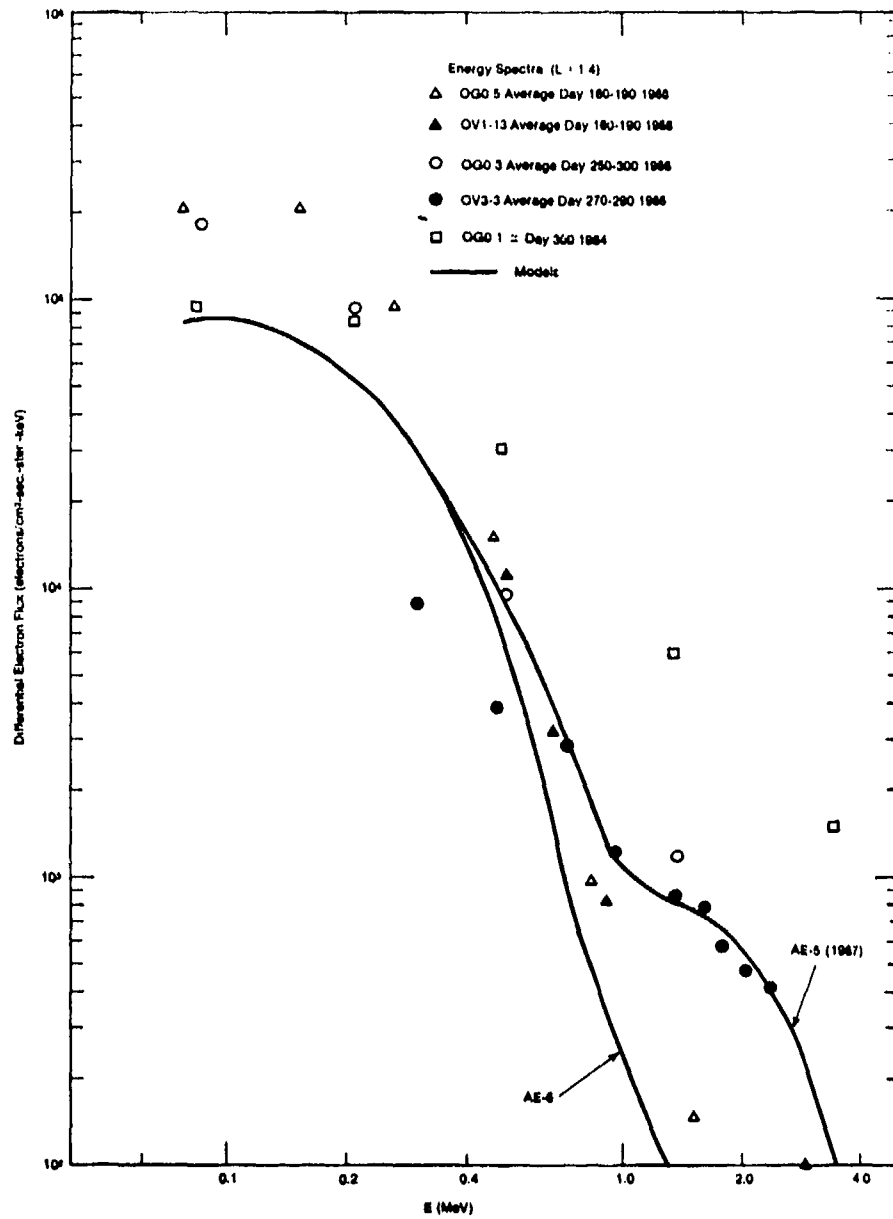


Figure 4-54. Comparison of inner zone model spectra with various data at L = 1.4 (Reference 80).

4 January 1977

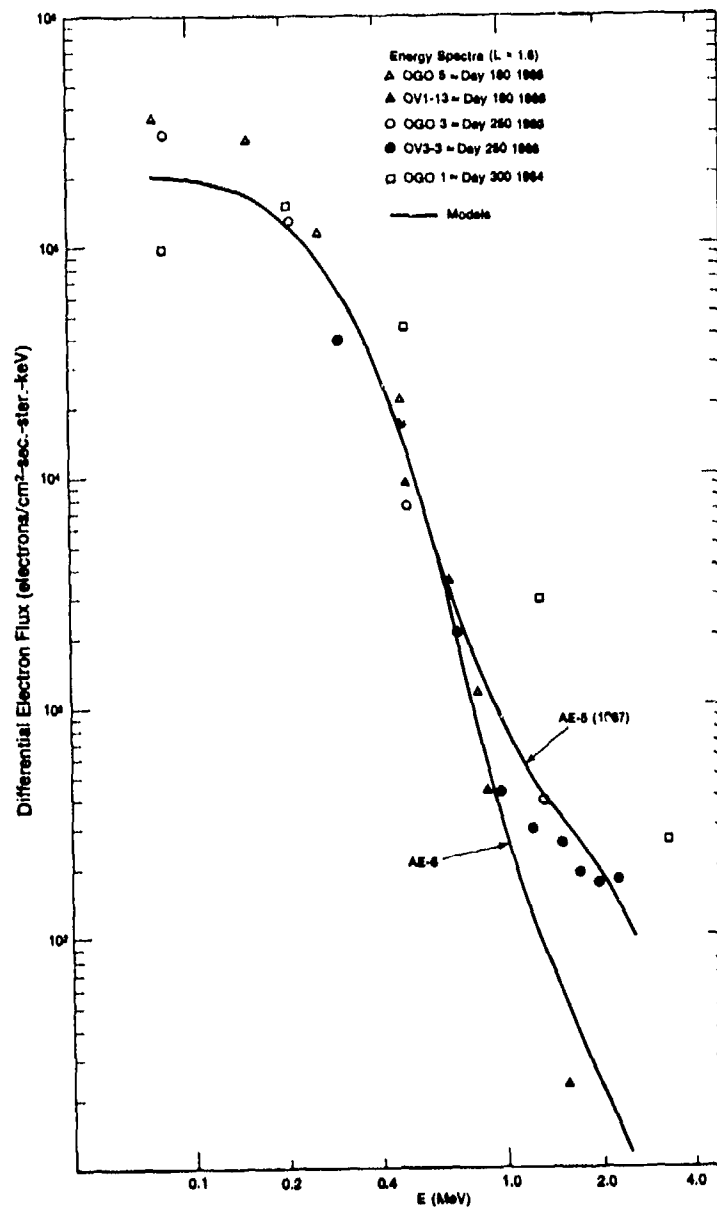


Figure 4-55. Comparison of inner zone model spectra with various data at L = 1.6 (Reference 80).

4 January 1977

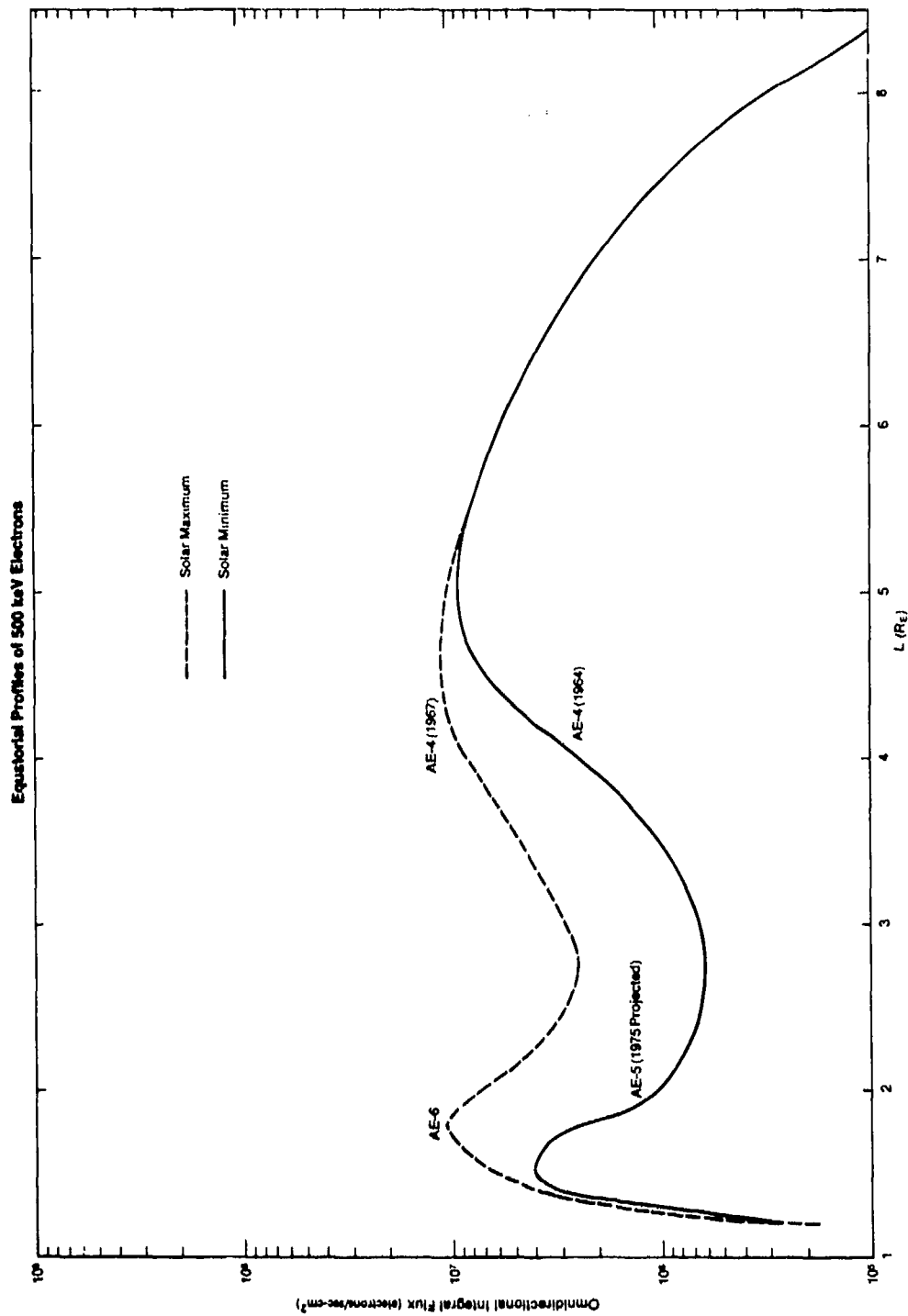


Figure 4-56. Composite equatorial radial profiles of the overall environment models for electrons with $E > 500$ KeV.

4 January 1977

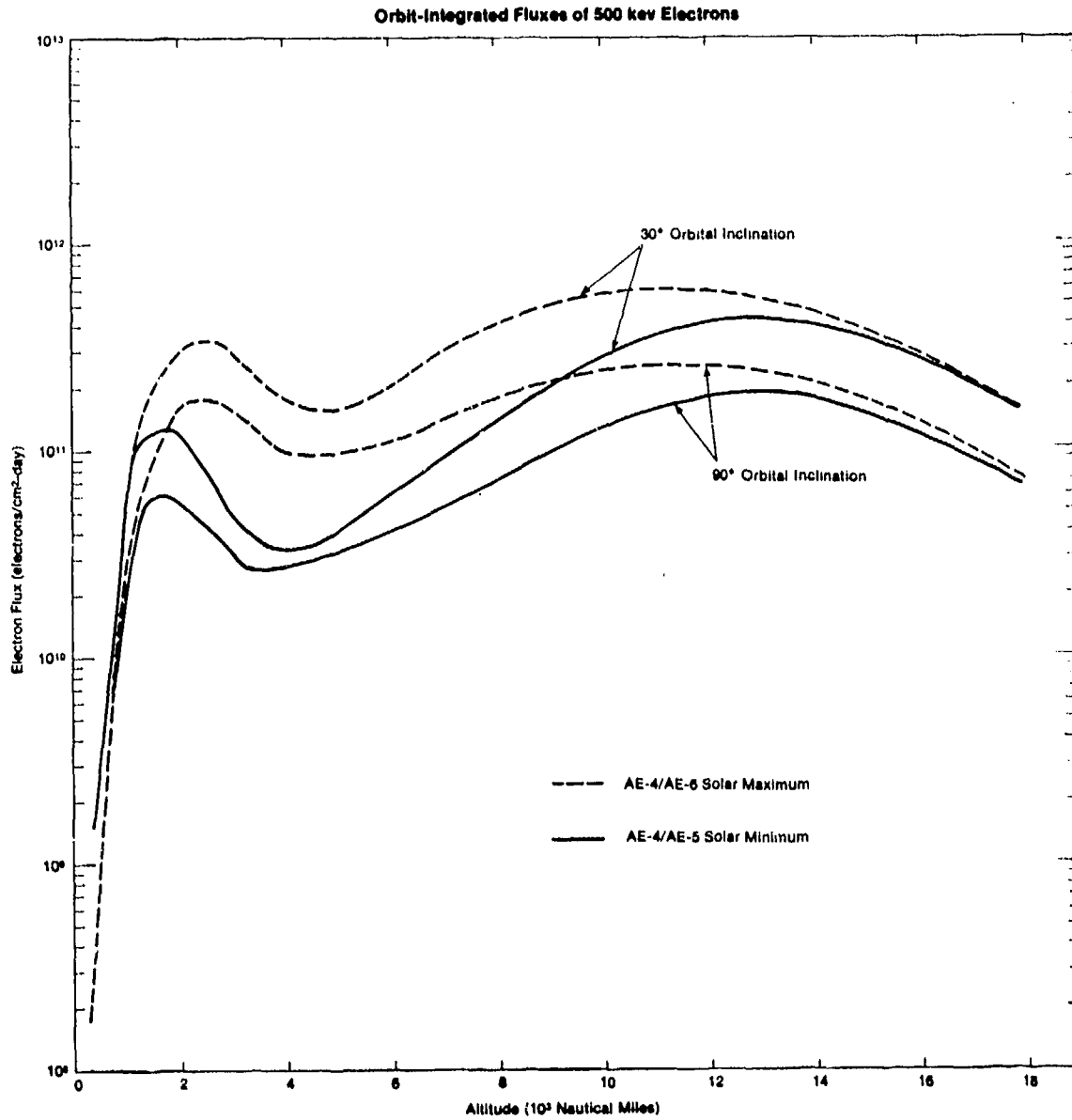


Figure 4-57. Orbit-integrated fluxes (1-day fluences) of >500 KeV electrons as a function of orbital altitude for inclinations of 30 and 90 degrees.

4 January 1977

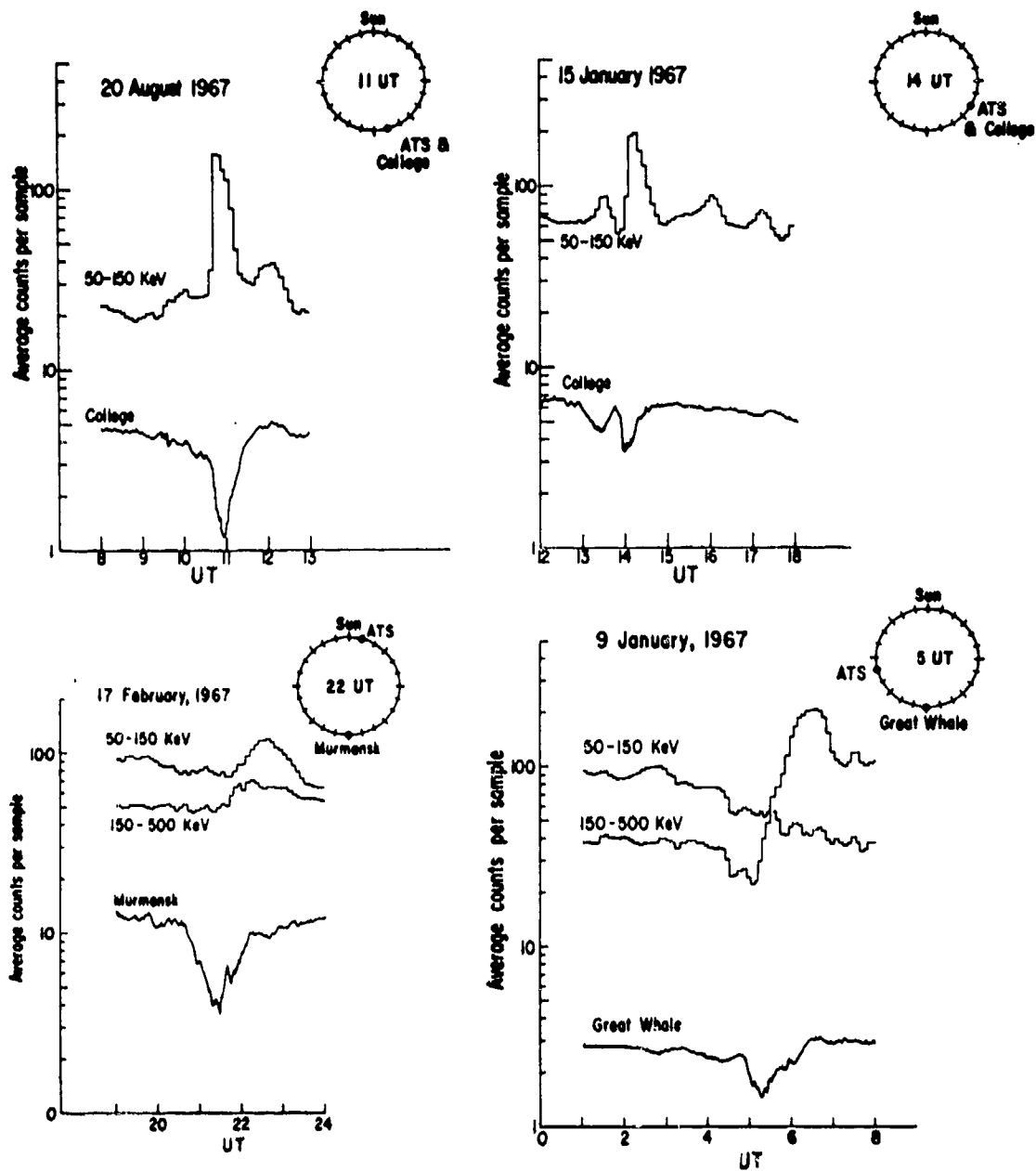


Figure 4-58. Particle substorm events observed by ATS 1 spectrometer. A linear amplitude trace of the correlated ground magnetogram is also presented for each event. The inset clock shows the local times of the spacecraft and the ground station pertaining to the event (Reference 44).

4 January 1977

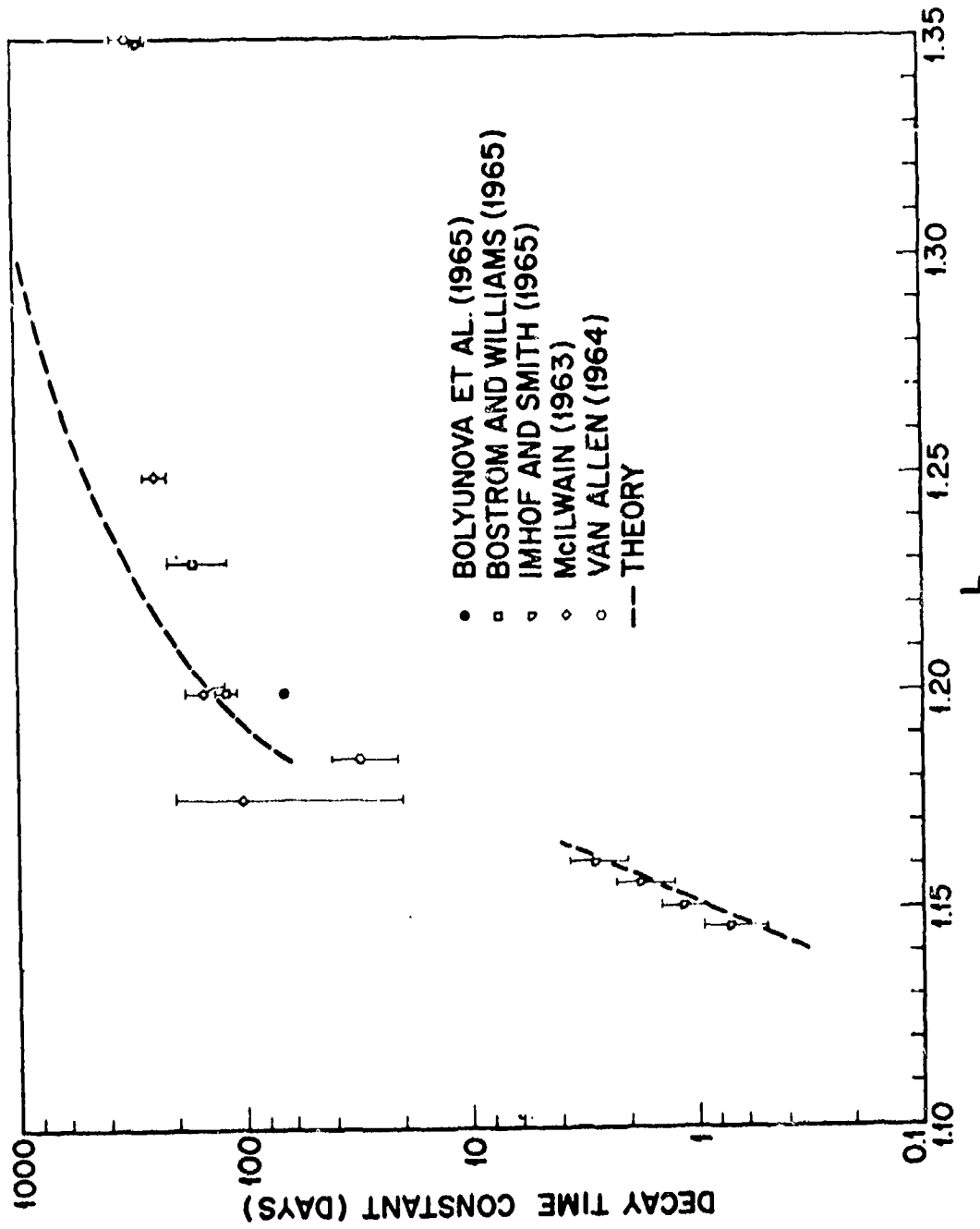


Figure 4-59. Comparison of the theoretical Coulomb-scattering loss with the measured decay time of electrons from 300 KeV to 5 MeV (Reference 46).

4 January 1977

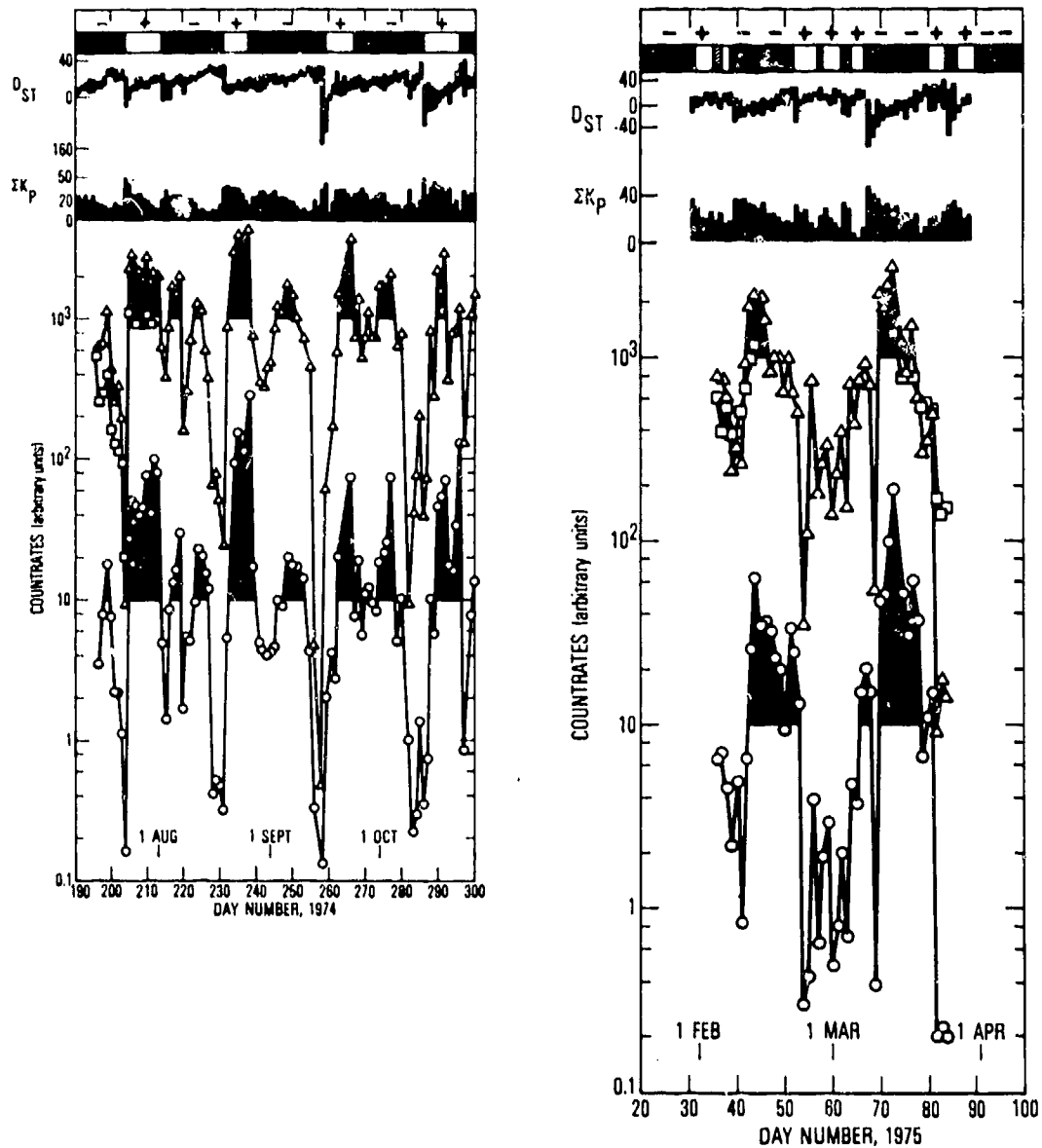


Figure 4-60. Hourly average of local noon electron count rates as observed by ATS 6 and ATS 1 in the autumn of 1974 and spring of 1975. Circles and triangles are ATS 6 data of >3.9 - and >1.6 -MeV electrons, respectively, and squares are ATS 1 data of >1.9 -MeV electrons. Flux enhancements are shaded for clarity. The correlation of the enhancements with the IMF sector structure is described in the text (Reference 49).

4 January 1977

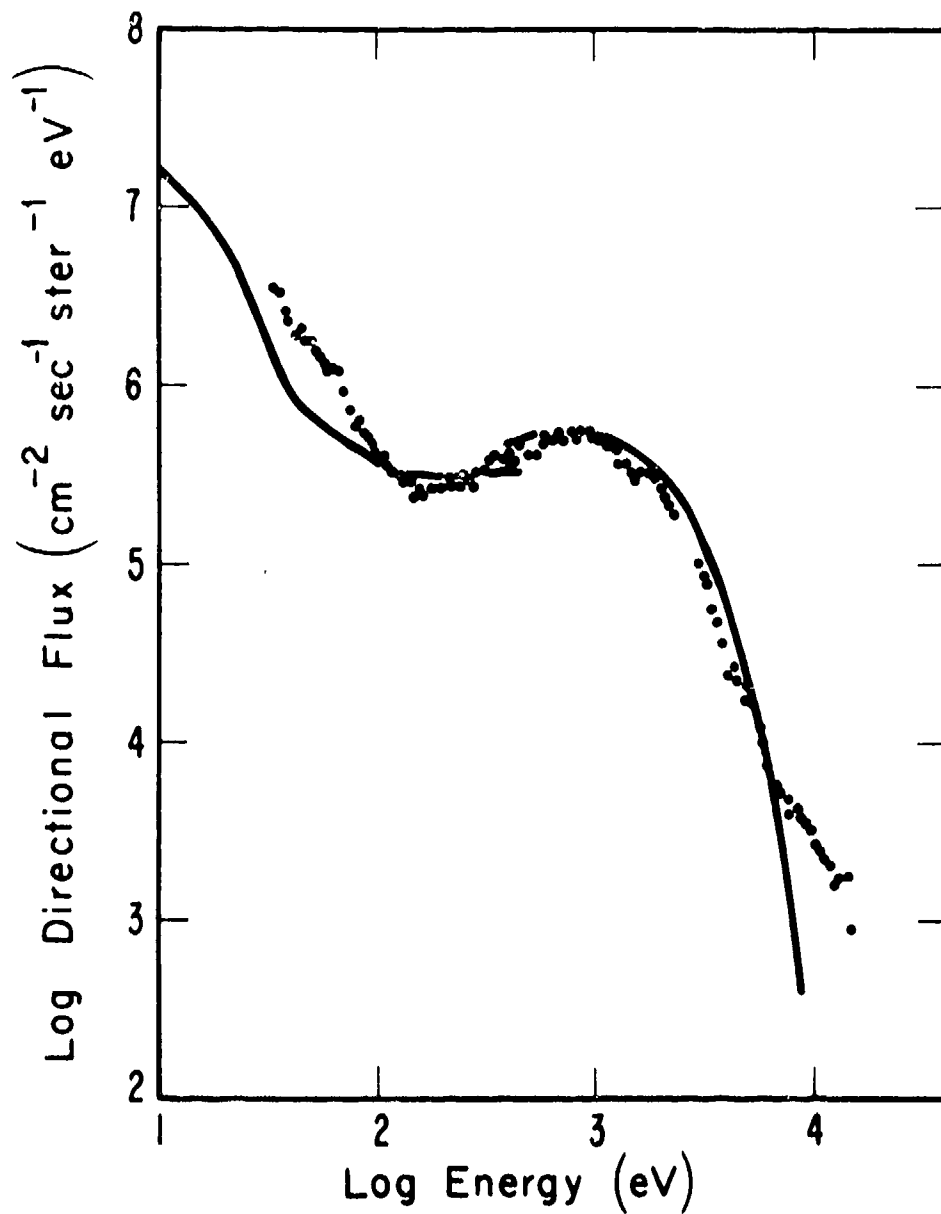


Figure 4-61. Comparison of the Injun 5 electron spectrum with the model spectrum computed by assuming a 400-volt potential difference along a magnetic field line and an ambient Maxwellian electron distribution of temperature of 800 eV and density of 5 cm⁻³ (Reference 51).

4 January 1977

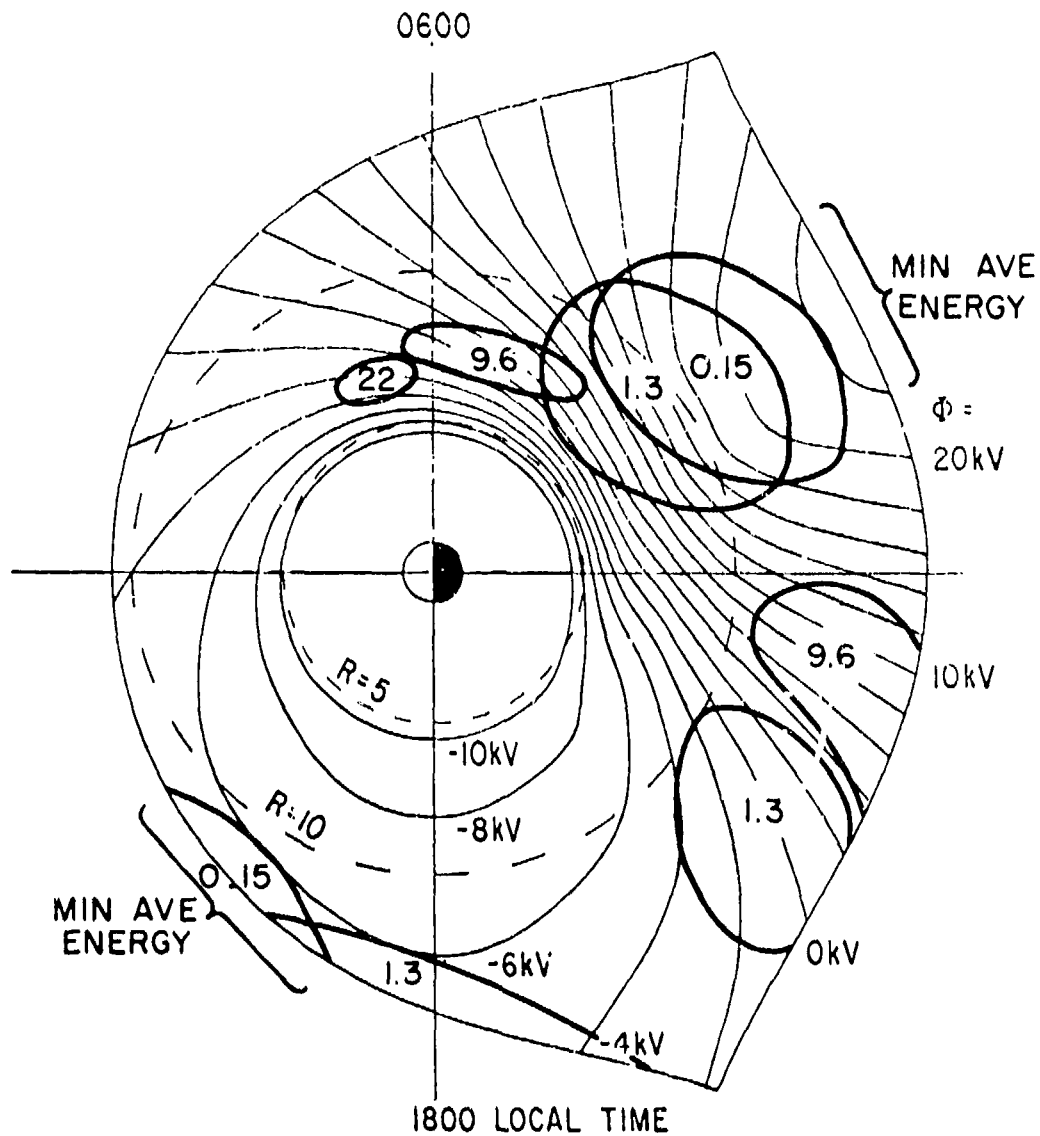


Figure 4-62. Composite map of low-energy electrons. Heavy lines give the locations of peak fluxes and energies projected onto the equatorial plane. The lighter lines present the electric potential pattern of McIlwain's model E3H (Reference 52).

4 January 1977

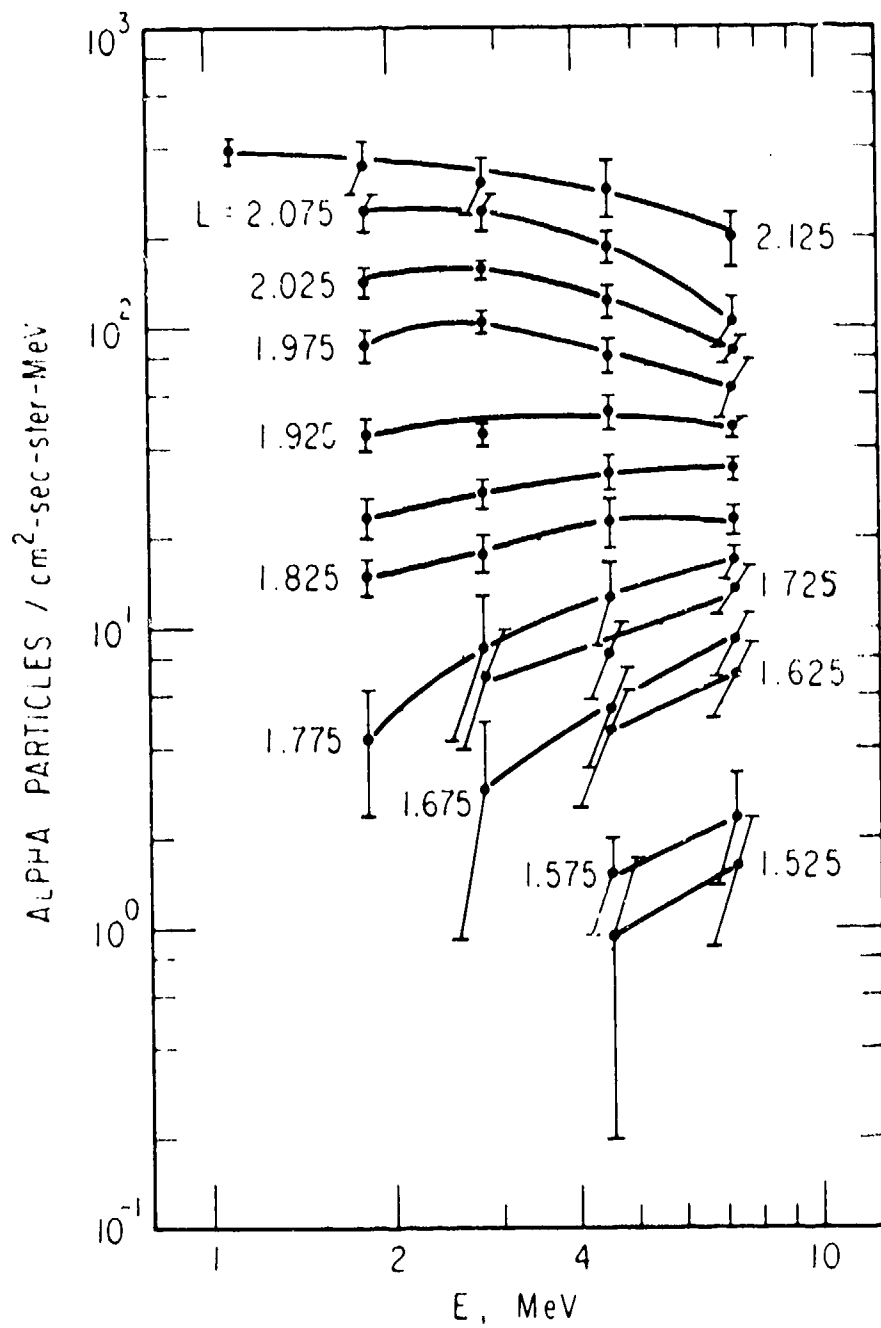


Figure 4-63. Differential energy spectra of alpha particles at selected L values between 1.525 and 2.125 plotted on the same intensity scale for $B/B_0 = 1.3$ (Reference 67).

4 January 1977

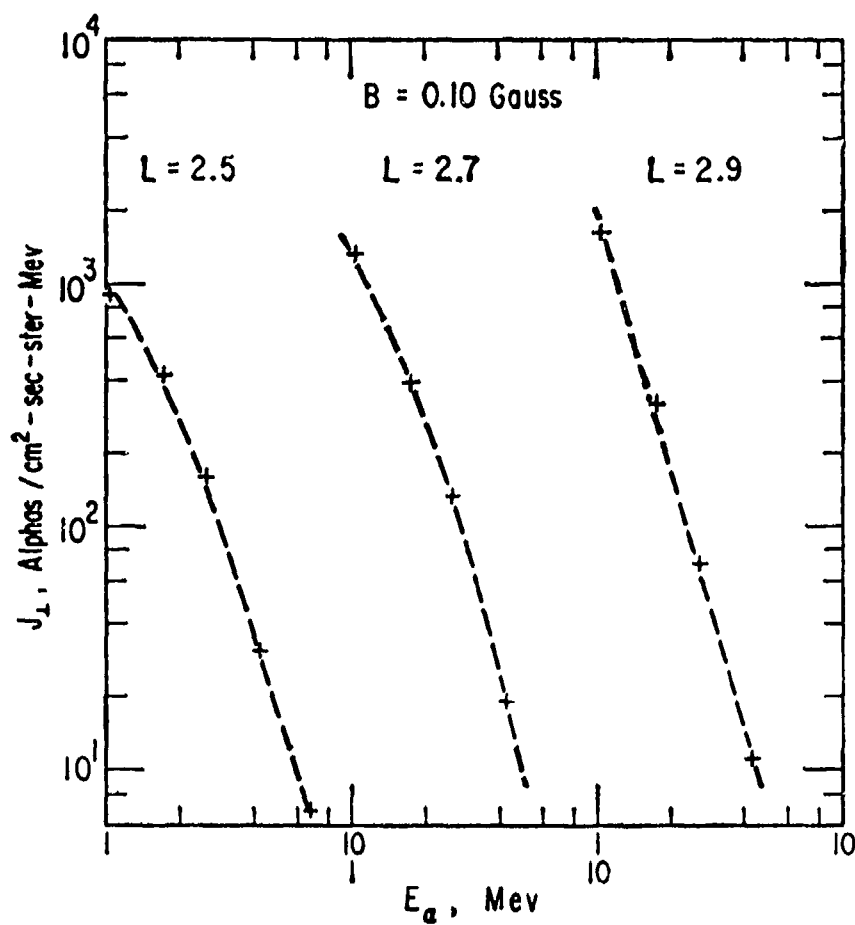


Figure 4-64. Alpha particle spectra (differential flux versus total energy) for B = 0.10 gauss and L = 2.5, 2.7, and 2.9 (Reference 57).

4 January 1977

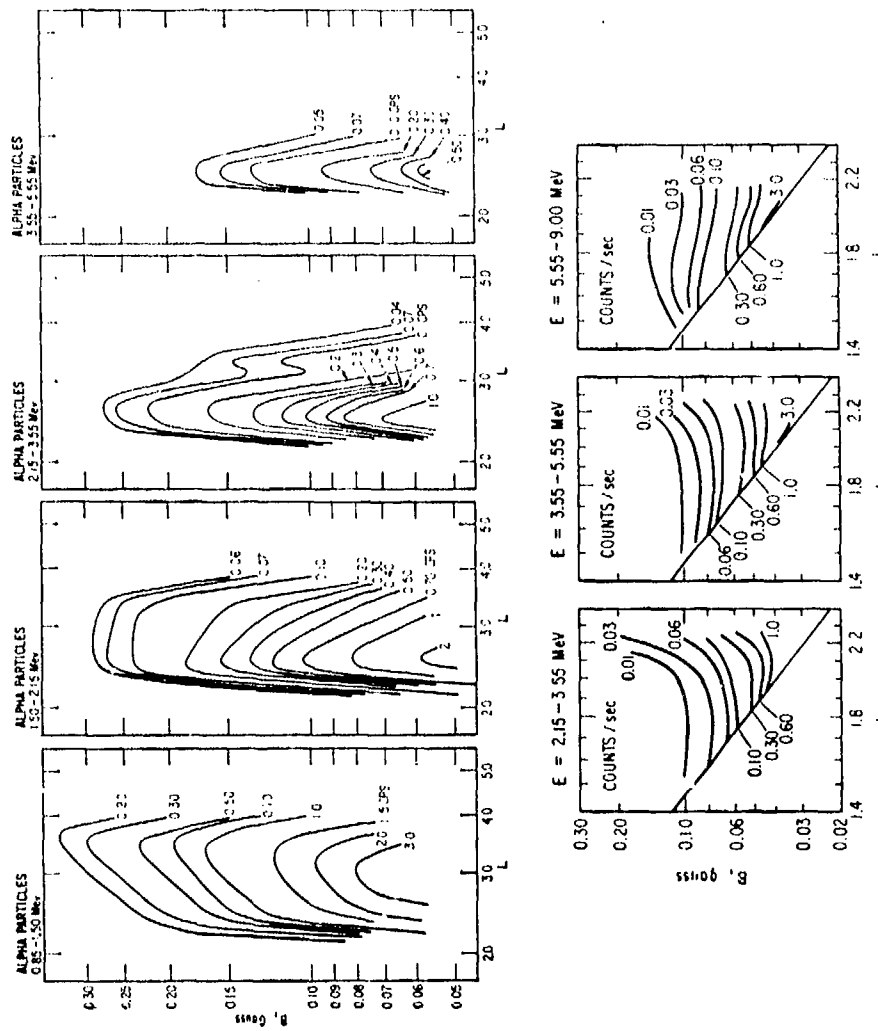


Figure 4-65. B-L plots of five alpha particle channels. The curves are labeled by counts per second. To convert to flux ($\text{cm}^{-2}\text{-sec}^{-1}$) in the respective energy passband, multiply by 470 for the 0.85- to 1.5-MeV channel, 380 for the 1.50- to 2.15-MeV channel, 425 for the 2.15- to 3.55-MeV channel, 375 for the 3.55- to 5.55-MeV channel, and 342 for the 5.55- to 9.0-MeV channel (Reference 67).

4 January 1977

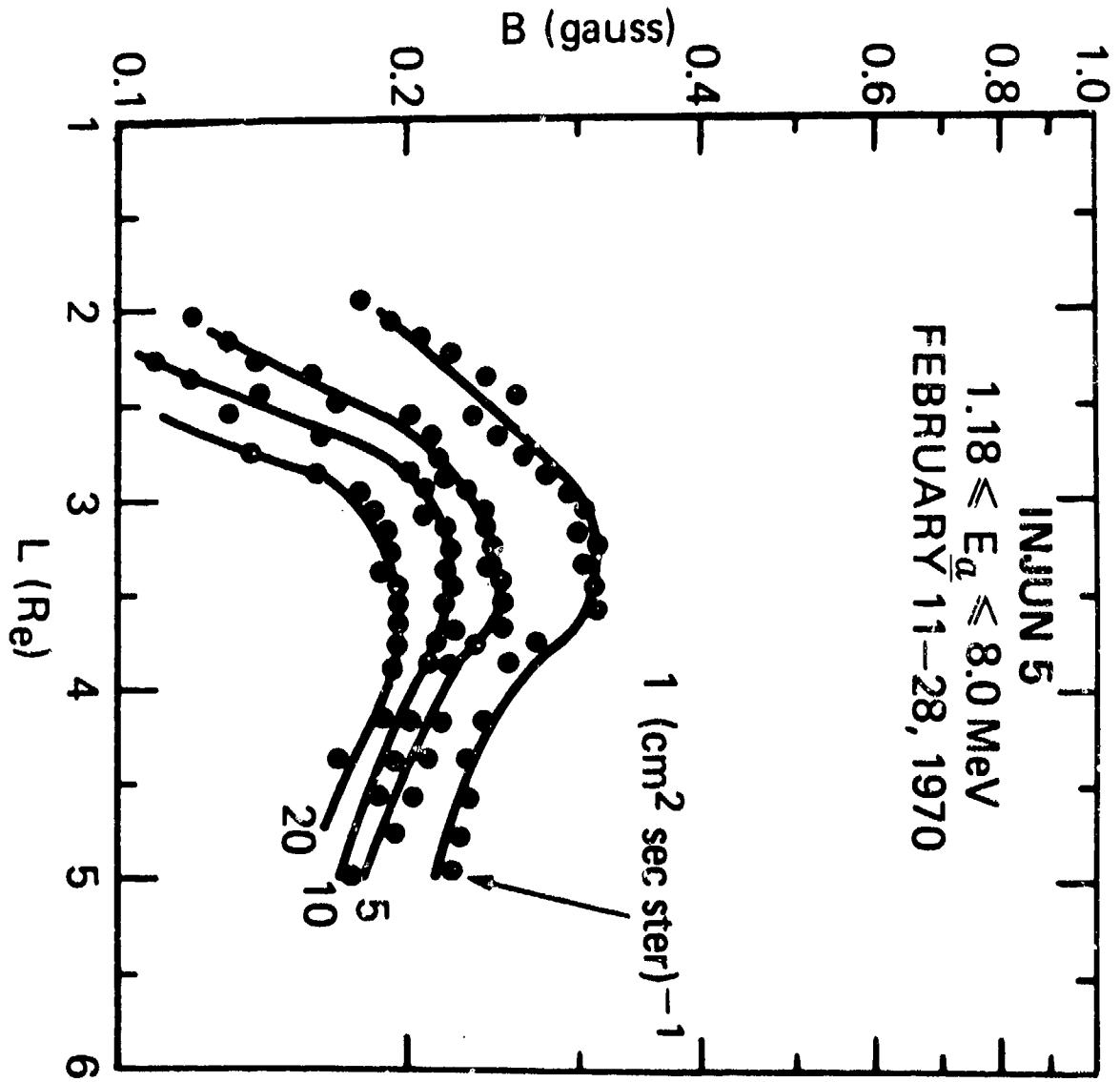


Figure 4-66. B-L contours of alpha particles with energies between 1.18 and 8.0 MeV from 11 through 28 February 1970 (Reference 60).

4 January 1977

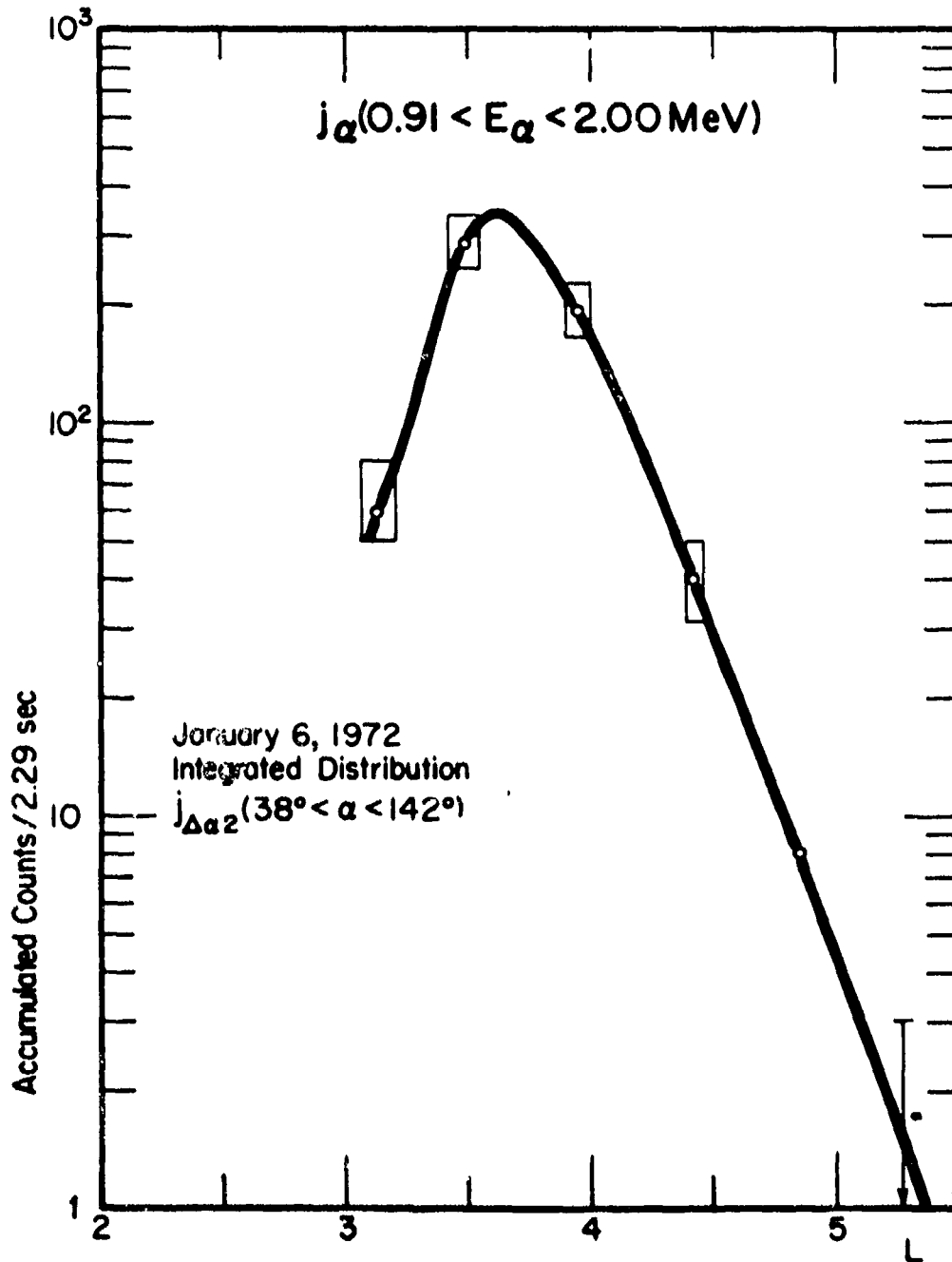


Figure 4-67. The radial profile of J_{α} ($0.91 < E_{\alpha} < 2.00$ MeV) inferred from the response of the $\Delta\alpha 2$ channel (Reference 59).

4 January 1977

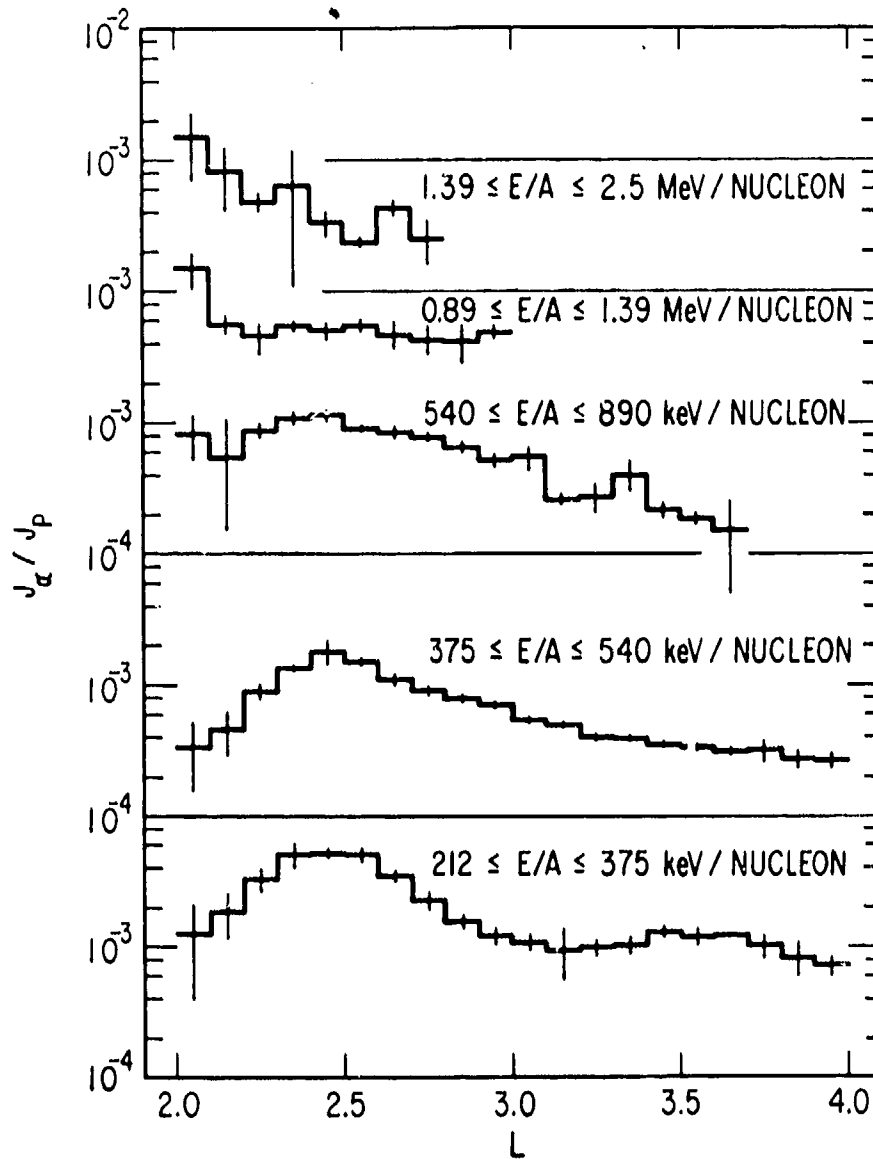


Figure 4-68. Average J_α/J_p versus L for five ranges of energy per nucleon (E/A). The ratios were obtained by averaging together the ratios from several values of B/B_0 at each L shell. The error bars represent the standard deviation of individual values from the average. E/A increases from the bottom frame to the top frame (Reference 58).

4 January 1977

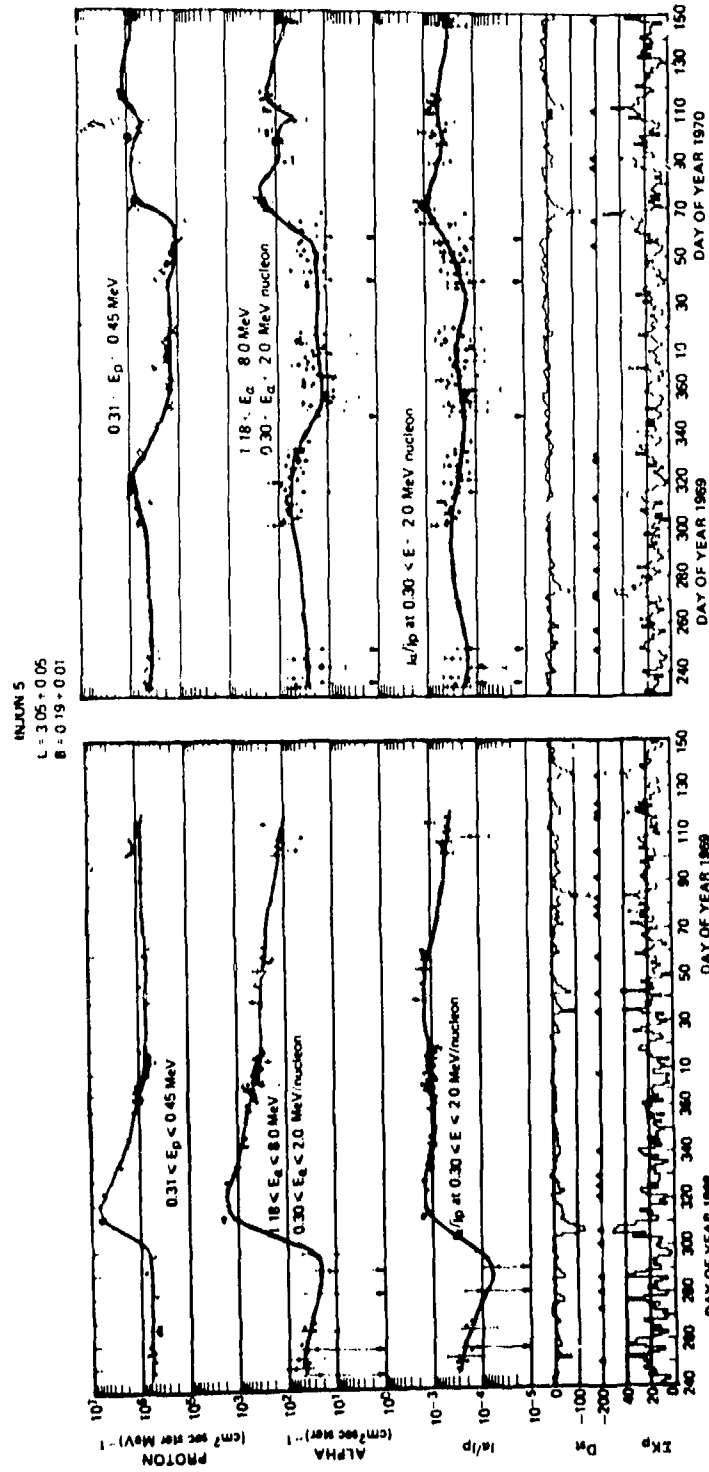


Figure 4-69. Daily averages of intensity for protons in the energy range of $0.31 \leq E_p \leq 0.45$ and alpha particles in the range of $0.30 \leq E_\alpha \leq 2.0$ MeV/nucleon, at $L = 3.05 \pm 0.05$ and $B = 0.19 \pm 0.01$ for the entire period for available Injun 5 data. Also shown are the J_α/J_p ratios, the daily-averaged Dst index, and the K_p daily sum (Reference 60).

4 January 1977

DISTRIBUTION LIST

DEPARTMENT OF DEFENSE

Director
Defense Advanced Research Proj. Agency
ATTN: LTC W. A. Whitaker
ATTN: Dir. Tac. Tech. Ofc., Robert A. Moore
ATTN: STO, Captain J. Justice
ATTN: NMO, Eric Willis
ATTN: Major Gregory Canavan

Defense Communication Engineer Center
2 cy ATTN: Code R103S
ATTN: Code 720, John Worthington
ATTN: Code 103, J. Raffensberger
ATTN: Code 103R, D. T. Worthington
ATTN: Code 700, J. Lebo

Director
Defense Communications Agency
ATTN: W. Heidig
ATTN: Code 810, R. W. Rostrom

Defense Documentation Center
Cameron Station
12 cy ATTN: TC

Director
Defense Intelligence Agency
ATTN: DT-1, Mr. Knoll
ATTN: DT-1C

Director
Defense Nuclear Agency
ATTN: STVL, F. Lavier
ATTN: RAEV, Harold C. Fitz, Jr.
ATTN: RAAE, Major John Clark
3 cy ATTN: RAAE, Charles A. Blank
3 cy ATTN: TITL, Tech. Library
ATTN: ULIS
ATTN: STRA
ATTN: RAEV
ATTN: TISI, Archives
ATTN: RAAE, Major Mueller
ATTN: RATN

Dir. of Defense Resch. & Engineering
Department of Defense
ATTN: S6SS (OS)

Commander
Field Command
Defense Nuclear Agency
ATTN: FCT
ATTN: FCT, William S. Isengard

Director
Interservice Nuclear Weapons School
ATTN: Document Control

Director
Joint Strat. Target Planning Staff, JCS
ATTN: JPST, Major J. S. Green
ATTN: Doc. Control

DEPARTMENT OF DEFENSE (Continued)

Chief
Livermore Division, Field Command, DNA
Lawrence Livermore Laboratory
ATTN: FCPRL

Director
National Security Agency
ATTN: Technical Library

Chairman
Office of Joint Chiefs of Staff
ATTN: J-3, Environmental Services Div.

OJCS/J-3
ATTN: J-3, Environmental Services Div.
ATTN: J-3, Operations
ATTN: WWCSS, Eval. Ofc., Mr. Toma

OJCS/J-6
ATTN: J-6
ATTN: J-6, Plans & Policy R & D Div.

DEPARTMENT OF THE ARMY

Commander/Director
Atmospheric Sciences Laboratory
US Army Electronics Command
ATTN: Robert Rubio
ATTN: R. Olsen
ATTN: E. Butterfield, DRSEL-BL-SY-R
ATTN: F. E. Niles, DRSEL-BL-SY-S
ATTN: H. Ballard

Director
BMD Advanced Tech. Center
Huntsville Office
ATTN: ATC-0, W. Davies

Program Manager
BMD Program Office
ATTN: Plans Division

Commander
BMD System Command
ATTN: BDMSC-TEN, Noah J. Hurst

Dep. Chief of Staff for Resch. Dev. & Acq.
Department of the Army
ATTN: CRD-NCB
ATTN: NCB Division
ATTN: ABMDA-00

Chief of Engineers
Department of the Army
ATTN: Fernand DePercin

Deputy Chief of Staff for Ops. & Plans
Department of the Army
ATTN: Dir. of Chem. & Nuc. Ops.
ATTN: DAMO-BDC, Colonel David W. Einsel

PRECEDING PAGE BLANK-NOT FILLED

D-1

4 January 1977

DEPARTMENT OF THE ARMY (Continued)

Commander
Harry Diamond Laboratories
2 cy ATTN: DRXDO-NP
ATTN: Chief, Nuc. Vulnerability Br.

Director
US Army Ballistic Research Labs.
ATTN: John C. Meester
ATTN: J. Heimerl
ATTN: Tech. Lib., Edward Baicy

Commander
US Army Electronics Command
ATTN: DRSEL-RD-P
ATTN: DRSEL-TL-1R, Edwin T. Hunter
ATTN: DRSEL-XL-D
ATTN: DNA Coordinator
ATTN: Inst. for Exploratory Res.
ATTN: Wpns. Effects Section
ATTN: Stanley Kronenberg

Commander
US Army Foreign Science & Tech. Center
ATTN: R. Jones

Commander
US Army Materiel Dev. & Readiness Command
ATTN: DRUDE-D, Lawrence Flynn

Commander
US Army Missile Command
ATTN: DRSMI-XS, Chief Scientist
ATTN: Chief Doc. Section

Commander
US Army Nuclear Agency
ATTN: MONA-WE, J. Berberet

Commander
US Army Satcom Agency
ATTN: Technical Library

Chief
US Army Research Office
ATTN: CRDARD-DCS, Hermann K. Robl
ATTN: CRDARD-P, Robert Mace

Commander
Whippany Field Office (BMDJOC-WS-W)
Bell Telephone Laboratories
ATTN: John Turner

Commander
White Sands Missile Range
ATTN: Willis W. Webb, AMSEL-NL-SD
ATTN: Marvin P. Squires, STEWS-TE-NT

DEPARTMENT OF THE NAVY

Chief of Naval Operations
Navy Department
ATTN: OP 981
ATTN: Code 604C3, Robert Piacesi

Commander
Naval Air Systems Command
Headquarters
ATTN: AIR 5381

DEPARTMENT OF THE NAVY (Continued)

Chief of Naval Research
Navy Department
ATTN: Code 427, CDR Ronald J. Oberle
ATTN: Code 461, R. Gracen Joiner
ATTN: Code JTU, John G. Dardis
ATTN: Code 464, Thomas P. Quinn
ATTN: Code 464, Jacob L. Warner

Commander
Naval Electronic Systems Command
Naval Electronic Systems Command Hqs.
ATTN: PME 117-T
ATTN: ELEX 03

Commanding Officer
Naval Intelligence Support Center
ATTN: Code 40A, E. Blase
ATTN: Document Control

Commander
Naval Ocean Systems Center
ATTN: William F. Moler
ATTN: Code 2200, Verne E. Hildebrand
ATTN: Code 2200, Richard Pappert
ATTN: Code 2200, Ilan Rothmuller
ATTN: Code 2200, Jurgen Richter
ATTN: Tech. Lib. for T. J. Keary

Superintendent (Code 1424)
Naval Postgraduate School
ATTN: Code 61, MN, E. A. Milne
ATTN: Code 61, DY, J. N. Dyer
ATTN: Code 2124, Tech. Rpts. Librarian

Director
Naval Research Laboratory
ATTN: Code 7128, James D. Kurfess
ATTN: Code 7730, Edgar A. McClean
ATTN: Code 7756, J. Davis
ATTN: Gerald H. Share
ATTN: Code 7125.7, Donald J. Moran
ATTN: W. Neil Johnson
ATTN: Code 2600, Tech. Lib.
ATTN: Code 7750, S. L. Ossakow
ATTN: Code 7701, Jack D. Brown
ATTN: Code 7750, Klaus Hain
ATTN: Code 7750, Wahab Ali
ATTN: Code 6603P, Richard L. Statler
ATTN: Code 6461, Francis J. Campbell
ATTN: Code 7127, Charles Y. Johnson
ATTN: Code 7700, Timothy P. Coffey
ATTN: Code 5174, Frederick W. Raymond
ATTN: Code 4004, Emanuel L. Brancato
ATTN: Robert L. Kinzer

Officer in Charge
Naval Surface Weapons Center
ATTN: Code WA501, Navy Nuc. Prgms. Off.

Commander
Naval Weapons Center
ATTN: Document Control

Commander
Naval Weather Service Command
Naval Weather Service Headquarters
Washington Navy Yard
ATTN: Mr. Martin

4 January 1977

DEPARTMENT OF THE NAVY (Continued)

Commanding Officer
Navy Astronautics Group
6 cy ATTN: W. J. Gleason

Commanding Officer
Nuclear Weapons Tng. Center Pacific
Naval Air Station, North Island
ATTN: Nuclear Warfare Department

Commander
Nuclear Weapons Tng. Group Atlantic
ATTN: Nuclear Warfare Department

DEPARTMENT OF THE AIR FORCE

Commander
ADC/DO
ATTN: DOF

Commander
ADCOM/XPD
ATTN: Hqs. 14th Aerospace Force (EVN)
ATTN: Paul Mason
ATTN: XPQDQ
ATTN: XPQDQ, Major G. Kuch

AF Geophysics Laboratory, AFSC
ATTN: OPR, Maj J. Reed
ATTN: OPR, J. Kennally
ATTN: SUOLA, E. L. Cunha
ATTN: OPR Alva T. Stair
ATTN: OPR, R. O'Neill
ATTN: OPR, T. Connolly
ATTN: OPR, Harold Gardner
ATTN: OPR, P. Billingsly
ATTN: H. A. B. Gardiner
ATTN: Lt Col W. Bittinger
ATTN: C. Stergis
ATTN: CRT
ATTN: L. Katz
ATTN: OPR, J. Rodgers
ATTN: LKB, A. Faire
ATTN: PHE, Joseph Kelly
ATTN: LKD, Edmond Murad
ATTN: LI, Phillip Newman
2 cy ATTN: PHG, J. C. McClay
ATTN: LIE, George J. Glassman
ATTN: Space Physics Lab., R. C. Filz
5 cy ATTN: LKB, Kenneth S. W. Champion
ATTN: LKB, T. J. Keneshea
ATTN: OPR, F. DelGrice
ATTN: LKS, F. R. Innes
ATTN: LKB, William S. Linder, Jr.
ATTN: LKD, Dr. Heroux
ATTN: LKD, Rocco S. Marcisi
ATTN: LKO, Robert E. Huffman
ATTN: OP, John S. Caring

AFTAC
5 cy ATTN: TD
ATTN: TF/Major Wiley
ATTN: TN-F, Lt Col E. C. Thomas
3 cy ATTN: TN
ATTN: Tech. Lib.

DEPARTMENT OF THE AIR FORCE (Continued)

AF Weapons Laboratory, AFSC
ATTN: DYT, Capt David W. Goetz
ATTN: DYT, Capt Hollars
ATTN: DYT, Joseph Janni
ATTN: CA, Arthur H. Guenther
ATTN: DYT, Capt Gary D. Cable
ATTN: DYT
ATTN: SUL

Headquarters
Air Force Systems Command
ATTN: SCTSW, Wpns. & Wpns. Effects Div.
ATTN: DLS
ATTN: Lt Col W. Beam
ATTN: Lt Col H. Simmons
ATTN: DLXP, Capt Roisal
ATTN: Lt Col E. C. Nealy
ATTN: SDS/DLSE
ATTN: Technical Library

Det. 1, 12WS
Space Forecasting Section
ATTN: Capt R. M. Healin

DE18, 30TWS
ATTN: Capt Edmund D. Dafzewski, USAF

Headquarters
Electronic Systems Division, (AFSC)
ATTN: James Whelan
ATTN: W. C. Morton

Commander
Foreign Technology Division, AFSC
ATTN: NICD, Library
ATTN: TDPSS, Kenneth N. Williams

Hq. USAF/IN
ATTN: IN

Hq. USAF/RD
ATTN: RD DCS, D. Rand
ATTN: RDPS
ATTN: RDQSM
ATTN: RDSA
ATTN: RD

Commander
Rome Air Development Center, AFSC
ATTN: V. Coyne
ATTN: EMTLD, Doc. Library
ATTN: Col R. Pactauf
ATTN: OCSF, J. J. Simons

SAMSO/DY
ATTN: DYE, Lt Col W. E. Herdrich
ATTN: DYE

SAMSO/SZ
ATTN: SZJ, Major Lawrence Doan

SAMSO/XR
ATTN: XR

Commander in Chief
Strategic Air Command
ATTN: XPPS, Maj Brian G. Stephan

4 January 1977

DEPARTMENT OF THE AIR FORCE (Continued)

USAFETAC/CB

ATTN: CBT, Mr. Creasi

4th Weather Wing, MAC
2 cy ATTN: AEGB

ENERGY RESEARCH & DEVELOPMENT ADMINISTRATION

Argonne National Laboratory
Records Control

ATTN: Doc. Con. for Len Leibowitz
ATTN: Doc. Con. for A. C. Wahl
ATTN: Doc. Con. for David W. Green
ATTN: Doc. Con. for Gerald T. Ready
ATTN: Doc. Con. for S. Gabelnick

Division of Military Application
US Energy Resch. & Dev. Admin.

ATTN: Doc. Con. for Donald I. Gale
ATTN: Doc. Con. for Maj D. A. Haycock
ATTN: Doc. Con. for Col T. Cross
ATTN: Doc. Con. for Frank A. Ross
ATTN: Doc. Con. for David H. Slade
ATTN: Doc. Con. for Rudolf J. Engelmann

University of California
Lawrence Livermore Laboratory

ATTN: Tech. Info. Dept. L-3
ATTN: J. F. Tinney, L-517

Los Alamos Scientific Laboratory

ATTN: Doc. Con. for William Maier
ATTN: Doc. Con. for David W. Steinhaus
ATTN: Doc. Con. for C. R. Mehl, Org. 5230
ATTN: Doc. Con. for Donald Kerr
ATTN: Doc. Con. for R. A. Jeffries
ATTN: Doc. Con. for John S. Malik
ATTN: Doc. Con. for J. Judd
ATTN: Doc. Con. for E. A. Bryant
ATTN: Reference Library, Ann Beyer
ATTN: D. M. Rohrer, MS 518
ATTN: Doc. Con. for John Zinn
ATTN: Doc. Con. for E. W. Hones, Jr.
ATTN: Doc. Con. for T. Bieniewski, CMB-1
2 cy ATTN: Doc. Con. for Martin Tierney, J-10
ATTN: Doc. Con. for S. Rockwood
ATTN: Doc. Con. for W. M. Hughes, MS 559
ATTN: Doc. Con. for Herman Hoerlin
ATTN: Doc. Con. for W. D. Marfield
ATTN: Doc. Con. for Marge Johnson

Sandia Laboratories

Livermore Laboratory
ATTN: Doc. Con. for Thomas B. Cook, Org. 8000

Sandia Laboratories

ATTN: Doc. Con. for Org. 9220
ATTN: Doc. Con. for W. D. Brown, Org. 1353
ATTN: Doc. Con. for Clarence R. Mehl, Org. 5230
ATTN: Doc. Con. for 3141, Sandia Rpt. Coll.
ATTN: Doc. Con. for Morgan L. Kramm, Org. 5720
ATTN: Doc. Con. for Craig Hudson
ATTN: Doc. Con. for J. C. Eckhardt, Org. 1250

ENERGY RESEARCH & DEVELOPMENT ADMINISTRATION
(Continued)

US Energy Research & Dev. Admin.
Division of Headquarters Services
Library Branch G-043

ATTN: Doc. Con. for George L. Rogosa
ATTN: Doc. Con. for H. H. Kurzweg
ATTN: Doc. Con. for D. Kohlstad
ATTN: Doc. Con. for Richard J. Kandel
ATTN: Doc. Con. for Joseph D. LaFleur

OTHER GOVERNMENT AGENCIES

Central Intelligence Agency

ATTN: RD/SI, Rm. 5G48, Hq. Bldg. for
NEB/OSI - 2G48 Hqs.

Department of Commerce

National Bureau of Standards

ATTN: Sec. Officer for Lewis H. Geyntman
ATTN: Sec. Officer for George A. Sinnatt
ATTN: Sec. Officer for D. Garvin
ATTN: Sec. Officer for K. Kessler
ATTN: Sec. Officer for J. McKinley
ATTN: Sec. Officer for J. Cooper
ATTN: Sec. Officer for B. Stienner
ATTN: Sec. Officer for M. Schear
ATTN: Sec. Officer for Stanley Abramowitz
ATTN: Sec. Officer for Office of Director
ATTN: Sec. Officer for D. R. Lide
ATTN: Sec. Officer for M. Krauss
ATTN: Sec. Officer for J. T. Herron

Department of Commerce

Office of Telecommunications
Institute for Telecom Science
ATTN: William F. Utiat

Department of the Interior

US Geological Survey
Special Projects Center
ATTN: Joseph C. Cain

Department of the Interior

US Geological Survey
ATTN: Robert W. Regan

Department of Transportation

Transportation Resch. System Center
ATTN: F. Marmo

Department of Transportation

Office of the Secretary
ATTN: R. Underwood
ATTN: Samuel C. Coroniti
ATTN: Richard L. Strombotne, TST-8
ATTN: Alan J. Grobecker
ATTN: Document Control

NASA

George C. Marshall Space Flight Center

ATTN: R. Chappell
ATTN: W. T. Roberts
ATTN: W. A. Oran
ATTN: C. R. Balcher
ATTN: N. H. Stone
ATTN: R. D. Hudson
ATTN: John Watts, Code ES22

4 January 1977

OTHER GOVERNMENT AGENCIES (Continued)

NASA

Coddard Space Flight Center
ATTN: James I. Vette
ATTN: J. Siry
ATTN: H. A. Taylor
ATTN: R. P. Benson
ATTN: M. Sugiura
ATTN: S. J. Bauer
ATTN: Technical Library
ATTN: A. C. Aiken
ATTN: J. P. Hepner
ATTN: G. Leviq
ATTN: Gilbert D. Mead, Code 641
ATTN: A. Tempkin

NASA

ATTN: J. Naugle
ATTN: E. R. Scherling
ATTN: A. Schardt
ATTN: H. H. Kurzweg
ATTN: R. A. Schiffer
ATTN: W. L. Taylor, Code ST
ATTN: J. Findlay
ATTN: D. R. William, Code ST
ATTN: P. Eaton
ATTN: N. Roman
ATTN: K. Fellows
ATTN: G. Sharp
ATTN: M. Tepper
ATTN: D. P. Cauffman

NASA

Johnson Space Center
ATTN: Owen Garriot
ATTN: Classified Lib., Code BM6

NASA

Ames Research Center
ATTN: N-245-3, Palmer Dyal
ATTN: C. P. Sonett
ATTN: M-254-4, R. Whitten
ATTN: N-245-4, Iliia G. Poppoff

NASA Scientific & Technical Info. Fac.
ATTN: Acq. Branch
ATTN: SAR/DLA-385

National Bureau of Standards

ATTN: W. Carl Lineberger, JILA
ATTN: Stephen J. Smith, JILA
ATTN: G. Reid
ATTN: A. V. Phelps, JILA
ATTN: Gordon H. Dunn, JILA
ATTN: Peter L. Bander, JILA

National Oceanic & Atmospheric Admin.
National Weather Service
Department of Commerce
ATTN: J. K. Angell
ATTN: L. Machta

National Oceanic & Atmospheric Admin.
National Ocean Survey
Department of Commerce

Washington Science Center
ATTN: Gerald A. Peterson
ATTN: Ronald L. Lavoie
ATTN: Wayne McGovern
ATTN: John W. Townsend, Jr.
ATTN: Edward S. Epstein

OTHER GOVERNMENT AGENCIES (Continued)

National Oceanic & Atmospheric Admin.
Environmental Research Laboratories
Department of Commerce
ATTN: Walther N. Spjeldvik
ATTN: k43, Herbert H. Sauer
ATTN: Robert B. Doeker
ATTN: R43, Donald J. Williams
ATTN: Aeronomy Lab., George C. Reid
ATTN: Eldon Ferguson
ATTN: RX1, Robert W. Knecht

National Science Foundation

ATTN: W. H. Cramer
ATTN: F. P. Todd
ATTN: Role Sinclair
ATTN: r. Gilman Blake
ATTN: R. Manka
ATTN: W. D. Adams
ATTN: R. S. Zapolsky
ATTN: Fred D. White
ATTN: M. K. Wilson

US Arms Control & Disarmament Agcy.

ATTN: Office of Director
ATTN: Reference Info. Center
ATTN: Pierce S. Corden

DEPARTMENT OF DEFENSE CONTRACTORS

Aerodyne Research, Inc.
ATTN: M. Camac

Aeronomy Corporation
ATTN: S. A. Bowhill

Aerospace Corporation
ATTN: V. Josephson
ATTN: Mr. Goldsmith
ATTN: G. Millburn
ATTN: L. W. Aukerman
ATTN: R. D. Rawcliffe
ATTN: J. Sorrels
ATTN: Julian Reinheimer
ATTN: D. C. Pecka
ATTN: V. Wall
ATTN: Thomas D. Taylor
ATTN: J. B. Blake
ATTN: Harris Mayer
ATTN: S. P. Bower
ATTN: J. Stevens
ATTN: N. Cohen
ATTN: M. Berg
ATTN: R. Mortensen
ATTN: George Paulikas
ATTN: T. Friedman
ATTN: Library
ATTN: F. Keller
ATTN: J. Woodford

Albright Colloge
ATTN: Moo. Ung. Kim, Physics Dept.

American Nucleonics Corporation
ATTN: Sec. Officer for G. L. Brown

American Science & Engineering, Inc.
ATTN: Document Control

Analytical Systems Engineering Corp.
ATTN: J. A. Caruso

4 January 1977

DEPARTMENT OF DEFENSE CONTRACTORS (Continued)

Battelle Memorial Institute
ATTN: Radiation Eff. Info. Center

The Boeing Company
ATTN: Glen Keister

The Trustees of Boston College
Chestnut Hill Campus
ATTN: R. Eather
ATTN: Library
ATTN: R. L. Carovillao
2 cy ATTN: Chairman Dept. of Chem.
ATTN: Prof. Marcov
ATTN: R. Hegblom

Brown Engineering Company, Inc.
ATTN: James E. Cato
ATTN: J. Dobkins

University of California at Los Angeles
Office of Contract & Grant Admin.
ATTN: T. A. Farley, Space Sci. Ltr.

University of California at Riverside
ATTN: Alan C. Lloyd
ATTN: James N. Pitts, Jr.

University of California at San Diego
Marine Physical Lab. of the Scripps
Institute of Oceanography
ATTN: C. E. McIlwain, Physics Dept.

University of California
Berkeley Campus Room 318
Sproul Hall
ATTN: Kinsey A. Anderson
ATTN: Michael Lampton

State of California
Air Resources Board
ATTN: Leo Zafonte

University of California
Space Sciences Laboratory
ATTN: Bodo Parady
ATTN: C. I. Meng

Calspan Corporation
ATTN: W. Wurster
ATTN: Robert A. Fluegge
ATTN: C. E. Treanor
ATTN: M. G. Dunn

University of Colorado
Office of Contracts & Grants
ATTN: Jeffrey B. Pearce, LASP
ATTN: C. Beaty, JILA
ATTN: Charles A. Barth, LASP
ATTN: A. Phelps, JILA
ATTN: C. Lineberger, JILA

The Trustees of Columbia University
ATTN: Sec. Officer, H. M. Foley
ATTN: Richard N. Zare

Comsat Laboratories
ATTN: Document Control

DEPARTMENT OF DEFENSE CONTRACTORS (Continued)

Epsilon Laboratories, Inc.
ATTN: Henry Miranda
ATTN: Carl Accardo

ESL, Inc.
ATTN: James Marshall

Extranuclear Laboratories, Inc.
ATTN: Wade Fite

General Dynamics Corp.
Convair Division
ATTN: Library, 128-00

General Electric Company
Space Division
Valley Forge Space Center
ATTN: Tech. Info. Center
ATTN: T. Baurer
ATTN: F. Alyea
ATTN: Joseph C. Peden, VFSC, Rm. 4230M
ATTN: P. Zavitsanos
ATTN: M. H. Bortner, Space Sci. Lab.

General Electric Company
Re-Entry & Environmental Systems Div.
ATTN: A. A. Siniagalli

General Electric Company
TEMPO-Center for Advanced Studies
ATTN: Warren S. Knapp
ATTN: Tim Stephens
77 cy ATTN: DASIAC
ATTN: Mike Dudash
ATTN: B. Gambill
ATTN: Don Chandler

General Electric Tech. Services Company, Inc.
HMES
ATTN: George Millman

General Research Corporation
ATTN: John Isa, Jr.

General Research Corporation
Washington Operations
ATTN: Thomas M. Zakrzewski

Geophysical Institute
University of Alaska
ATTN: Henry Cole
ATTN: R. Parthasarathy
ATTN: S. I. Akasofu
ATTN: T. N. Davis
ATTN: A. Belon
2 cy ATTN: Neal Brown
ATTN: Technical Library
ATTN: J. S. Wagner, Physics Dept.
ATTN: D. J. Henderson

Grumman Aerospace Corporation
ATTN: Marton Bossi

Harvard College Observatory
Smithsonian Astrophysical Observatory
Center for Astrophysics
ATTN: J. Patrick Henry

4 January 1977

DEPARTMENT OF DEFENSE CONTRACTORS (Continued)

HRB-Singer, Inc.
ATTN: Tech. Info. Center

hSS, Inc.
ATTN: Document Control
ATTN: H. Stewart
ATTN: Donald Hansen
ATTN: M. P. Shuler

IBM Corporation
ATTN: Technical Rpts. Center (912 A816)

IIT Research Institute
ATTN: Technical Library
ATTN: R. B. Cohen

University of Illinois
Physics Department
ATTN: William J. Otting

Institute for Defense Analyses
ATTN: IDA Librarian, Ruth S. Smith
ATTN: Hans Wolfhard
ATTN: Joel Bangston
ATTN: Ernest Bauer

Intl. Business Machines Corp.
Data Processing Division
ATTN: D. C. Sullivan

IRT Corporation
ATTN: R. L. Mertz
ATTN: Evan Miller
ATTN: R. H. Neynaber
ATTN: F. W. Simpson
ATTN: R. F. Overmyer, GRT

Johns Hopkins University
Applied Physics Laboratory
ATTN: Peter E. Partridge
ATTN: S. M. Krimigis
ATTN: Document Librarian

Kaman Sciences Corporation
ATTN: Frank H. Shelton
ATTN: W. Foster Rich
ATTN: Library

Lockheed Missiles & Space Company, Inc.
ATTN: J. H. Hockenberry, D/60-01
ATTN: Philip J. Hart, Dept. 81-14
ATTN: W. P. Minnaugh, D/69-50
ATTN: F. M. Friedlaender
ATTN: J. Cretcher
ATTN: Q. A. Riepe, D/60-80
ATTN: D. R. Churchill
ATTN: S. I. Weiss, D/68-01
ATTN: D. L. Crowther, D/62-25
ATTN: Edwin A. Smith, Dept. 85-85
ATTN: J. T. Hart, Jr., D/61-03
ATTN: E. E. Crowther, D/60-01
ATTN: D. F. McClinton
ATTN: Samuel I. Taimuty, Dept. 85-85

M.I.T. Lincoln Laboratory
ATTN: James H. Pannell, L-246
ATTN: W. E. Morrow

DEPARTMENT OF DEFENSE CONTRACTORS (Continued)

Lockheed Missiles & Space Company, Inc.
ATTN: W. D. Frye, D/52-21
ATTN: W. E. Francis, D/52-12
ATTN: W. L. Imhof, D/52-12
ATTN: T. D. Damsell
ATTN: R. D. Meyerott
ATTN: Tech. Info. Center, D/COLL
ATTN: R. K. Landshoff
ATTN: J. B. Reagan, D/52-12
ATTN: A. D. Anderson, D/52-12
ATTN: John B. Cladis, Dept. 52-12
ATTN: James W. Schallau
ATTN: John E. Evans, Dept. 52-14
ATTN: G. H. Nakano, D/52-12, B/205
ATTN: John Kumer
ATTN: L. L. Newkirk, D/52-21
ATTN: Tom James
ATTN: G. T. Davidson, D/52-12
ATTN: Martin Walt, Dept. 52-10
ATTN: R. A. Breuch, D/52-21
ATTN: R. D. Sharp, D/52-12
ATTN: R. P. Caren, D/52-20
ATTN: D. C. Fisher, D/52-14
ATTN: Richard G. Johnson, Dept. 52-12
ATTN: Billy M. McCormac, Dept. 52-54

Maxwell Laboratories, Inc.
ATTN: Victor Fargo

McDonnell Douglas Corporation
ATTN: A. J. Mauley
ATTN: A. D. Goedeke
ATTN: William Olsen

University of Minnesota
ATTN: J. R. Winkler

Mission Research Corporation
ATTN: Conrad L. Longaire
ATTN: D. Archer
ATTN: M. Scheibe
ATTN: P. Fischer
ATTN: R. Hendrick
ATTN: Dave Sowie
ATTN: D. Sappenfield
ATTN: R. Bogusch

Mission Research Corporation-San Diego
ATTN: V. A. J. Van Lint

The Mitre Corporation
ATTN: Tech. Lib. for R. Greeley
ATTN: P. Grant
ATTN: Tech. Lib. for B. Troutman
ATTN: Library

National Academy of Sciences
ATTN: National Materials Advisory Board for Edward R. Dyer
ATTN: National Materials Advisory Board for William C. Bartley
ATTN: National Materials Advisory Board for J. R. Sievers

Photometrics, Inc.
ATTN: Irving L. Kofsky

4 January 1977

DEPARTMENT OF DEFENSE CONTRACTORS (Continued)

Pennsylvania State University
Industrial Security Office
ATTN: L. Hale
ATTN: J. S. Nisbet

Physical Dynamics, Inc.
ATTN: A. Thompson
ATTN: Joseph B. Workman

Physical Sciences, Inc.
ATTN: R. L. Taylor
ATTN: Kurt Wray

University of Pittsburgh of the Comwth. Sys. of
Higher Education
Cathedral of Learning
ATTN: Manfred A. Biondi
ATTN: Wade L. Fite
ATTN: Frederick Kaufman

R & D Associates
ATTN: R. P. Turco
ATTN: Robert E. LeLevier
ATTN: William J. Karzas
ATTN: S. Clay Rogers
ATTN: R. G. Lindgren
ATTN: Forrest Gilmore
ATTN: William R. Graham, Jr.
ATTN: H. A. Dry

R & D Associates
ATTN: Herbert J. Mitchell

Radiation Research Associates, Inc.
ATTN: N. M. Schaeffer

The Rand Corporation
2 cy ATTN: Technical Library
ATTN: Paul Tamarkin
ATTN: Cullen Grain

Rice University
Department of Space Science
ATTN: Joseph Chamberlain
ATTN: Ronald F. Stebbings

William Marsh Rice University
ATTN: Industrial Sec. Super., J. Chamberlain

Rockwell International Corporation
Space Division
ATTN: William Atwell

Sanders Associates, Inc.
ATTN: Jack Schwartz

Science Applications, Inc.
ATTN: Daniel A. Hamlin
ATTN: D. Sachs

Science Applications, Inc.
Huntsville Division
ATTN: Noel R. Byrn

Professor Chalmers F. Sechrist
ATTN: C. Sechrist

DEPARTMENT OF DEFENSE CONTRACTORS (Continued)

Smithsonian Astrophysical Observatory
ATTN: A. Dalgarno

University of Southern California
ATTN: S. W. Benson

Space Data Corporation
ATTN: Edward F. Allen

Sperry Flight Systems Division
Sperry Rand Corporation
ATTN: D. Andrew Schow

Stanford Research Institute
ATTN: James R. Peterson
ATTN: Felix T. Smith
ATTN: Ronald White
ATTN: Ray L. Leadabrand
ATTN: G. Black
ATTN: R. D. Hake, Jr.
ATTN: Arthur Lee Whitson
ATTN: M. Baron
ATTN: L. L. Cobb
ATTN: J. Lomax
ATTN: E. Kindermann
ATTN: Burt R. Gasten
ATTN: Allen M. Peterson
ATTN: Walter G. Chestnut

Stanford Research Institute
ATTN: Warren W. Barning

Stanford University
Radio Science Laboratory
ATTN: D. L. Carpenter
ATTN: R. S. Helliswell

Technology International Corporation
ATTN: W. P. Boquist

TRW Defense & Space Sys. Group
ATTN: R. K. Piebuch, R1-2078
ATTN: Tech. Info. Center/S-1930
ATTN: Robert M. Webb, R1-2410
ATTN: R. Watson, R1/1096
ATTN: J. F. Fricthenicht, R1-1196
ATTN: H. H. Holloway, R1-2036
ATTN: F. Scarf, R5-1280
ATTN: O. E. Adams, R1-1144

United Technologies Corporation
ATTN: H. Michaels
ATTN: Robert H. Bullis
ATTN: J. B. Addison

Utah State University
ATTN: Kay Baker
ATTN: D. Burt
ATTN: Doran Baker
ATTN: C. Wyatt

VisiDyne, Inc.
ATTN: Oscar Manley
ATTN: J. W. Carpenter

Wayne State University
ATTN: Pieter K. Rol, Chem. Engrg. & Mat.
Sci.
ATTN: R. H. Kummier

4 January 1977

DEPARTMENT OF DEFENSE CONTRACTORS (Continued)

Wayne State University
Dept. of Physics
ATTN: Walter E. Kauppila

DEPARTMENT OF DEFENSE CONTRACTORS (Continued)

Yale University
ATTN: Engrg. Dept.